RF PULSE DESIGN FOR PARALLEL TRANSMISSION IN ULTRA HIGH FIELD MAGNETIC RESONANCE IMAGING

by

Hai Zheng

B.S., Xi'an JiaoTong University, 2005

Submitted to the Graduate Faculty of
the Swanson School of Engineering in partial fulfillment
of the requirements for the degree of
Doctor of Philosophy

University of Pittsburgh
2012

UNIVERSITY OF PITTSBURGH

SWANSON SCHOOL OF ENGINEERING

This dissertation was presented

by

Hai Zheng

It was defended on

January 23, 2012

and approved by

George D. Stetten, M.D., Ph.D., Professor, Department of Bioengineering and Radiology

Tamer S. Ibrahim, Ph.D., Associate Professor, Department of Bioengineering and Radiology

Douglas C. Noll, Ph.D., Professor, Department of Biomedical Engineering and Radiology, University of Michigan

Dissertation Director: Fernando E. Boada, Ph.D., Professor, Department of Radiology and Bioengineering

RF PULSE DESIGN FOR PARALLEL TRANSMISSION IN ULTRA HIGH FIELD MAGNETIC RESONANCE IMAGING

Hai Zheng, Ph.D.

University of Pittsburgh, 2012

Magnetic Resonance Imaging (MRI) plays an important role in visualizing the structure and function of the human body. In recent years, ultra high magnetic field (UHF) MRI has emerged as an attractive means to achieve significant improvements in both signal-to-noise ratio (SNR) and contrast. However, *in vivo* imaging at UHF is hampered by the presence of severe B_1 and B_0 inhomogeneities. B_1 inhomogeneity leads to spatial non-uniformity excitation in MR images. B_0 inhomogeneity, on the other hand, produces blurring, distortions and signal loss at tissue/air interfaces. Both of them greatly limit the applications of UHF MRI. Thus mitigating B_1 and B_0 inhomogeneities is central in making UHF MRI practical for clinical use.

Tailored RF pulse design has been demonstrated as a feasible means to mitigate the effects of B_1 and B_0 inhomogeneities. However, the primary limitation of such tailored pulses is that the pulse duration is too long for practical clinical applications. With the introduction of parallel transmission technology, one can shorten the pulse duration without sacrificing excitation performance. Prior reports in parallel transmission were formulated using linear, small-tip-angle approximation algorithms, which are violated in the regime of nonlinear large-tip-angle excitation.

The overall goal of this dissertation is to develop effective and fast algorithms for parallel transmission UHF RF pulses design. The key contributions of this work include 1) a novel large-tip-angle RF pulse design method to achieve significant improvements compared with previous

algorithms; 2) implementing a model-based eddy current correction method to compensate eddy current field induced on RF shield for parallel transmission and leading to improved excitation and time efficiency; 3) developing new RF pulse design strategy to restore the lost signal over the whole brain and increase BOLD contrast to brain activation in T_2*-weighted fMRI at UHF.

For testing and validation, these algorithms were implement on a Siemens 7T MRI scanner equipped with a parallel transmission system and their capabilities for ultra high field MRI demonstrated, first by phantom experiments and later by *in vivo* human imaging studies. The contributions presented here will be of importance to bring parallel transmission technology to clinical applications in UHF MRI.

TABLE OF CONTENTS

LIST OF FIGURES

ACKNOWLEDGEMENT

The dissertation would not have been possible without the help and support of many individuals. First, most importantly, I would like to express my greatest appreciation to my advisor, Dr. Fernando E. Boada, who has been instrumental to this work. I am especially grateful to him for the guidance, inspiration and support through my PhD studies at the University of Pittsburgh Magnetic Resonance Research Center (MRRC). Being a great mentor, he is creative, broad-minded and visionary. I was blessed to have him as an advisor and excited to be working with him.

I would also like to thank the committee members: Dr. Douglas C. Noll, Dr. Tamer S. Ibrahim, and Dr. George D. Stetten for their valuable time and insightful comments on my dissertation.

I am fortunate to have the opportunity to work with Tiejun Zhao. I would like to convey my sincere gratitude to him for tremendous help on completing my PhD. He is leading me into MR field and helping me out whenever I had a problem with MR physics, pulse sequence, the scanner, computer programming, or anything else. I have learned a lot from him since I first joined MRRC.

I am also grateful to Yongxian Qian for teaching me MR physics, pulse sequence and write papers. It has been a true pleasure working with you, a knowledgeable MR scientist.

I would also like to thank the rest of my colleagues Howard Aizenstein, Lei Sheu, Kathryn Edelman, Claudiu Schirda, Stephen Hegedus, Stephen Yutzy, Chris Cieply, Vincent

I would also like to thank the rest of my colleagues Howard Aizenstein, Lei Sheu, Kathryn Edelman, Claudiu Schirda, Stephen Hegedus, Stephen Yutzy, Chris Cieply, Vincent Lee, Anthony Defranco, Yujuan Zhao, Daniel Stough, Narayanan Krishnamurthy for their help and friendship. You guys have been great and helpful.

Xun Jiang, my wife, has done so much to support me over years since I first came to US. She is the one that motivates me to keep moving forward and brings me limitless happiness. We have been through a lot together, happy and stressful time. No matter what the future is, we will get there together. It is a wonderful life.

Finally, I would like to thank my parents and parents-in-law. They always support, trust and understand me. I am always the best in their view. They are standing behind me and encouraging me to advance forward.

Dedicated to my wife and family.

Hai Zheng

Santa Clara, California

March 11, 2012

1.0 INTRODUCTION

1.1 THE AIMS OF THIS DISSERTATION

1.1.1 Ultra High Field MRI

Magnetic Resonance Imaging (MRI) plays an important role in visualizing the structure and function of human body. Its extraordinary soft tissue contrast makes it the preferred imaging modality for diagnosing many soft tissue disorders, especially in the brain, spinal cord, and pelvis. In recent years, **ultra high magnetic field MRI** is of most interests to achieve significant improvements in both image signal-to-noise ratio (SNR) (1) and contrast. However, in vivo imaging at ultra high field is hampered by the presence of severe B_1^+ inhomogeneity (2) arising from wavelength interference effects (3, 4), and tissue conductive radio frequency (RF) amplitude attenuation (5). This leads to very unfavorable spatial non-uniformity excitation in the region of interest, and greatly limits the applications of ultra high field MRI.

1.1.2 Large-tip-angle RF Pulse Design

RF pulse design has been demonstrated as a feasible approach to mitigate B_0 and B_1 inhomogeneities, including spatially tailored RF pulses design (6-8), RF shimming (9-11), adiabatic pulses (12, 13). We will focus on spatially tailored excitation design due to its significant advantages. But the primary limitation of such pulses is in their long pulse duration, which makes them impractical for clinical use. With the inception of **parallel transmission** (14-16), whereby multiple independent RF excitation channels are simultaneously used instead of single channel used in conventional scanners, pulse duration can be dramatically shortened but at the cost of substantially more complicated RF pulses design. Prior works in parallel transmission are formulated on linear approximation design algorithms, which are violated in the regime of large-tip-angle excitation. The performance of many pulse sequences are primarily relied on the performance of large-tip-angle RF pulses, such as, MP-RAGE, RARE and DTI. Thus, **the first goal** of this dissertation is to design large-tip-angle RF pulses at ultra high field using parallel transmission technology to effectively mitigate B_0 and B_1 inhomogeneities with practical RF pulses.

1.1.3 Eddy Current Compensation

SAR is a serious issue accompanying with ultra high field MRI. The pulses calculated here often lead to high peak RF magnitudes that might not be well-suited practical routine on human subjects. Transverse electromagnetic (TEM) coil is employed in our experiments due to its efficiency and can be driven with relatively low voltage. However, stronger eddy currents arise. Thus effective **Eddy Current Compensation** algorithms for parallel transmission are in high demand, which is **the second goal** of this dissertation.

1.1.4 T_2^*-weighted BOLD fMRI

One of the straightforward applications of parallel transmission is functional Magnetic Resonance Imaging (fMRI) (17-19). In T_2^*-weighted blood-oxygenation-level-dependent (BOLD) (20) fMRI, images suffer from signal loss artifacts at the brain regions close to air-filled cavities. The artifacts arise from magnetic field inhomogeneity caused by the magnetic susceptibility difference between air and tissue in human head, and impede the study of some important brain regions such as the orbital frontal and inferior temporal cortices (21). This phenomenon is more apparent at ultra high field MRI. Various techniques have been proposed to recover magnetic susceptibility induced signal loss, such as thin slice (22), z-shim (23, 24), 3D tailored RF pulses (25, 26). The primary drawback of tailored RF pulses is long pulse duration; nevertheless, parallel transmission can dramatically reduce pulse duration. **The third goal** of this dissertation is to design tailored RF pulses that can recover signal loss induced by magnetic susceptibility in T_2^*-weighted functional MRI at ultra high field strength using parallel transmission technology.

1.1.5 Specific Aims

Aim #1: Design effective and fast algorithms for large-tip-angle RF pulses that can be successfully employed in *in vivo* B_1^+ inhomogeneity mitigation at ultra high field MRI using parallel transmission. To fulfill this aim, we design large-tip-angle RF pulses to improve the performance of large-tip-angle excitation (90^o excitation, 180^o inversion and 180^o refocusing) at ultra high field MRI. To demonstrate the strengths of the proposed algorithms, we compare proposed algorithms with other existing algorithms, such as small tip angle method and additive angle method.

Aim #2: Design effective and fast algorithms to counteract the eddy currents in parallel transmission. To fulfill this aim, we propose eddy current compensation method through characterizing the system constants of eddy currents. This algorithm is very straightforward and efficient to compensate the artifacts from two perspective, hardware and software.

Aim #3: Design effective and fast algorithms for RF pulses for practical applications. The one demonstrated in this dissertation is to recover the magnetic susceptibility induced signal loss in T_2*-weighted fMRI at ultra high field strength using parallel transmission. Precompensated algorithm would cancel out intravoxel dephasing and then spins would be in phase during the center of data acquisition. This has previously not been practical due to the requirement of lengthy RF pulses, but becomes feasible with the parallel transmission technology.

In summary, the goal of this dissertation is on algorithm design and implementation of the novel technology---parallel transmission, ultimately with applications in human imaging. The effective RF pulses design algorithms is essential to bring high and ultra high field human MRI to clinical use.

1.2 THE SIGNIFICIANCE OF THIS DISSERTATION

1.2.1 Parallel Transmission Technology

Recently, ultra high field MRI gains more and more interests due to dramatic improvements in SNR and contrast. However, ultra high field human MRI must overcome several technical challenges to be successful. In particular, inhomogeneous RF (B_1^+) field arises when the wavelengths of the transmitted RF pulses are comparable to the size of the imaged anatomy (3). B_1^+ inhomogeneity causes images to exhibit center brightening, spatial contrast variation, and SNR nonuniformity, despite the use of homogeneous volume RF excitation coils (5, 27, 28). These give rise to various image artifacts and impede the performance of many pulse sequences, which seriously limit practical applications of ultra high field MRI.

RF pulse design for multidimensional selective excitation (29) in the presence of time-varying gradients has many practical applications, such as B_1^+ inhomogeneity mitigation and localized volume excitation. Nevertheless, due to limitations in gradient hardware and RF power deposition, such RF pulse design can lead to long pulse duration that hampers their performance and practical applicability. With the introduction of parallel transmission design in conjunction with multiple channels that are capable of simultaneous, independent RF excitation, one can shorten pulse duration by taking the advantage of sensitivity pattern in spatial excitation among the array of coils (30). Parallel transmission has several advantages over conventional single channel transmission due to the extra degrees of freedom created by multiple independent channels.

First, parallel transmission enables undersampling in excitation k-space because of its ability to correct for the undersampling induced aliasing, which leads to shorten RF pulses while maintaining the excited magnetization profiles (30, 32).

Second, parallel transmission can improve the spatial excitation pattern while without increasing the RF pulse duration (33).

Third, parallel transmission can control different RF pulse shapes, rather than only amplitudes and phases as RF shimming (9-11), and provides complete control over different RF pulses. It is therefore able to produce more homogeneous RF excitation, which is crucial for ultra high field imaging in which B_1 field is rather inhomogeneous due to dielectric resonances and tissue conductivity-induced RF amplitude attenuation.

Fourth, specific absorption rate (SAR) can be incorporated in the design, which can compromise between the excitation profile and RF power deposition, including local and global RF power distributions.

1.2.2 RF Pulse Design for Parallel Transmission

To date, most of the proposed parallel RF excitation designs are based on the small-tip-angle approximation (29). This formulation greatly simplifies computation and can provide good trade-off for designs since the problem of RF pulse design is reduced to a linear system. But, these methods can only design excitation pulses within the regime of small tip angle, (e.g., 30^o), and cannot design inversion and refocusing pulses. Even for 90^o excitation, the pulses based on small-tip-angle approximation can yield significant error in the excitation profiles (31). So designing effective algorithms for large tip angle RF pulses for parallel transmission is prerequisite for the clinical use of parallel transmission.

Note that there are non-iterative and iterative methods available for designing multidimensional large-tip-angle RF pulses for parallel transmission.

The most widely used non-iterative method is named by linear-class large-tip-angle (**LCLTA**) RF pulse design for parallel transmission (34), which is based on the LCLTA theory (35) at single channel and then extends to parallel transmission. The LCLTA design generalizes the Small Tip Angle (STA) design by concatenating a sequence of small excitation pulses when a special class of excitation k-space trajectories is used, such as inherently self-refocused spiral. The formulation of LCLTA design is very similar to STA design except that the magnetization profile is replaced with flip angle profile. Strictly speaking, both STA and LCLTA are linear approximation of nonlinear Bloch equation. STA or LCLTA is only the first term in a perturbation expansion of the Bloch equation (36). As a result, imperfections due to the higher order terms missing can appear in the excited magnetization profiles, even the assumptions of STA or LCLTA are satisfied. Significant distortions can appear when the assumptions of STA or LCLTA are violated, e.g., when using the STA method to design 90^o excitation or when using the LCLTA method on echo planar (EP) trajectory.

Heretofore, many methods based on iterative scheme have been proposed. Xu et al. (37) formulated the multidimensional, multichannel RF pulse design as an **Optimal Control** problem with multiple controls based directly on the Bloch equation. A first-order gradient optimization algorithm is used to iteratively solve the control problem, where STA or LCLTA is used as an initial guess. RF pulse design is completely considered as a black box and thus computationally demanding. Most importantly, this method may converge to a local minimum solution of insufficient accuracy. Another iterative scheme is **Additive Angle (AA)** method proposed by Grissom *et al* (38). This method is based on a series of iterative updates to a large-tip-angle pulse. A small-tip-angle RF pulse is as the initial pulse and significant deviation from the desired pattern is expected. Then another small-tip-angle pulse is designed to add the previous one, to bring the pattern excited by summed pulses closer to the desired pattern. The summed pulse is seeded to the next iteration, and iterations continue until a convergence criterion is met. Because additive angle method is formulated as a small number of Bloch equation simulations and fast small-tip-angle pulse designs, the computational time is relatively shorter than optimal control method. However, additive angle method employs a series of iterative linear pulse designs to approximate the nonlinear Bloch equation, notable excitation error appear particularly at high acceleration with the use of echo planar (EP) trajectory. Therefore, it is necessary to derive RF waveforms directly from the Bloch equation and design effective and fast algorithm for large-tip-angle RF pulses for parallel transmission.

1.2.3 Significance of Aims

Aim #1 is to propose effective and fast algorithm for designing large-tip-angle RF pulses for parallel transmission to excite desired pattern in the presence of severe B_1^+ inhomogeneity at ultra high field. To achieve effectiveness, it is inevitable to derive RF pulses directly from the Bloch equation; to achieve rapidness, complicated evaluation should be avoided. In this work, we evaluate the use of a novel approach, which called **Perturbation Analysis Method (PTA)**, for parallel transmission RF pulse design that is based on a perturbation analysis of the Bloch equation. In this approach, the difference between the target magnetization profile and that produced by STA designed pulses can be analytically expressed as a function of the applied RF pulses. This analytical expression can then be used to calculate corrections for the applied RF pulse in an iterative fashion. It is similar to Additive angle method, but the equations are derived directly from the Bloch equation. Three different comparisons of 90^o excitation, 180^o inversion and 180^o refocusing are shown among three methods of STA, AA and PTA. Excitation error and peak amplitude are evaluated at various acceleration factors (R), which is defined as the number of interleaved trajectories.

Furthermore, it has been noted that hardware and experimental imperfections can severely alter the excitation patterns obtained with these accelerated pulses at ultra high field imaging (39, 40). The distortion induced by RF coils is also very evident especially in spatially localized excitations of parallel transmission. Although many techniques, such as shielded gradients (41), pre-emphasis system (42), and k-space trajectory measurement (40, 43) have been reported to compensate the eddy current field; however, they are either only compensate the gradient coil induced eddy currents or the measurement of actual k-space trajectory is too time-consuming and/or inaccurate to compensate RF induced eddy currents. The synchronization of multiple RF pulse channels and gradient waveforms should be also taken into consideration. So **Aim #2** is to propose a novel method of **Eddy Current Compensation** for parallel transmission RF pulse design to compensate the overall distortion using multi-exponential fitting of the eddy current model to determine the eddy current fields. Substantial improvements in multi-dimensional excitation pattern accuracy should be obtained with this correction method. The improvements should be particularly notable in the case of high acceleration factor, where strong eddy current is presented. Simulations as well as experiments should show that this proposed approach leads to fast convergence and improved excitation quality during parallel transmission.

Designing large-tip-angle RF pulses is very important for practical applications. Diffusion tensor imaging (DTI) can map the tissue fiber orientation and connectivity in three dimensions, guided by the principal diffusion directions (44). It is a very important technique to characterize the tissue properties and can be used as more early detection than conventional T_1 or T_2 imaging in which tissues has significantly different microstructural characteristics (45). Some clinical applications of DTI are in the tract-specific localization of white matter lesions such as trauma and in defining the severity of diffuse traumatic brain injury (TBI). The localization of tumors in relation to the white matter tracts (infiltration, deflection) has been one of the most important initial applications. At present, single-shot spin-echo EPI with diffusion gradient is the most prevalent sequence due to its high acquisition speed (e.g., <100 ms per image) and motion insensitivity. However, the performance of this sequence is under expectation at ultra high field MRI due to the severe B_1^+ inhomogeneity, which 180^o refocusing pulses cannot successfully refocus every position in phase. Furthermore, at ultra field MRI, adiabatic pulses are employed to excite sequences with inversion pulses, such as MP-RAGE or inversion recovery, since it can invert magnetization vectors uniformly even in the presence of a spatially nonuniform B_1 field. However, the power deposition is much higher than non-adiabatic pulses, which limits its widespread use. Parallel transmission can overcome the aforementioned limitations while maintaining lower power deposition. The only necessity is an effective and fast algorithm for designing large-tip-angle RF pulses for parallel transmission.

Based on the success of aforementioned aims, **Aim #3** is to design multi-dimensional multi-channel tailored RF pulses to **precompensate** intravoxel dephasing caused by magnetic susceptibility for signal recovery in **T_2*-weighted fMRI**. Along with high-resolution anatomical brain images, functional images allow localization of brain functions that evolve over the duration of an experimental paradigm (46). Such capability of functional localization has proven to be invaluable to researchers in neuroscience, psychology, psychiatry, and beyond. Among many contrast mechanisms for fMRI, T_2*-weighted blood-oxygenation-level-dependent (BOLD)

(19) image contrast has been the most popular up to now. Neuronal activities, such as action potential generation and neurotransmitter release, initiates complex interactions among local blood flow, volume and oxygenation level (19, 20 and 47). This process leads to a decrease in regional deoxyhemoglobin concentration, which has been attributed to an increase in cerebral blood flow that exceeds oxygen consumption, and then causes an increase in regional blood oxygenation level, which increase the T_2* value of blood. Therefore, T_2*-weighted image contrast can be used to infer neuronal activities, although mechanisms are not fully understood.

Magnetic susceptibility is defined as the degree to which a material magnetizes in the presence of an external magnetic field. The value of magnetic susceptibility can be positive or negative (paramagnetic or diamagnetic, respectively). Magnetic field is distorted because such variation of field strength from inside to outside of intravoxel, particularly at the interface of susceptibility differences. Deoxyhemoglobin (deoxy-Hb) is strongly paramagnetic, while oxyhemoglobin (oxy-Hb) is slightly diamagnetic. Therefore, in a uniform magnetic field, those cells containing more oxy-Hb create more homogeneous field than those containing more deoxy-Hb. According to the Larmor frequency, excited spins precesses at different frequencies in the presence of inhomogenous field, which leads to spatial dispersion of the phase of spins and contributes to T_2* contrast. Although Gradient echo planar imaging GE-EPI with long readout and TE provides good susceptibility-induced T_2* contrast and temporal resolution, however, it is vulnerable to susceptibility-induced artifacts. The primary artifact origin is magnetic susceptibility difference between brain structures and air cavities, which leads to main field inhomogeneity. Signal loss is the most critical artifact and difficult to be corrected in the image reconstruction process. The origin of signal loss is intravoxel dephasing, which caused by susceptibility-induced field inhomogeneity. Intravoxel dephasing leads to vector cancellation, which results in partial or even complete voxel signal intensity drop. In multi-dimensional excitation, pixel dimension of through plane is often larger than the one of in plane. So through-plane dephasing is usually the dominant factor of signal loss relative to in-plane dephasing. But in-plane dephasing should be taken into consideration at ultra high field due to the severe B_1 inhomogeneity in plane. The study of some important brain regions such as the orbital frontal and inferior temporal cortices are severely hampered by signal loss.

Several approaches have been proposed to recover the susceptibility-induced signal loss. It can be mitigated by the reduction of the size of image voxels, which is called “thin slices” (48, 49). If the voxel dimension of though plane is reduced, cancellation of dephased spin signals is alleviated. However, one major drawback of using thin slices is, obviously, a reduction in brain coverage per repetition time. So the scanning time will be increased by multiple folds compared to conventional thick slices are used. Some groups proposed to use an external coil for localized shimming to recover signal loss directly at counteracting the field distortion by placing coils close to the field inhomogeneity (50, 51). These localized shimming methods were effective to certain extents in improving field homogeneity. However, for long time fMRI sessions, placement of shimming hardware on subject leads to significant discomfort, which likely increases head motion and thus critical artifacts are observed. Another class of methods uses z-gradient lobs to compensate for through-plane dephasing, which is called “z-shim” (24, 52-55). A z-gradient lobe, deployed after excitation, can create linear phase along z dimension that could cancel out the dephasing due to field inhomogenetiy accumulated up to data acquisition. Since gradient lobes are non-selective and the extent of dephasing varies as a function of voxel location, one needs to acquire multiple subimages using different gradient moments to refocus different image regions. Then the subimages can be combined in various ways (23, 24), to form a final image free of signal loss. To generate an image with acceptable signal recovery, it usually requires several subscans for each slice location, and hence a major problem of z-shim is the temporal resolution loss due to acquisition of multiple subimages for each slice location.

Three dimensional tailored RF (3DTRF) pulse design was firstly introduced to signal loss recovery by Stenger *et al* (25). This method is based on the excitation k-space analysis perspective and under the small-tip-angle approximation to the Bloch equation (29). It has several important advantages.

First, it has no interference with imaging parameters, for example, thin slice thickness is not required.

Second, due to the incorporation of field map, it does not require multiple subimage acquisitions for a single image, which is a significant advantage compared to z-shim that temporal resolution is sacrificed.

Finally, this method can be applied in conjunction with many other existing methods, such as thin slice, localized shimming and z-shim for maximal signal recovery.

However, this pulse design is impractical in clinical uses unless several major technical hurdles are overcome. First, the 3DTRF pulses are exceedingly long relative to slice-selective SINC pulses. It was demonstrated that a 60-ms 3DTRF pulses was effective in selecting a 2-cm thick slice, and recovering signal loss above the sinus cavity (25). Needless to say the select slices of 5 mm in typical fMRI studies, the designed pulses will be much longer than 60ms. Also, it is difficult to simultaneously recover multiple regions, which typically appear at places close to air-filled middle ears and sinuses. In addition, it does not perform well at places where the magnetic field is severely inhomogeneous. Large frequency offset will destroy the in-plane excitation accuracy, though the effect in slice selective direction is minimal.

Although Yip *et al* (26) demonstrated that pulse duration of 3DTRF could be reduced to 15.4 ms in selecting 5-mm slice by using novel echo-volumar (EV) trajectory, also called fask-kz trajectory or spoke trajectory, the results were reported at 3T, which field inhomogeneity and intravoxel dephasing are not as severe as at ultra high field, such as 7T. More spokes have to be deployed at ultra high field in order to successfully recover signal loss, however, this will lead to increase RF pulses duration. Such lengthy RF pulses seriously hamper the temporal resolution of the MR images, which is critical in fMRI studies. In addition, because the long 3DTRF pulses are deployed in the regions with extremely inhomogeneous field, excitation accuracy can be severely affected by off-resonance excitation.

The primary drawback of three-dimensional tailored RF pulses is exceedingly long pulse duration. Parallel transmission can dramatically shorten RF pulses duration by undersampling the k-space trajectory. **Aim #3** of this dissertation is to design clinically applicable 3D tailored RF pulses that can recover signal loss caused by magnetic susceptibility difference in T_2*-weighted fMRI at ultra high field using parallel transmission. First, the magnetic susceptibility-induced field map is obtained via two sets of multi-slice 3D gradient echo (GRE) images with an echo time difference, which should be small enough so that no phase evolution during this period exceeds $\pm\pi$. Then we incorporate the set of field maps of multiple slices with time duration of TE into the small-tip-angle RF pulses design for parallel transmission. The major improvement is that multiple channels and multi-slice B_1^+ maps are simultaneously employed in the RF pulse design.

This method can be combined with aforementioned algorithms. For example, this precompensated method can be combined with PTA method to comprise the analytical framework of RF pulse design in the regime of large-tip-angle excitation. Eddy current correction method should be included to avoid the effect of hardware imperfection, such, eddy current field, delays between gradients and RF pulses. Maximal signal recovery can be obtained from the combined algorithms compared to gross precompensated algorithm. Furthermore, with the use of parallel transmission, it becomes possible that the one has previously not been practical due to the requirement of lengthy RF pulses.

In summary, the goal of this dissertation is to design effective and fast algorithms for parallel transmission, ultimately with applications in human imaging. If the aims are realized, the largest hurdle of severe B_1 field inhomogeneity at ultra high field MRI can be overcome. Ultra high field MRI will gain widespread application with homogeneous field strength due to its high SNR and contrast. Therefore, it is very meaningful to investigate novel RF pulse design algorithms for parallel transmission to bring ultra high field human MRI to clinical use.

1.3 THE STURCTURE OF THIS DISSERTATION

The structure of the dissertation is as follows:

Chapter 1 presents the specific aims of this dissertation along with the current difficulties at ultra high field. In addition, to motivate subsequent chapters, the significance of this dissertation is explained in details.

Chapter 2 describes the basic MR physics such as the generation and reception of MR signal. In addition, we introduce the parallel transmission theory and then focus on the principle of pulse design for parallel transmission including small-tip-angle and large-tip-angle excitations.

Chapter 3 describes the novel design algorithm of large-tip-angle parallel transmission RF pulses using perturbation analysis (PTA) of Bloch Equation and implementation of the algorithm on an 8-channel parallel system at 7T for both simulations and experiments, successfully demonstrating the capability of the technique in creating short pulses for localized excitation, mitigating B_1^+ inhomogeneity, and providing excitation for arbitrary target pattern. This work has been published in Magnetic Resonance in Medicine.

Chapter 4 presents an eddy current characterization technique for parallel transmission RF pulse design. This algorithm is useful to compensate the eddy current field induced from RF shield when fast switching gradients are used. The technique was verified and validated on a water phantom at 7T using an 8-channel parallel transmission system. This work has been submitted for publication in Journal of Magnetic Resonance.

Chapter 5 introduces a novel RF pulse design combining parallel transmission technology and 3D tailored RF pulse design, dubbed as PTX 3DTRF, to restore the magnetic susceptibility induced artifacts in some important functional brain regions. The algorithm is validated both on phantom and human studies. The proposed algorithm has successfully been demonstrated in whole brain BOLD fMRI studies at 7T. Significant improvement can be observed with the use of PTX 3DTRF pulse design. This work has been submitted for publication in Magnetic Resonance in Medicine.

Chapter 6 presents two practical considerations for the design of parallel transmission RF pulses especially at ultra high field. The first describes a technique to rapidly obtain B_1^+ maps of all channels of RF coils for parallel transmission at ultra high field. The spatial B_1^+ profiles of RF transmission coils are crucial inputs for parallel transmission design, which requires a technique that could be used to rapidly obtain a good estimation of these profiles. The second describes a technique to effectively compensate the excitation artifacts caused by directly discrete sampling and finite gradient raster time. These two techniques have been published in the Annual Meeting and Exhibition of International Society for Magnetic Resonance in Medicine.

Chapter 7 summarizes the major contributions of this dissertation and proposes several interesting ideas of the extensions to this dissertation as the future work.

2.0 BACKGROUND

The aim of this chapter is to provide the relevant background for understanding the work in the subsequent chapters of this dissertation. First of all, a brief description of MR physics is presented, including MR principle, signal excitation and reception. Then an outline of the RF pulse design theory for single and multiple channel excitations are followed. Finally, the focus of this chapter will be mainly on the excitation stage of MRI, including small-tip-angle and large-tip-angle parallel transmission RF pulse design.

2.1 MAGNETIC RESONANCE IMAGING

Nuclear particles like protons, electrons and neutrons have a physical property---spin. Nuclei with an odd number of protons or neutrons possess a nuclear spin angular momentum. Spins can have positive or negative signs, which corresponds to different rotating direction of angular momentum. Two or more spins with different signs can be paired together to present the net spin. In MRI, only nuclei with non-zero net spin are of importance. When in a magnetic field, spins will act like magnet dipoles that will be aligned parallel or anti-parallel to the external field, which corresponds to low or high energy levels. The magnetization arises from the difference of the numbers of nuclei between these two states and contributes to the generation of signal in MR imaging. Human body largely consists of water, hydrogen nuclei that follows the spin behaviors and thus they are the signal source of conventional MR imaging. In different regions of human body, the type and concentration of nuclei are different, for example, the white and gray matters in the brain, leading to significantly valuable soft tissue contrast for clinic MR imaging.

MR imaging can be classified as a two-stage experiment: excitation and reception. The excitation stage involves exciting magnetic moments from low-energy state to high-energy state and thus generate a detectable signal. The reception stage involves receiving the detectable signal via Farady's law of induction to transform electronic signal to images through frequency, phase and slice encoding.

In contemporary commercial scanners, three magnetic fields are usually used in MR imaging,

1) Main Field (B_0)

A static main field (B_0) applied along the positive z direction, is always present. In the absence of the main field, magnetic moments in the subjects are in random orientation. When the static magnetic field is applied, excited spins will precess at the Larmor frequency and the magnetic moments will align with the applied field. Larmor frequency (w) is linearly related to the strength of main field, i.e., $w = \gamma B_0$, where γ is the gyromagnetic ratio, which is a constant for a given nucleus. For proton MRI, gyromagneic ratio is 42.56 MHz/Tesla.

2) Gradient Field (G)

The magnetic field gradient system normally consists of three orthogonal gradient coils. Gradient coils are designed to produce time-varying magnetic fields of controlled spatial nonuniformity. The gradient system is a crucial component of MRI system because gradient fields are essential for signal localization and spatially selective excitation, as will become evident in the subsequent chapters.

3) Radiofrequency Field (B_1)

During the excitation stage, a radiofrequency (RF) with the resonance frequency of magnetic moment is applied in the transverse (x-y) plane using RF transmission coils. This pulse can create a torque that rotates magnetic moment from low energy level to high energy level, corresponding to rotate the magnetization from the longitudinal direction to the transverse direction. During the reception stage, the signal can be generated in properly oriented RF receiver coils according to the Faraday' law of induction, which states that a time-varying magnetic field will induce a voltage in a coil placed perpendicular to the direction of this magnetic field. Mathematically, the law is given by,

$$V = -\frac{\partial \Phi(t)}{dt} \tag{2.1}$$

where $\Phi(t)$ is the magnetic flux. V is the induced voltage. To determine the flux, we have to use the principle of reciprocity. Specifically, if a unit current flows in the coil, it will produce a magnetic field $B^{receive}(\mathbf{r})$ at location $\mathbf{r}$. Thus, the magnetic flux through the coil by $M(\mathbf{r},t)$ is given by,

$$\Phi(t) = \int B^{receive}(\mathbf{r}) \bullet M(\mathbf{r},t) d\mathbf{r} \tag{2.2}$$

Substituting this into Eq. (2.1),

$$V = -\frac{\partial}{\partial t} \int B^{receive}(\mathbf{r}) \bullet M(\mathbf{r},t) d\mathbf{r} \tag{2.3}$$

Note that only the transverse magnetization contributes to the signal. That is why people refer the MR signal as the transverse magnetization M_{xy}. Furthermore, the MR signal we used for reconstructing images is usually the one after demodulation of high frequency. So the MR signal is given as follows,

$$S(t) \propto \omega_0 \int B_{xy}^{receive^*}(\mathbf{r}) M_{xy}(\mathbf{r},0) e^{-t/T_2(\mathbf{r})} e^{-\Delta\omega(\mathbf{r})t} d\mathbf{r} \tag{2.4}$$

where $B_{xy}^{receive^*}$ is the complex conjugate of $B_{xy}^{receive}$, which is also called receiver sensitivity (B_1^-). For transmit sensitivity B_1^+ is implicitly included in M_{xy}. We will discuss on how to obtain sensitivity maps in the subsequent chapters, as they are crucial for parallel transmission RF pulse design.

By ignoring the T_2* effect, MR signal is proportional to the Larmor frequency, receiver sensitivity map, transverse magnetization and excited sample volume.

$$\| S \| \propto \omega_0 B_{xy}^{receive^*} M_{xy} V_s \tag{2.5}$$

Note that both Larmor frequency and M_{xy} are linearly related to the main field B_0. So if the main field increases twice, the signal should increase four times. That is why the ultra high field gains more and more interests hitherto.

2.2 RF PULSE DESIGN

2.2.1 Single Channel Transmission Theory

The time-dependent behavior of magnetic moments $\vec{M}$ in the presence of an applied magnetic field $\vec{B}_1$ can be quantitatively described by the so-called **Bloch equation**. Bloch equation can be used to determine the magnetization state following a RF pulse $\vec{B}_1$ excitation for a given initial magnetization state M_0. The goal of RF pulse design is to develop methods for designing RF pulses that rotate magnetization from an initial state at the beginning of the RF pulse, to a desired state at the end of the RF pulse. In the context of MRI, the Bloch equation takes the following general form,

$$\frac{d\vec{M}}{dt} = \gamma \vec{M} \times \vec{B}_1 - \frac{M_x \vec{i} + M_y \vec{j}}{T_2} - \frac{(M_z - M_0)\vec{k}}{T_1} \qquad (2.6)$$

where γ is the gyromagnetic ratio, T_1 and T_2 are the longitudinal and transverse relaxation time constants, and M_0 is the equilibrium state for $\vec{M}$ in the presence of B_0 only.

Equation (2.6) is nonlinear and very difficult to use in design of RF pulses B_1. However, under some circumstances such as small tip angle, ignoring T_1 and T_2, the so-called small-tip-angle approximation (29), yields the following linear equation that can be used to design RF pulses in an analytical frame.

$$M_{xy}(\vec{\mathbf{r}}) = i\gamma M_0 \int_0^T B_1(t) e^{i\vec{\mathbf{r}}\cdot\vec{k}(t)}\, dt \qquad (2.7)$$

where the k-space is defined as the time-reversed integration of the gradient waveforms. The so-called excitation k-space has different interpretation with the widespread imaging k-space notation and given by,

$$\vec{k}(t) = -\int_t^T \vec{G}(s)\,ds \tag{2.8}$$

This analytical frame provides a simple Fourier relationship between RF pulses B_1 and desired transverse magnetization M_{xy}. The RF pulses B_1 and Gradient field $\vec{G}$ can be used to control the transverse magnetization and then signal intensity at various locations of the image. This powerful express of RF excitation can be summarized as the transverse magnetization is the Fourier transform of a spatial frequency function, where gradient waveform $\vec{G}$ is traveling a path in Fourier space (so-called excitation k-space), multiplied by a spatial frequency weighting function, where B_1 describes the weighting (RF energy deposition) along the path in excitation k-space. We will revisit this formalism many times in the subsequent chapters.

Note that this analysis is derived under the small-tip-angle approximation (29). The special case of RF pulses and k-space trajectory will create good excitation profile up to a relative large-tip-angle such as 90°. This method that scales small-tip-angle analysis to accurately excite large-tip-angle is called as the linear class of large-tip-angle RF pulse design (35). These RF pulses must follow some rules, 1) B_1 deposit energy in a Hermitian-symmetry fashion, which means that for every point of RF deposited energy on the excitation k-space trajectory, there is another point symmetric about the origin with the conjugate weighting of RF deposited energy. 2) The k-space trajectory must end at the origin, where the endpoint defines the origin. This class of RF pulses is called as inherently self-refocused pulses. Under theses assumptions,

$$\theta(\vec{\mathbf{r}}) = \gamma \int_0^T B_1^*(t) e^{i\vec{\mathbf{r}}\cdot\vec{k}(t)}\, dt \tag{2.9}$$

where θ is the tip angle resulting from the concatenation of self-refocused pulses. Equation (2.9) holds when the aforementioned linear class assumptions are satisfied. For large-tip-angle excitation, the assumption contains two parts. First, k-space trajectory starts and ends at the origin of the excitation k-space. Second, k-space trajectory can be decomposed into a sequence of inherently refocused subtrajectories, each corresponding to a subpulse with a small-tip-angle. Note that not all excitation k-space trajectories can be decomposed into refocused subtrajectories. The two widespread two-dimensional excitation k-space trajectories are spiral and echo-planar (EP), which are illustrated in Fig. 2.1. Between these, only the spiral can be approximately decomposed into refocused subtrajectories. Therefore, significant errors will arise when the linear class of large-tip-angle RF pulse is applied in the EP trajectory.

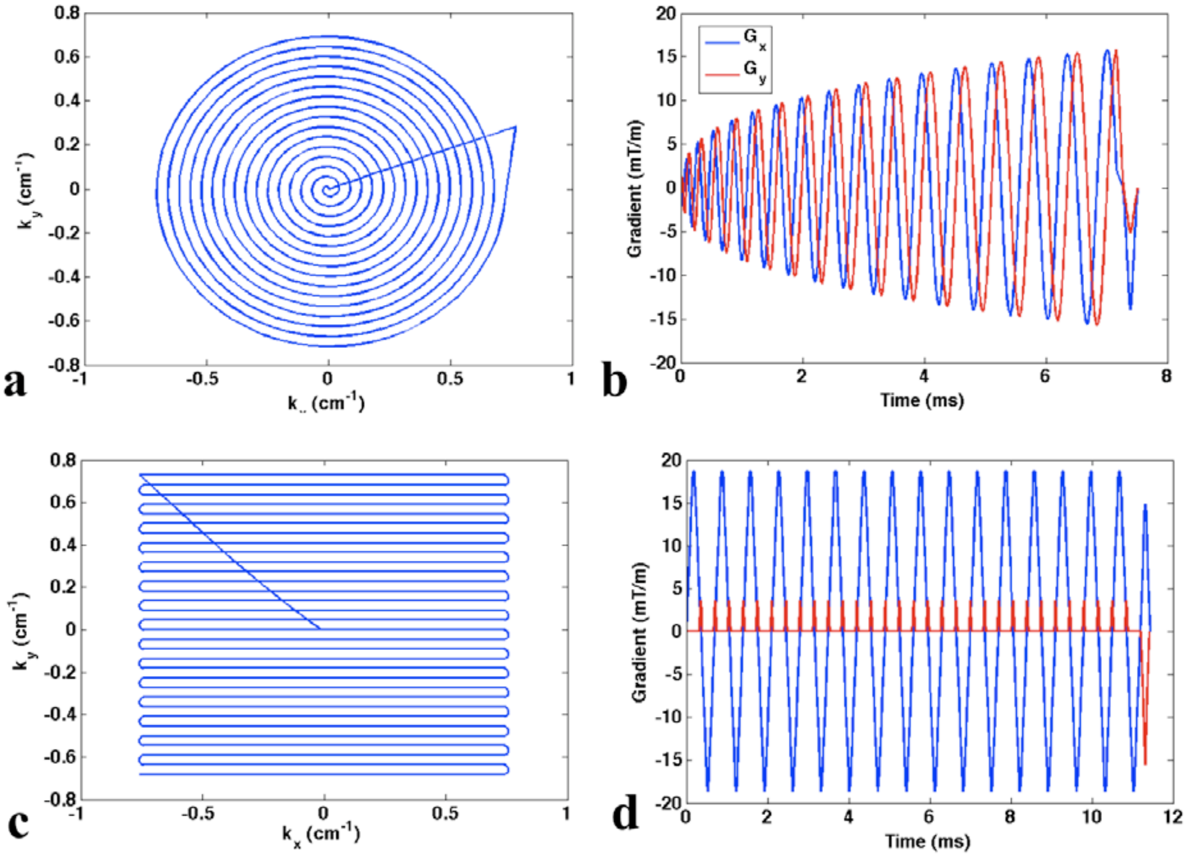

Figure 2.1 (a) Spiral k-space trajectory obtained by time-reversed integration of the corresponding gradient waveforms in (b). (c) Echo-planar (EP) trajectory and (d) the corresponding gradient waveforms.

2.2.2 Multiple Channel Transmission Theory

Heretofore, all the theories and techniques have presumed that excitation was performed with a single channel excitation. As previously demonstrated, multi-dimensional, spatially selective excitation often leads to long pulse duration that is not suitable for practical applications. Naturally, the pulse duration increases with the complexity of target patterns. For example, the selective RF excitations for mitigating severe B_1^+ inhomogeneity with the use of spoke trajectory can be very long because many spokes are required to sufficiently compensate the severe inhomogeneity in plane which inevitably results in long k-space trajectory and thus long pulse duration.

With the incidence of parallel transmission technology, the pulse duration can be significantly shortened or so-called accelerated, relative to the single channel excitation. Parallel transmission is a means of accelerating multidimensional selective excitation using multiple channel coils driven with independent waveforms (14,15). This makes it possible to excite more complex target patterns with practical pulse duration, which can be used in localized excitation and RF field inhomogeneity mitigation especially at ultra high field.

To gain the intuition of parallel transmission, the concept of B_1^+ sensitivity map should be first described. The B_1^+ sensitivity map refers to the spatial variation of the RF field produced when a coil is placed near the subject, which is dependent on the structural design and position of the coil. In the case of single channel excitation, the RF coils is designed to achieve uniformity across the space via the use of "birdcage mode" coil, however, the uniformity cannot be achieved at ultra high field, which arises the issue of RF field inhomogeneity. In the case of multiple channel transmission, RF pulses from multiple independent RF coils can excite desired target patterns via transmitting simultaneously. The B_1^+ sensitivity map of each channel is different and provides extra degrees of freedom for RF pulse design, which is the key to shorten pulse duration while maintaining the desired excitation pattern.

Mathematically, RF field produced by a single channel can be formulated as a separable function of time and space,

$$B_1(\mathbf{r},t) = S(\mathbf{r})B_1(t) \tag{2.10}$$

where $S(\mathbf{r})$ is the complex transmit sensitivity map of the single channel. By extending to multiple channels, the combined excitation field is given by,

$$B_1(\mathbf{r},t) = \sum_{n=1}^{N} S_n(\mathbf{r}) B_{1,n}(t) \tag{2.11}$$

To elucidate the concept clearly, we take the analysis under the small-tip-angle RF pulse design of single channel as an example. Substituting Eq. (2.11) into Eq. (2.7), we obtain the corresponding small-tip-angle RF pulse design of multiple channels as follows,

$$M_{xy}(\vec{\mathbf{r}}) = i\gamma M_0 \sum_{n=1}^{N} S_n(\vec{\mathbf{r}}) \int_0^T B_{1,n}(t) e^{i\vec{\mathbf{r}}\cdot\vec{k}(t)}\, dt = \sum_{n=1}^{N} S_n(\vec{\mathbf{r}}) M_n(\vec{\mathbf{r}},T) \tag{2.12}$$

where $M_n(\vec{\mathbf{r}},T)$ is the excited pattern produced by the RF pulse $B_{1,n}(t)$ of the channel n only. This expression shows that the combined excitation pattern in parallel transmission can be obtained via the summation of the excitation pattern of single channel, weighted by transmit sensitivity map of the single channel.

As previously mentioned, the use of multiple channels provides extra degrees of freedom, which allows us to undersample the excitation k-space trajectory with the same excitation accuracy as fully sampling can be achieved. Thus we can accelerate k-space trajectory and then shorten the pulse duration without sacrificing the excitation quality. This is the fundamental mechanism underlying parallel transmission. Figure 2.2 shows the examples that RF pulses using undersampled k-space trajectories can excite patterns with the same accuracy as when using a fully sampled trajectory shown in Fig. 2.1.

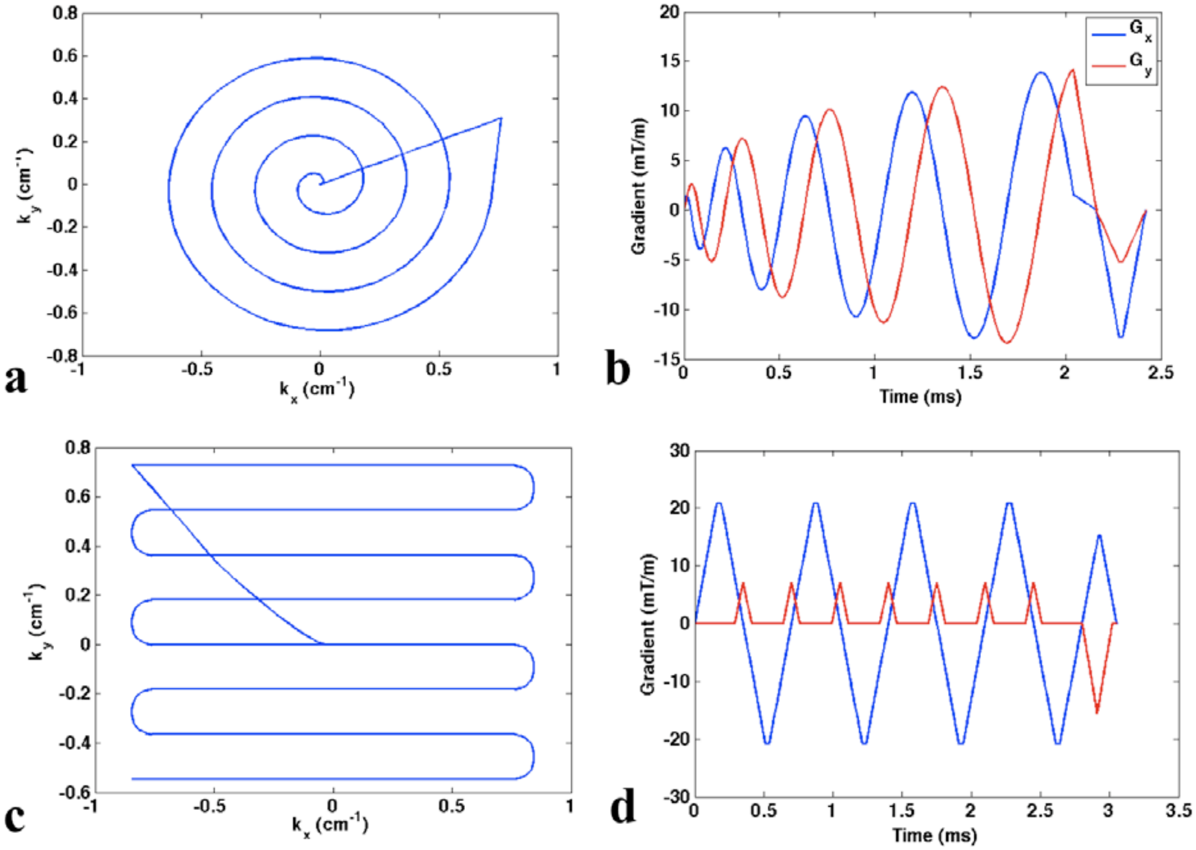

Figure 2.2 (a) Spiral k-space trajectory with undersampling or acceleration factor of 4 and (b) the corresponding gradient waveforms. (c) Echo-planar (EP) trajectory and (d) the corresponding gradient waveforms with the same acceleration factor as spiral trajectory.

2.3 PARALLEL TRANSMISSION RF PULSE DESIGN

2.3.1 Small-tip-angle Parallel Pulse Design

Several methods have been proposed for the design of small-tip-angle RF pulses in parallel transmission (14-16, 56). The pioneering pulse design methods were introduced by Katscher *et* *al* (14) and Zhu (15). Then they were followed by Griswold *et al* (56) and the most widely used method proposed by Grissom *et al* (16). We now briefly review all the methods.

1) Transmit SENSE

The method introduced by Katscher *et al* (14), called transmit SENSE, is analogous to SENSE parallel imaging and characterized by explicit use of transmit sensitivity maps in the pulse design. The mathematical formulation is based on a convolution in excitation k-space and allows using arbitrary k-space trajectories. As previous discussed, assuming that the small-tip-angle approximation is satisfied, the combined excitation simultaneously produced by multiple channels is given by,

$$P_{Tot}(\mathbf{r}) = \sum_{n=1}^{N} S_n(\mathbf{r}) P_n(\mathbf{r}) \tag{2.13}$$

where $S_n(\mathbf{r})$ is the transmit sensitivity map of channel *n*. Then, take Fourier transform of Eq. (2.13) to k-space frequency domain,

$$\tilde{P}_{Tot}(\mathbf{r}) = \sum_{n=1}^{N} \tilde{S}_n(\mathbf{r}) \otimes \tilde{P}_n(\mathbf{r}) \tag{2.14}$$

where the tilde denotes the Fourier transform operation and the operator ⊗ denotes a convolution. This equation can be discretized in space and frequency domains and concatenated as the following form,

$$\tilde{P}_{Tot}(\mathbf{r}) = [\tilde{S}_1 \cdots \tilde{S}_N] \begin{bmatrix} \tilde{P}_1 \\ \vdots \\ \tilde{P}_N \end{bmatrix} = \tilde{S}_{full} \tilde{P}_{full} \tag{2.15}$$

Then a regularized least square function can be formulated as Eq. (2.16) and solved by any classic methods for sparse linear equations such as LSQR.

$$\tilde{P}_{full} = \arg\min\left\{\| \tilde{S}_{full}\tilde{P}_{full} - \tilde{P}_{Des} \|^2 + R(\tilde{P}_{full})\right\} \tag{2.16}$$

Finally, the individual RF pulse of each channel can be obtained by taking the inverse of Fourier transform of each excited pattern of $\tilde{P}_{full}$. Since there are no any assumptions or restrictions on the sampled k-space, this method can be used for arbitrary k-space trajectories. The only issue is that it is complicated and relatively slow due to the conversion between time and frequency domains.

2) Aliasing-Removal Method

The method introduced by Zhu (15) formulates parallel transmission RF pulse design as an optimization problem in the spatial domain. The aim of this method is to solve the expected excitation pattern of each channel and subsequently obtain the RF pulse of each channel via Fourier transform. In this method, it is assumed that k-space trajectory is undersampled in one dimension. Moreover, because the method is based on the removal of aliasing in the spatial domain and aliases have to be coherent, it is restricted to Cartesian echo-planar trajectory. Therefore, significant artifacts arise when the non-Cartesian trajectories are applied such as spiral, which considerably restricts the use of this method.

3) Transmit GRAPPA

The method proposed by Griswold *et al* (56) is in manner analogous to GRAPPA parallel imaging (57). The most significant advantage of this method is that it does not require the acquisition of transmit sensitivity maps. This is a very encouraging benefit because it is not a trivial problem to accurately and rapidly measure transmit sensitivity maps, especially at ultra high field, where severe spatial variation of RF transmit field appears. However, several drawbacks of this methods hamper the practical usages. First, instead of requiring prior determination of transmit sensitivity maps, it involves an extra calibration during the pulse design. Second, it is also restricted to Cartesian echo-planar trajectories due to the acceleration via undersampling in one dimension. Last but not least, this method is based on the assumption that a relatively uniform transmit field is produced. The third assumption is the most critical because of highly inhomogeneous RF field at ultra high field. Thus this method cannot be applied for ultra high field parallel transmission applications.

4) Spatial domain method

Spatial domain method proposed by Grissom *et al* (16) is the most widely used small-tip-angle parallel transmission RF pulse design. We have already briefly described it in Section 2.2.2. Now, we rewrite (2.12),

$$M(\mathbf{r}) = i\gamma M_0 \sum_{n=1}^{N} S_n(\mathbf{r}) \int_0^T b_n(t) e^{i\mathbf{r}\cdot k(t)}\, dt \tag{2.16}$$

Then discretize time to N_t samples and space to N_s samples, we may write,

$$M(\mathbf{r}) = \sum_{n=1}^{N} D_n A b_n \tag{2.17}$$

where $D_n = diag\{S_n(\mathbf{r})\}$ is a diagonal matrix containing the transmit sensitivity map of Channel *n*. The (i,j)$_{th}$ element of the matrix A with the size of $N_s \times N_t$ is given by,

$$a_{ij} = i\gamma M_0 \Delta t e^{ir_i \cdot k(t_j)} \tag{2.18}$$

Field map can be incorporated into the element to reduce the artifact due to B_0 inhomogeneity. Equation (2.16) can be rewritten via horizontal concatenation of the matrices $D_n A$ and vertical concatenation of the vectors b_n as follows,

$$M = \left[D_1 A \cdots D_N A \right] \begin{bmatrix} b_1 \\ \vdots \\ b_N \end{bmatrix} = A_{full} b_{full} \tag{2.19}$$

Thus, the RF pulses can be obtained via solving the following least square cost function using conjugate gradient method.

$$b_{full} = \arg\min \left\{ \| A_{full} b_{full} - M_{Des} \|^2 + R(b_{full}) \right\} \tag{2.20}$$

where $R(b_{full})$ is the Tikhonov regularization term, where RF power deposition can be controlled by the tradeoff of excitation accuracy.

The form of this method is close to transmit SENSE, however, it is derived at the spatial domain, so the computation is significantly reduced due to the skip of transform to frequency domain and interpolation between k-space trajectories. This method has no restriction on the use of trajectories. Due to the robustness of this method, spatial domain method is prevailing in the parallel transmission applications.

2.3.2 Large-tip-angle Parallel Pulse Design

Pulse design is much more challenging at the regime of large-tip-angle due to the nonlinearity of the Bloch equation. Many methods have been reported for designing large-tip-angle RF pulses. Here we only cover the three most widely used large-tip-angle parallel RF pulse design methods, which are classified as non-iterative and iterative methods.

1) Non-iterative method

As mentioned in Chapter 1, linear-class large-tip-angle (LCLTA) RF pulse design for parallel transmission (34) is a dominant non-iterative method, which based on an extension of the single-channel linear-class large-tip-angle theory. The method is generally fast and involves certain approximations. The LCLTA design generalizes the small-tip-angle (STA) pulse design by concatenating a sequence of small-tip-angle excitation pulses, so it must obey some approximations, for example the k-space trajectory has to be inherently self-refocused. Thus, excitation artifacts are notable when echo-planar (EP) trajectory is applied due to the break of assumptions. Equation (2.21) is the central equation for the parallel transmission LCLTA theory,

$$\theta(\mathbf{r}) = \gamma \sum_{n=1}^{N} S_n^*(\mathbf{r}) \int_0^T b_n^* e^{-i\mathbf{r}\cdot k(t)}\, dt \qquad (2.21)$$

where the sign of star notes the operation of complex conjugate. Equation (2.21) is very close to Eq. (2.16) where the magnetization is replaced by tip angle. More strictly speaking, both STA and LCLTA are linear approximation of the nonlinear Bloch equation. They are only the first term in a perturbation expansion of the Bloch equation. We will mathematically explain this in detail with the introduction of our proposed method in Chapter 3.

2) Iterative method

With the use of LCLTA, image distortion due to the lack of the higher order terms can appear in the excited magnetization profiles even the assumptions are satisfied. Therefore, methods based on iterative scheme are proposed. Currently, two striking iterative methods for designing large-tip-angle parallel RF pulses are presented: Optimal Control Method and Additive Angle Method.

A: Optimal Control Method

Xu *et al* (37) formulated the large-tip-angle parallel transmission RF pulse design as an optimal control problem with multiple parameter controls based directly on the Bloch equation. Then a first order gradient optimization algorithm is employed to iteratively solve the optimal control problem, where the result from STA or LCLTA is used as an initial guess. This method has no restrictions on tip angles and trajectories, which was demonstrated as an effective tool to design large-tip-angle parallel transmission RF pulses. However, in the method, RF pulse design is considered as a black box without underlying physical background. Furthermore, due to lots of controlled parameters, the design is very time-consuming and memory intensive. Of most importance, this method cannot guarantee the global solution which means that it may converge to a local minimum solution of insufficient accuracy.

B: Additive Angle Method

Another iterative scheme is Additive Angle (AA) method proposed by Grissom *et al* (38). Because we will compare our Perturbation Analysis (PTA) method to this method in Chapter 3, we review its derivation here.

Firstly, assuming that $[b_1 \ \cdots \ b_n]$ are pulses of small-tip-angle excitation, the excited profile by these pulses can be approximated by,

$$\theta(\mathbf{r})e^{i\angle M_{xy}(\mathbf{r})} = i\gamma\Delta t\sum_{n=1}^{N} S_n(\mathbf{r})\sum_{j=1}^{N_t} b_{n,j}e^{-i\mathbf{r}\cdot k(t_j)} \qquad (2.22)$$

where $\theta(\mathbf{r})$ is tip angle profile and $\angle M_{xy}(\mathbf{r})$ denotes the phase of transverse magnetization, other parameters are defined the same as above. It is assumed that the pulses $[b_1 \ \cdots \ b_n]$ cannot excite desired pattern and the difference between desired pattern and excited pattern

$$\Delta\theta(\mathbf{r})e^{i\angle M_{xy}(\mathbf{r})} = i\gamma\Delta t\sum_{n=1}^{N} S_n(\mathbf{r})\sum_{j=1}^{N_t}\Delta b_{n,j}e^{-i\mathbf{r}\cdot k(t_j)} \tag{2.23}$$

As previously mentioned, the pulses Δb_n can be solved via conjugate gradient method with regularization terms including previous pulses b_n, which is given by,

$$[\Delta b_1 \ \cdots \ \Delta b_n] = \arg\min\{\| \sum_{n=1}^{N} D_n A \Delta b_n - \Delta d \|^2 + \lambda \sum_{n=1}^{N} \| b_n + \Delta b_n \|^2\} \tag{2.24}$$

where the difference between desired and excited patterns is $\Delta d = \Delta\theta \bullet e^{i\angle M_{xy}}$ and λ denotes the regularization parameter that controls the tradeoff between excitation accuracy and power deposition. To make further improvement, the procedure is repeated iteratively to update the pulses via $[b_1 + \Delta b_1 \ \cdots \ b_n + \Delta b_n]$ until accuracy stops improving or the criterion is met.

In summary, Additive Angle Method is based on a series of iterative updates of small-tip-angle pulses to design large-tip-angle pulse. The deviation between the initial guess of small-tip-angle excitation and the desired pattern is expected. Then another small-tip-angle excitation is supposed to bring the pattern excited by summed pulses closer to the desired pattern. The summed pulse is then seeded to the next iteration, and the procedure is continuing until a convergence criterion is met. In comparison, Additive Angle Method is faster than Optimal Control Method due to its formulation of a series of small-tip-angle pulse designs. However, it also utilizes the linear relationship to approximate the nonlinear Bloch equation, so notable excitation error appear particular at high acceleration in echo-planar (EP) trajectory. Thus, it is necessary to derive RF waveforms directly from the Bloch equation and design effective and fast algorithm for large-tip-angle RF pulses for parallel transmission. This analysis motivated us to explore a novel algorithm for designing large-tip-angle parallel transmission RF pulses as shown in Chapter 3.

3.0 PERTURBATION ANALYSIS METHOD FOR LARGE-TIP-ANGLE PARALLEL RF PULSE DESIGN

3.1 INTRODUCTION

In this chapter, we propose a fast and efficient large-tip-angle RF pulse design method for parallel transmission in ultra high field MRI. As it is known, parallel transmission (14, 15) provides an effective and comprehensive means to implement complex tailored radiofrequency (RF) excitation for a wide range of MRI applications. While the fundamental framework for the design of complex RF excitations was introduced many years ago (29), the resulting RF pulses were too long for practical implementation on multidimensional selective excitation (58, 59, 60). In PTX, the use of multiple simultaneous RF channels allows shortening the duration of the RF pulse by a factor that increases with the number of independent RF channels being used. This leads to practical RF pulse designs that can be used as the foundation for improved imaging applications.

Under the Small Tip Angle (STA) approximation (29) the relationship between the desired excitation pattern and the required RF pulses can be easily estimated using the methodology introduced by Grissom *et al* (16). This methodology provides an analytic expression relating the desired excitation pattern to each of the independent RF pulses in the design. The solution of the ensuing set of equations can be obtained by a variety of means, though typically methods such as the conjugate gradient yield an acceptable solution. The STA-based method (16, 61) can only be applied under the STA approximation, and it is not very effective for the design of large tip angle excitations, such as inversion and refocusing, in which case it often yields significant errors in the excitation profile (16, 31).

When the desired flip angle is large, the simple analytic expression quoted above no longer yields adequate results and other means of solution are required. One approach is to use non-linear optimization algorithms to essentially "search" through the parameter space for a solution based on the minimization of a cost functional reflecting some of the desired properties in the excitation profile and the RF pulses (37). Another approach is the so-called additive angle (AA) technique (38) in which the difference between the target magnetization profile and that produced by the STA is used to drive an iterative algorithm.

In this chapter, we evaluate the use of a new approach for PTX pulse design that is based on a perturbation analysis of the Bloch equation and recently introduced as the PTA method (62). In this approach, the difference between the target magnetization profile and that produced by the STA can be analytically expressed as a function of the applied RF pulses. This analytical expression can then be used to calculate corrections for the applied RF pulse in an iterative fashion. We demonstrate with simulations as well as experimental results that this approach leads to faster computation and improved excitation quality during PTX pulse design.

3.2 THEORY

3.2.1 Analytic Framework

In the rotating frame, for a multidimensional spatial selective excitation, the Bloch equation, without relaxation terms, and including the radiofrequency (RF) $B_1(t) = B_{1,x}(t) + iB_{1,y}(t)$ and gradient fields $\boldsymbol{G}(t) = [G_x(t) \;\; G_y(t) \;\; G_z(t)]^T$ simultaneously applied can be written as follows:

$$\begin{bmatrix} \dot{M}_x(\mathbf{r},t) \\ \dot{M}_y(\mathbf{r},t) \\ \dot{M}_z(\mathbf{r},t) \end{bmatrix} = \gamma \begin{bmatrix} 0 & \boldsymbol{G}(t)\bullet\mathbf{r} & -B_{1,y} \\ -\boldsymbol{G}(t)\bullet\mathbf{r} & 0 & B_{1,x} \\ B_{1,y} & -B_{1,x} & 0 \end{bmatrix} \times \begin{bmatrix} M_x(\mathbf{r},t) \\ M_y(\mathbf{r},t) \\ M_z(\mathbf{r},t) \end{bmatrix} \tag{3.1}$$

where $[M_x \;\; M_y \;\; M_z]^T$ represents the x, y, z components of the magnetization vector at spatial location $\mathbf{r} = [x \;\; y \;\; z]^T$ at time t and γ is the gyromagnetic ratio of the excited nucleus. Eq. (3.1) can be used to determine the magnetization state following a RF excitation for a given initial magnetization state $[M_x^0 \;\; M_y^0 \;\; M_z^0]^T$. The goal of RF pulse design is to develop methods for designing RF pulses that rotate the magnetization from an initial state at the beginning of the RF pulse, to a desired state at the end of the RF pulse.

The proposed method is derived directly from a perturbation analysis to the Bloch equation and it is analogous in concept to the ‘Additive Angle’ method of Grissom et al. (11). We first write the transverse magnetization in complex form, $M_{xy} = M_x + iM_y$, use the excitation k-space notation and follow the same manipulations (integration factors and k-space notation) used in the seminal paper of Pauly et al. (3) to obtain the following “formal” solution to the Bloch equation:

$$M_{xy}(\mathbf{r},T) = i\gamma \int_0^T M_z(\mathbf{r},t) B_1(t) e^{i2\pi \boldsymbol{k}(t)\cdot \mathbf{r}} dt \tag{3.2}$$

$$M_z(\mathbf{r},T) = M_0 + \gamma \int_0^T [\vec{M}_{xy}(\mathbf{r},t) \times \vec{B}_1(t)]_z \, dt \tag{3.3}$$

where $[\vec{M}_{xy}(\mathbf{r},t) \times \vec{B}_1(t)]_z$ denotes the scalar z-component of the vector cross product between $[M_x \;\; M_y \;\; 0]^T$ and $[B_{1,x} \;\; B_{1,y} \;\; 0]^T$. Combining Eq. (3.2) and Eq. (3.3), we can write the transverse magnetization as follows,

$$M_{xy}(\mathbf{r},T) = i\gamma M_0 \int_0^T B_1(t) e^{i2\pi \boldsymbol{k}(t)\cdot \mathbf{r}} dt + i\gamma^2 \int_0^T [\int_0^t [\vec{M}_{xy}(\mathbf{r},\tau) \times \vec{B}_1(\tau)]_z \, d\tau] \cdot B_1(t) e^{i2\pi \boldsymbol{k}(t)\cdot \mathbf{r}} dt \tag{3.4}$$

Equation (3.4) readily illustrates the inherent non-linear dependence of the Bloch equation on the excitation RF and can also be used to illustrate the errors introduced when the STA method (3) is used. Essentially, the contribution of the non-linear term in Eq. (3.4) is neglected. A corollary of this expression is that the expected error when the STA is used can also be estimated by calculating an upper bound for the second term in Eq. (3.4).

To derive the formulae used for the proposed method we first include the sensitivity maps in Eq. (3.2) (i.e. $B_1(t)$ becomes $\sum_{n=1}^{N} S_n(\mathbf{r}) b_n(t)$):

$$M_{xy}(\mathbf{r},T) = i\gamma \sum_{n=1}^{N} S_n(\mathbf{r}) \int_0^T M_z(\mathbf{r},t) b_n(t) e^{i2\pi \boldsymbol{k}(t)\cdot \mathbf{r}} dt \tag{3.5}$$

If we now denote by M_{xy}^D the desired transverse magnetization and by M_{xy}^p the excited transverse magnetization at spatial position $\mathbf{r}$ created by RF pulses $B_1\{b_1,...,b_N\}$ and $B_1^p\{b_1^p,...,b_N^p\}$ respectively, we have,

$$M_{xy}^D(\mathbf{r},T) = i\gamma \sum_{n=1}^{N} S_n(\mathbf{r}) \int_0^T M_z^D(\mathbf{r},t) b_n(t) e^{i2\pi \boldsymbol{k}(t)\cdot \mathbf{r}} dt \tag{3.6}$$

$$M_{xy}^{p}(\mathbf{r},T) = i\gamma \sum_{n=1}^{N} S_n(\mathbf{r}) \int_0^T M_z^{p}(\mathbf{r},t) b_n^p(t) e^{i2\pi \mathbf{k}(t)\cdot\mathbf{r}} dt \tag{3.7}$$

Subtract Eq. (3.7) from Eq. (3.6), and denote $\Delta M_{xy} = M_{xy}^{D} - M_{xy}^{p}$, $\Delta B_1\{\Delta b_1,\ldots,\Delta b_N\} = B_1\{b_1,\ldots,b_N\} - B_1^p\{b_1^p,\ldots,b_N^p\}$ we can obtain the following equation (see the Appendix),

$$\begin{aligned}\Delta M_{xy}(\mathbf{r},T) = {}& i\gamma \sum_{n=1}^{N} S_n(\mathbf{r}) \int_0^T M_z^{p}(\mathbf{r},t) \Delta b_n(t) e^{i2\pi \mathbf{k}(t)\cdot\mathbf{r}} dt \;+\; i\gamma \sum_{n=1}^{N} S_n(\mathbf{r}) \int_0^T \Delta M_z(\mathbf{r},t) b_n^p(t) e^{i2\pi \mathbf{k}(t)\cdot\mathbf{r}} dt \\ &+\; i\gamma \sum_{n=1}^{N} S_n(\mathbf{r}) \int_0^T \Delta M_z(\mathbf{r},t) \Delta b_n(t) e^{i2\pi \mathbf{k}(t)\cdot\mathbf{r}} dt\end{aligned} \tag{3.8}$$

where M_z^p represents the longitudinal magnetization created by $B_1^p\{b_1^p,\ldots,b_N^p\}$, $\Delta M_z = M_z^D - M_z^{p,j} \approx M_z^{p,j+1} - M_z^{p,j}$ (j denotes the number of iteration) is the difference between the longitudinal magnetization created by $B_1^p\{b_1^p,\ldots,b_N^p\}$ + $\Delta B_1\{\Delta b_1,\ldots,\Delta b_N\}$ and by $B_1^p\{b_1^p,\ldots,b_N^p\}$, respectively, and **k**(t) is, once again, the excitation k-space trajectory as defined in Ref. (3). Eq. (3.8) illustrates the nonlinear relationship between the error in the magnetization profile ΔM_{xy} and the desired correction pulse ΔB_1 (ΔM_z depends on ΔB_1). Note that by dropping the last two terms and setting $M_z^p = M_0$ (essentially linearizing the first term in Eq. (3.8)) the AA method (11) is obtained. Consequently, the use of these correction terms represents the most significant difference between the PTA method and the AA method.

3.2.2 Numerical Solution

In the PTA approach, both M_z^p and ΔM_z are known by numerically solving the Bloch equation, thus Eq. (3.8) is used for designing RF pulses by minimizing the following cost function,

$$\Delta B_1\{\Delta b_1,\ldots,\Delta b_N\} = \underset{\Delta b_n}{argmin}\left\{\|\sum_{n=1}^{N} S_n(\mathbf{r})(M_z^p + \Delta M_z)A\Delta b_n - \Delta M_{xy}^{new}\|_{\mathbf{W}}^2 + \beta\sum_{n=1}^{N}\| b_n^p + \Delta b_n \|^2\right\} \tag{3.9}$$

$$\Delta M_{xy}^{new} = \Delta M_{xy} - \sum_{n=1}^{N} S_n \Delta M_z A b_n^p \tag{3.10}$$

Here, the matrix A incorporates the Fourier kernel $\exp(i2\pi\boldsymbol{k}\mathbf{r})$ for the k-space traversal and field map corresponding to B_0 inhomogeneity. The W is a spatial error weighting mask that can be used to specify a region of interest (ROI). The regularization parameter β is used to balance between RF power and excitation error. The minimization problem can be solved by using the Conjugate Gradient (CG) method. Because no approximations are applied, the proposed method is not restricted by flip angles and/or k-space trajectories.

In the algorithm considered here, we use an initial set of RF pulses calculated via the STA parallel pulse design method in Ref. (7), to excite an initial transverse magnetization. The difference between this initial magnetization and the target magnetization profile is then calculated and used as the driving term in Eq. (3.8). The “corrected” RF pulses $B_1^p\{b_1^p,\ldots,b_N^p\} + \Delta B_1\{\Delta b_1,\ldots,\Delta b_N\}$, are then used to drive a Bloch equation solver so that the required time-dependent terms in Eq. (3.8) are calculated and the process is repeated until a tolerance criterion is achieved. During the iterative solution, it is not necessary to constrain the phase of the transverse magnetization since the phase information is already incorporated in the expression for the transverse magnetization. During the iterations, the regularization parameter β effectively balances the excitation accuracy and RF power, and, therefore, cannot be set in an arbitrary fashion. Specifically, the regularization parameter β is adjusted each iteration using the ‘L-curve’ method (13), albeit at the expense of an increase in the computational time. This computational time, however, can be effectively managed by allowing the regularization parameter to be constrained within a prescribed range.

3.3 METHODS

3.3.1 B_1 Mapping

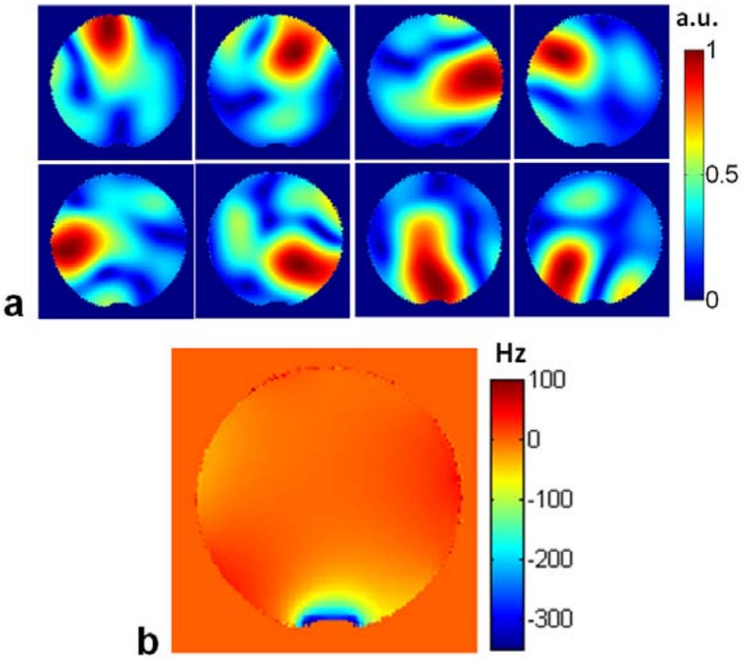

Figure 3.1 Magnitude of water phantom B_1+ map (a) and field map (b) used in the simulations of eight-channel parallel excitation.

One of the more important ingredients for effective PTX pulses design is the rapid and accurate mapping of the B_1^+ profiles of the transmit coil array in both experimental phantoms and humans. A technique similar to the multiple angle method proposed by Setsompop *et al* (64) was employed to estimate the B_1^+ profiles. This technique relied on RF transmission via slice-selective excitation for a set of voltages, namely, 30V, 60V, 90V, 120V and 150V, and fitting of the resulting sinusoidal signal intensity on pixel-by-pixel basis. A standard nonlinear fitting algorithm in the MATLAB toolbox was employed to perform the aforementioned fit and the desired B_1^+ profiles were extracted from the “apparent” frequency of the sinusoid. The total acquisition time for B_1^+ mapping of the eight channels was about 24 minutes. An example of the B_1+ profiles for the phantom is presented in Fig. 3.1a.

3.3.2 Main Field Inhomogeneity (ΔB_0) Mapping

FLASH sequence with TE1=3.7 ms and TE2=4.7 ms, respectively, was used to estimate the B_0 map, and incorporate its value into the RF pulse design (16, 38, 65) and reduce the effects of magnetic field inhomogeneities while improving the robustness of the RF pulse design. This B_0 compensation proved particularly useful during the use of high acceleration in PTX. The measured B_0 map is shown in Fig. 3.1b.

3.3.3 Pulse Design

Two-dimensional RF pulses were designed using the STA (16), AA (38) and PTA methods, respectively, and the results compared using computer simulations as well as experimental data. The desired pattern was a rectangle of 4.5 × 9 cm^2 on a 64 × 64 grid, within a FOV of 20 × 20 cm^2. The RF pulses were smoothed with a Gaussian filter in order to reduce Gibbs ringing artifact in the excitation patterns. When evaluating the performance of the RF pulse designs, the difference between the target and excited magnetizations was computed over the entire excited slice. Maximizing the spin excitation within the excited patterns and minimizing the spin excitation everywhere else were simultaneously implemented. We used the Root-mean-square error (RMSE) defined as $RMSE = \frac{1}{N_s}\sqrt{\sum_{i=1}^{N_s} | M_{xy}^{D} - M_{xy}^{p} |^2}$ with ROI masked between the desired and excited patterns to evaluate the accuracy. Both the additive angle and perturbation analysis designs were initialized with small tip angle designed pulses, with the same tip angle and with 50 CG iterations. A regularization parameter β of 10 was chosen. All pulse designs and simulations were performed in MATLAB 2009a (Mathworks, Natick, MA).

3.3.4 Computer Simulation

RF pulses were designed using spiral (SP) and echo-planar (EP) excitation k-space trajectories, respectively. Spiral trajectories were outward with maximum gradient amplitude of 40 mT/m and maximum slew rate of 150 mT/m/ms. PTX acceleration was achieved by undersampling the k-space trajectories in the radial direction. The EP trajectories were designed using maximum gradient amplitude of 36mT/m and maximum slew rate of 120 mT/m/ms. For the EP trajectories, acceleration was achieved by undersampling along the phase-encoding dimension. In all cases, the acceleration factor (R) was defined as the number of interleaved trajectories. To test the effectiveness of the proposed method, acceleration factors of 2, 3, 4, 5 and 6 for both spiral and EP trajectories were used. Likewise, excitation patterns with flip angles of 90 and 180 degrees were also used. Inversions as well as refocusing pulses were designed. The initial magnetization was set along the +z and +y axes for the inversion and refocusing pulses, respectively.

3.3.5 Experimental Data Acquisition

All experiments were performed on a Siemens 7T Magnetom scanner (Erlangen, Germany) equipped with an 8-channel parallel transmit (PTX) RF system and a gradient set with maximum amplitude of 40mT/m and maximum slew rate of 170 mT/m/ms. An 8-channel transmit/receive volume birdcage coil was used for all experiments. The phantom used for the experimental data acquisition consisted of an 8cm diameter sphere filled with 1.25 g/liter of nickel sulfate and 5 g/liter of sodium chloride.

For experimental data acquisition, spiral design with acceleration factors of 2, 4 and 6, were used. The nominal flip angle was 90^o for all experiments. The data were acquired with a 2D gradient recalled echo (GRE) sequence using the following parameters: matrix= 64 × 64, FOV= 20×20 cm^2, voxel resolution =3.125×3.125 mm^2. Repetition time (TR) =700 ms, echo time (TE) =2.41 ms, slice thickness = 5.0 mm and bandwidth =300 Hz/pixel. In order to minimize scanning time, we employed partial Fourier on both phase and slice directions (6/8 partial Fourier). Variable density spiral designs (66) with an undersampling factor of 2 were also used to reduce the SAR and allow achieving the transmission voltages to remain within the limits required by the RF coil.

For each method of pulse design (i.e., STA, AA and PTA) transmission voltages were calibrated through non-linear fitting of the sinusoidal signal intensity in a data set with varying excitation (30V, 60V, 90V, 120V and 150V) on an experimental phantom. The transmission voltages for different methods were obtained by simply scaling the RF pulses. The estimated voltages for a 90^o flip angle were 70V, 118V and 132V for STA, AA and PTA, respectively.

3.4 RESULTS

3.4.1 Selective Excitation

Figure 3.2 shows simulated excitation patterns produced by selective 90^o excitation pulses for a spiral trajectory using the STA, AA and PTA methods with various acceleration factors (R=2, 4, 6). At low acceleration (R=2, Fig. 3.2a, d and g), the STA-designed pulses yield an inaccurate pattern both in excitation strength and spatial orientation. The small tilt seen in the STA result is a direct result of the limited raster resolution on the time domain for the gradient waveforms and could, incidentally, be corrected by a small time shift of the RF waveforms (which can be sampled at a higher temporal resolution). By contrast, the excitation patterns produced by AA and PTA methods are very close to the desired targets. At medium acceleration (R=4, Fig. 3.2b, e and h), the excited pattern produced by AA begins to show evidence of decreased homogeneity that is not apparent on the results from the PTA technique. At hgh acceleration (R=6, Fig. 3.2c, f and i), the pattern excited by STA pulses is severely distorted. For this acceleration the inhomogeneity in the AA results has increased with obvious excitation errors clearly present outside the target excitation region as well. By contrast, the PTA method is still able to yield satisfactory results despite the reduction in RF pulse length.

When the EP trajectory is used, the resulting excitation pattern is well behaved along the readout direction (left to right). However, excitation errors are readily apparent along the phase encoding direction. This is especially obvious at high acceleration (R=6, Fig. 3.3c, f, and i), where even for the additive angle method there are large excitation errors. The use of the PTA approach under these conditions leads to improved results.

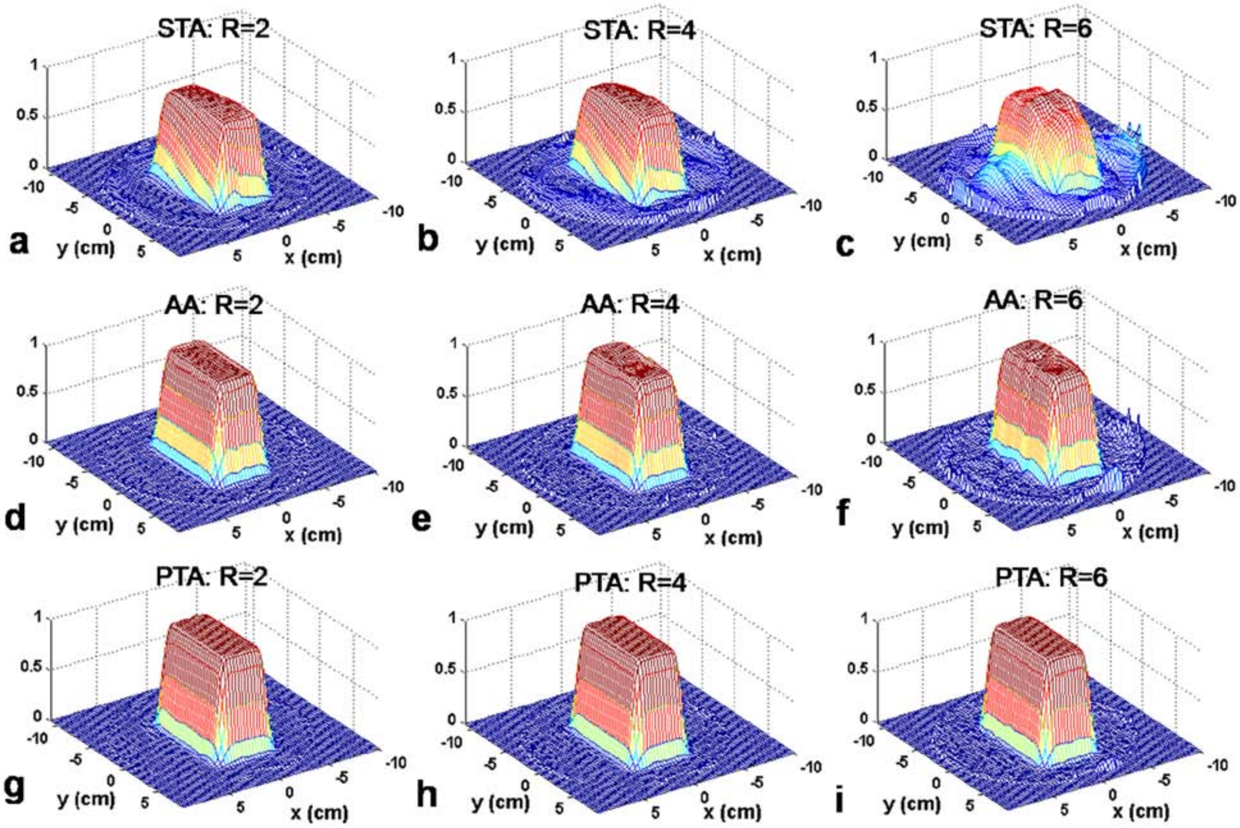

Figure 3.2 2D selective 90^o excitation pulses for a spiral trajectory with various acceleration factors R= 2, 4, 6, respectively. a-c: The transverse magnetization produced by Small Tip Angle (STA) method. d-f: The transverse magnetization produced by Additive Angle (AA) method. g-i: The transverse magnetization produced by Perturbation Analysis (PTA) method.

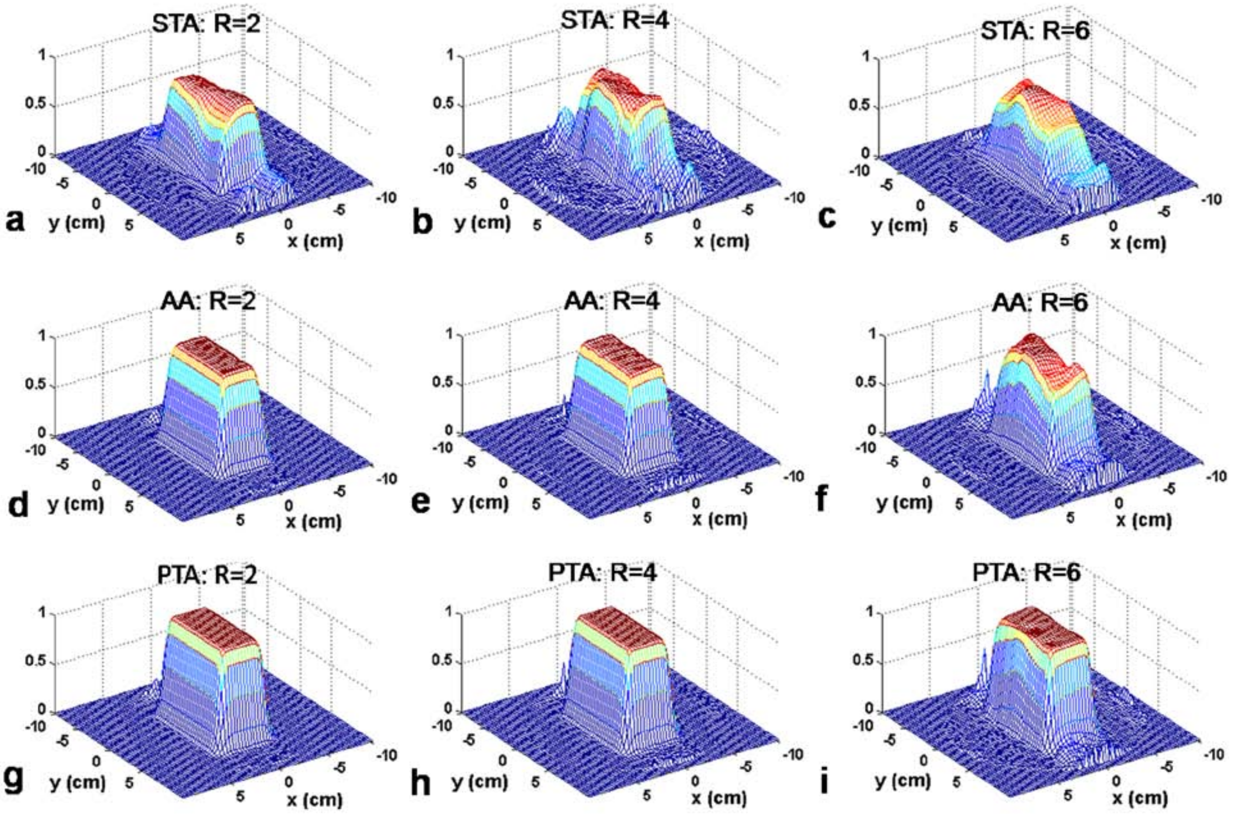

Figure 3.3 2D selective 90^o excitation pulses for an EP trajectory with various acceleration factors R= 2, 4, 6, respectively. a-c: The transverse magnetization produced by Small Tip Angle (STA) method. d-f: The transverse magnetization produced by Additive Angle (AA) method. g-i: The transverse magnetization produced by Perturbation Analysis (PTA) method.

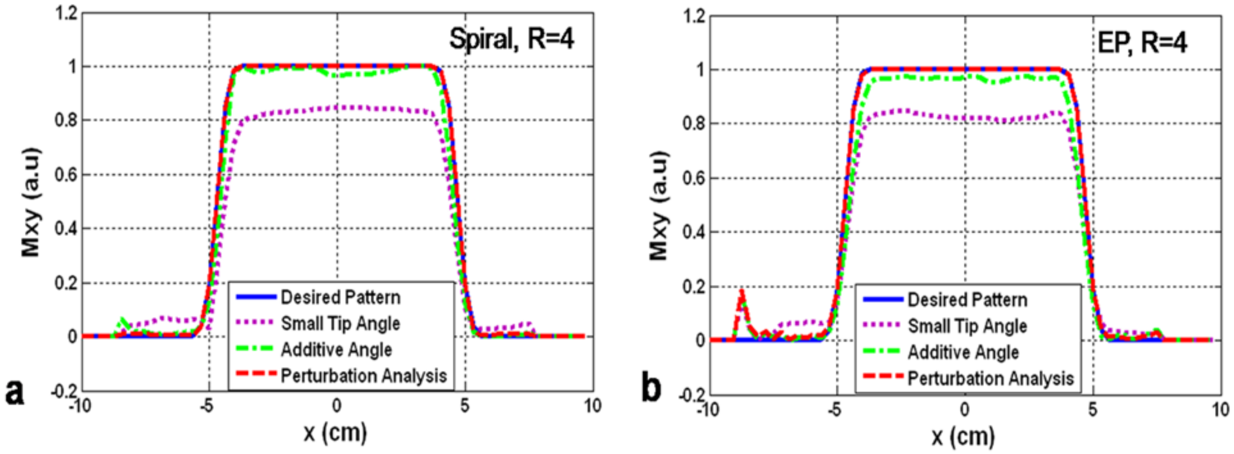

Figure 3.4 Transverse magnetization profiles taken through the center of the excited patterns in Figure 3.2 for spiral trajectory (a) and in Figure 2.3 for EP trajectory (b) with acceleration factor R=4 using Small Tip Angle method, Additive Angle method and Perturbation Analysis method, respectively.

A more in-depth depiction of the quality of the excitation patterns is presented on the line plots of Figs. 3.2 and 3.3. Here, a comparison of the profiles along the midline of the excitation patterns is presented for all the results. Notably, the STA designed pulses yield consistently poor profiles for both the spiral and EP trajectories. Improvements to the STA approach are clearly achieved using the AA method, though the bandwidth narrowing effect previously described by Grissom *et al* (38) and Pauly *et al* (67) is clearly present along the phase encoding direction (Fig. 3.4b). Excitation errors due to inaccuracies in the field map on the superior aspect of the phantom are also clearly depicted in Fig. 3.3e and h. In all cases, marked improvements in excitation accuracy are obtained through the use of the PTA technique. Figure 3.5 presents a comparison of excitation accuracy and peak RF magnitude for the AA and PTA methods over a range of acceleration factors. In Fig. 3.5a, it is shown that smaller RMSE can be achieved with the PTA method for both spiral and EP trajectories over the entire range of acceleration factors. In Fig. 3.5b, the graphs demonstrate that the peak magnitudes for the pulses designed by the AA

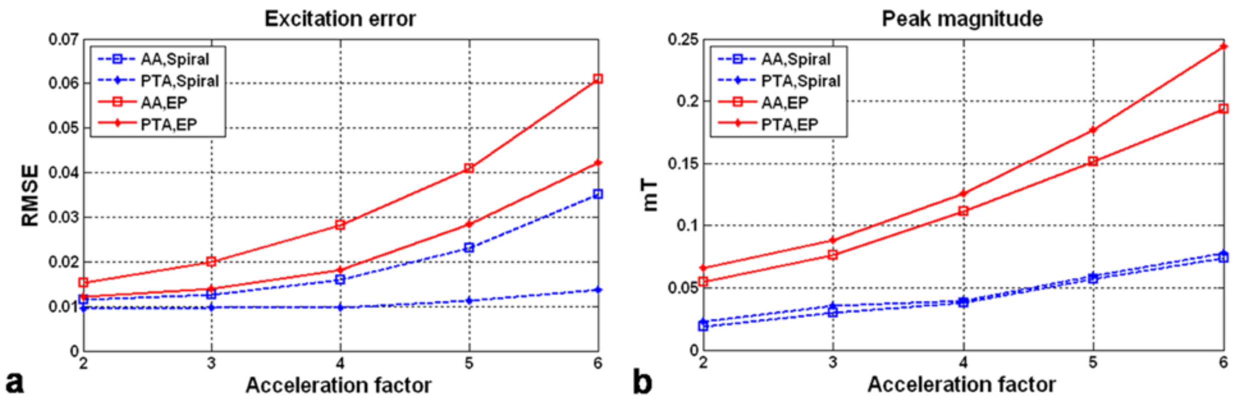

Figure 3.5 Comparison of excitation accuracy (a) and peak RF magnitude (b) between 90^o excitation pulses designed Additive Angle method and Perturbation Analysis method at various acceleration factors R=2, 3, 4, 5, 6.

and PTA methods at different acceleration factors are almost identical when the spiral trajectory is used; however, the PTA method yields pulses with slightly higher peak amplitude than the AA technique. Consequently, the RF pulses designed with the PTA method achieve lower excitation errors without a significant increase in peak magnitude over the entire range of acceleration factors.

Figure 3.6 shows the sum of magnitude of the eight RF pulses using an acceleration factor of 4 and for spiral and EP trajectories, respectively. Significant changes in the pulse shape result from the corrections of the excitation errors. The pulse durations in the spiral and EP cases were 1.92 ms and 3.22 ms, respectively. Note that for the EP case the RF pulses had zero amplitude during the blips along the phase encoding direction.

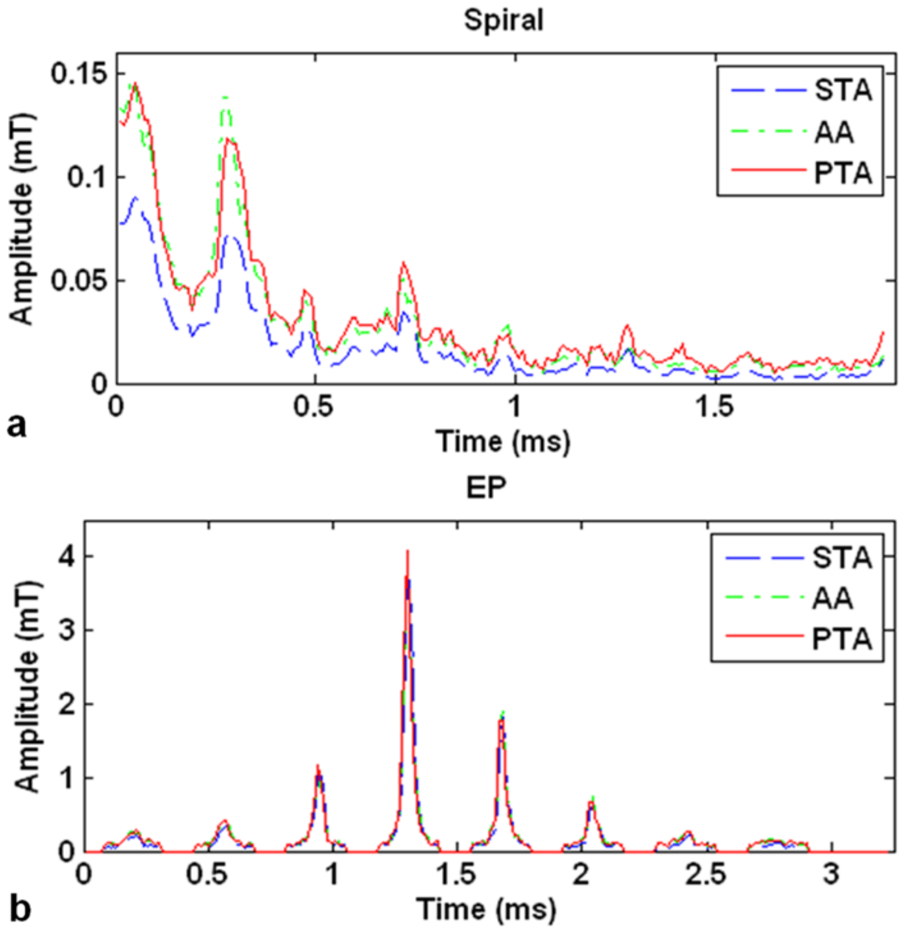

Figure 3.6 Sum of magnitudes of eight channel 90^o excitation RF pulses at acceleration factor R=4 (a) in the spiral case and (b) in the EP case.

3.4.2 Inversion

Figure 3.7 presents selective 180^{o} inversion pulses intended to invert the rectangle pattern used above when using spiral and EP trajectories with acceleration factor R=4. The initial magnetization vector is along +z direction at all spatial locations. Fig. 3.7a-c show the M_x, M_y and M_z magnetization profiles excited by the inversion pulses designed using the AA method with a spiral trajectory. The M_x component stays close to zero at most regions, but some magnetization flips over and leads to large excitation errors. For the M_y component, most of the magnetization is kept close to zero over the entire field of view (Except near the edge of the pattern). The M_z component is well inverted inside the desired pattern despite the small distortions within the target pattern. These distortions are almost completely corrected by the PTA method (Fig. 3.7d-f), though there are only minor improvements for the M_x, M_y components for both methods.

The excited M_x and M_y components have very similar behavior using the RF pulses designed by the AA and PTA methods when an EP trajectory is used (Fig. 3.7g, h, j, and k). However, the M_z component generated by the AA and PTA techniques (Fig. 3.7i) suffers from more severe distortions than the ones obtained using the spiral trajectory (Fig. 3.7c). A minor improvement in these distortions is clearly obtained when the PTA method is used.

3.4.3 Refocusing

Theoretically, an ideal refocusing pulse rotates the transverse component of the magnetization by 180 degrees (e.g., a magnetization pointing along +y direction is transformed into one pointing along –y direction) (37, 68). Fig. 3.8a and b presents a comparison of 180^{o} refocusing pulses for

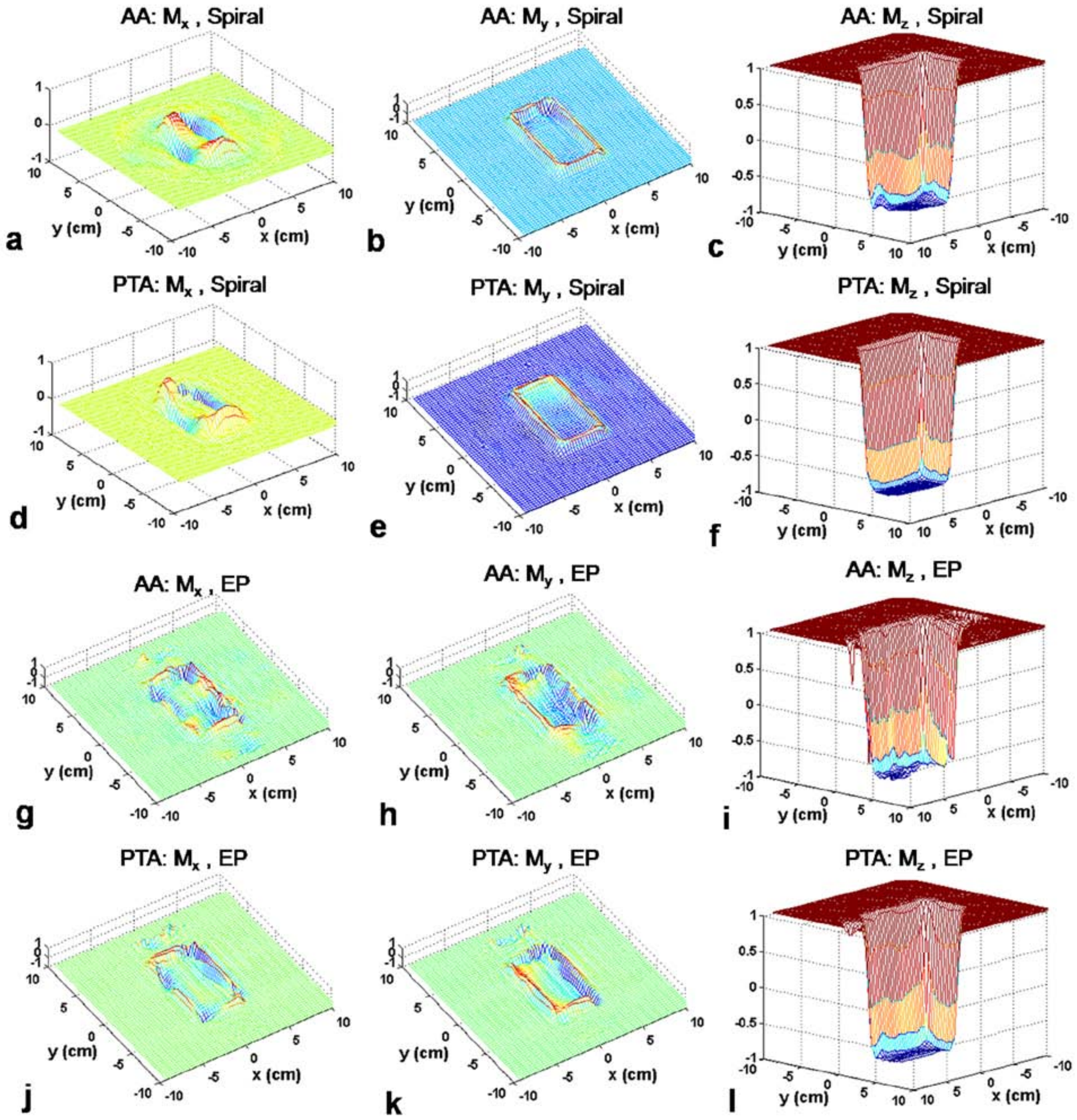

Figure 3.7 2D selective 180^o inversion pulses for spiral and EP trajectories with acceleration factor R=4. a-f: Mx, My and Mz components of magnetization profiles produced by Additive Angle (AA) method and Perturbation Analysis (PTA) method for a spiral trajectory. g-l: Mx, My and Mz components of magnetization profiles produced by Additive Angle (AA) method and Perturbation Analysis (PTA) method for an EP trajectory.

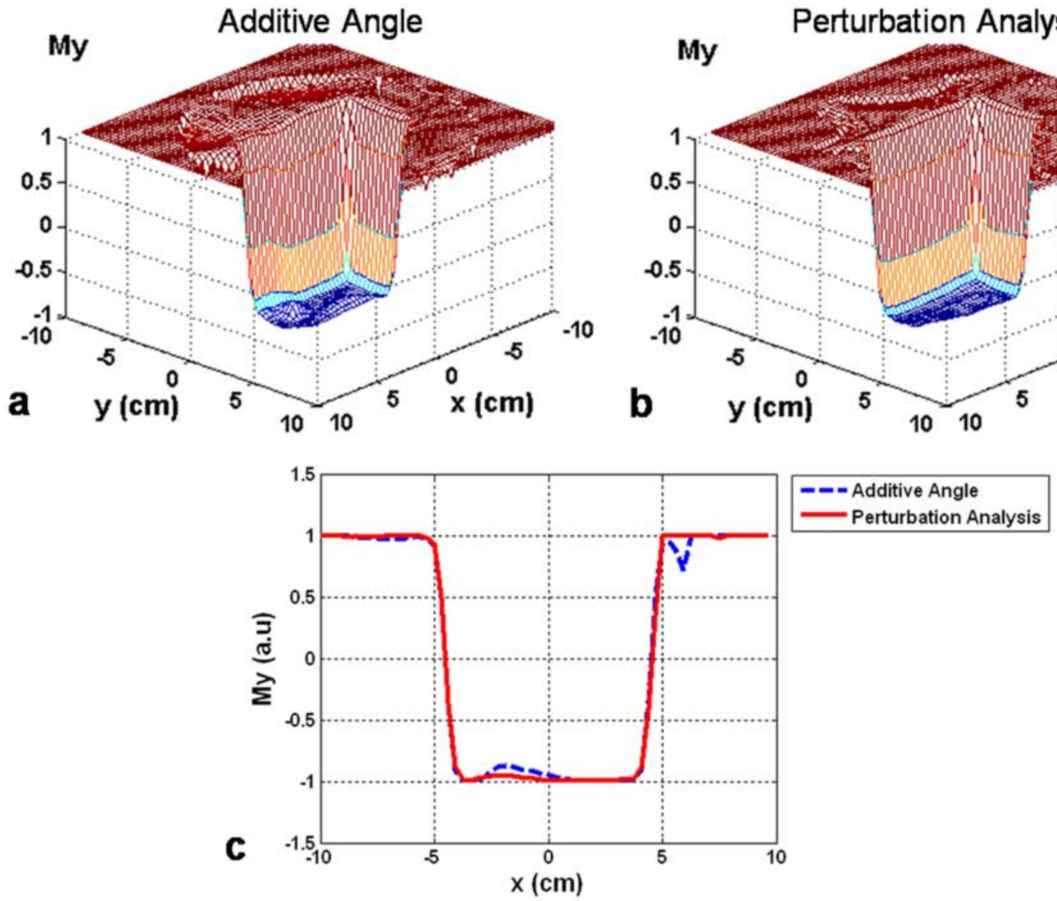

Figure 3.8 2D selective 180^{o} refocusing pulses for a spiral trajectory with acceleration factor R=4 designed using Additive Angle method (a) and Perturbation Analysis method (b). c: Transverse magnetization profiles taken through the center of the excited patterns from (a) and (b).

a spiral trajectory with an acceleration factor of 4 designed with the AA and PTA methods, respectively. Just as in the aforementioned example, some of the excitation errors obtained with the AA method (e.g., non-uniformity within the target block) are corrected through the use of the PTA techniques. The plot presented in Fig. 3.8c provides a more quantitative depiction of these variations in the form of a line profile through the centerline of the 2D excitation pattern for both methods.

3.4.4 Scanner Experiment

Figure 3.9 shows the experimental results obtained on the water phantom. Excitation patterns for the same target magnetization as in the simulations above are presented when the STA, AA and PTA methods are used with acceleration factors R=2, 4 and 6. The corresponding line profiles are also shown in the right panels of this figure (Fig. 3.9d, h and l). For low acceleration (R=2, Fig. 3.9a-c), the pattern excited by the STA pulses shows the same tilt observed in the simulation results (Fig. 3.2a-c). Likewise, the magnetization amplitude is lower than that of the desired pattern. As in the simulation results, for low accelerations, there is virtually no difference in the excitation patterns produced by the AA and PTA methods. At medium acceleration (R=4, Fig. 3.9e-g), the STA excitation pattern is still tilted and the magnetization amplitude deviates further from that the target pattern. The use of the AA method improves the amplitude of the magnetization although there are noticeable inhomogeneities within the target area. These inhomogeneities are successfully corrected through the use of the PTA method (Fig. 3.9h). At high acceleration (R=6, Fig. 3.9i-k), the excited magnetization profile by the STA method is severely distorted. These distortions are only partially corrected by the AA method and are further improved through the use the PTA method. Examination of the line profiles shown in

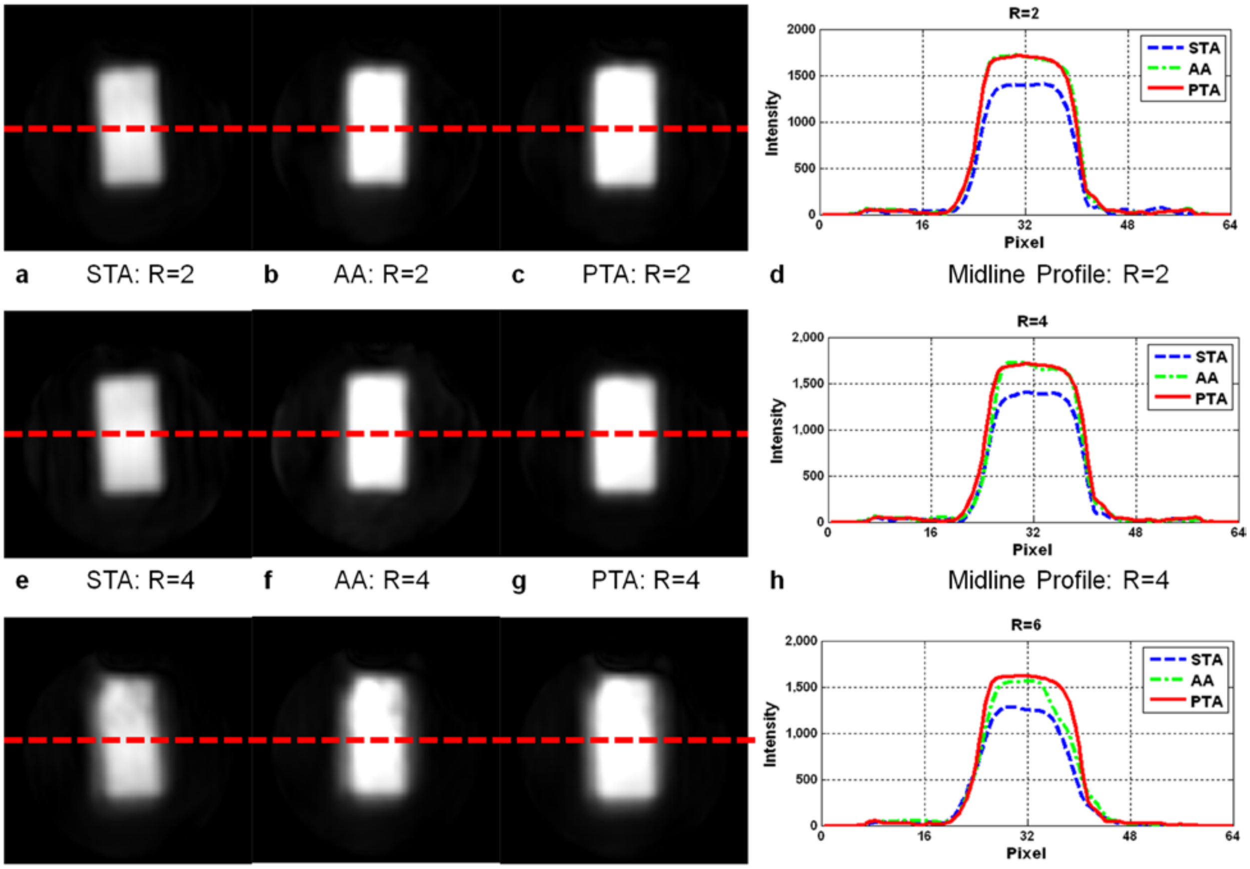

a STA: R=2 **b** AA: R=2 **c** PTA: R=2 **d** Midline Profile: R=2

e STA: R=4 **f** AA: R=4 **g** PTA: R=4 **h** Midline Profile: R=4

i STA: R=6 **j** AA: R=6 **k** PTA: R=6 **l** Midline Profile: R=6

Figure 3.9 Experimental results of magnitude images of the water phantom excited via Small Tip Angle method (a, e, i), Additive Angle method (b, f, j) and Perturbation Analysis method (c, g, k) for a spiral trajectory with corresponding transverse magnetization profiles (d, h, l) taken through the midline of the excited patterns with acceleration factors R=2, 4, 6, respectively.

Fig. 3.9d, h and l, further illustrates that the magnetization amplitude obtained by all three methods is always lower than its target value when high acceleration are used. This is an expected result since the excitation error increases with the increase of acceleration factor because lower tolerance for excitation error in the experimental parameters is not fully controlled during the experiments (gradient imperfections, B_1 and B_0 inhomogeneities, etc).

3.5 DISCUSSION

We have successfully presented a novel method for spatially selective large-tip-angle parallel RF excitation and demonstrated its use for large-tip-angle gradient echo, inversion-recovery and spin-echo for parallel transmission at ultra-high field (i.e., 7T). The technique presented here is similar in concept to the AA technique introduced by Grissom *et al* (38), but yields improved results at higher acceleration factors for the same computational time (number of iterations) due to its exact analytical nature. In this work, we have chosen to implement the solution to the PTA equations using an iterative algorithm for the sake of computational efficiency. However, other means to seek the solution, such as using nonlinear optimization techniques (e.g., Optimal Control algorithm (37, 69)) can also be used, albeit at the expense of using a general purpose optimization routine that does not shed much light into the dynamics of the system. For the iterative method used here, we have found that the regularization parameter has a significant effect on excitation accuracy and that specifically, in order to maintain the same excitation error the number of iterations must be increased when large regularization parameters are used.

Another feature of the method presented above is that by evaluating the second term of Eq. (3.4), the deviations from nonlinearity could be prospectively evaluated and used as a guide for the selection of the appropriate numerical technique used during its solution. Linearization schemes will yield improved results when the nonlinear component of the equation is small and nonlinear optimization technique could be preferred when this is not the case. The effect of trajectory design could also be evaluated in this fashion. This particular observation is useful when interpreting the improved performance of all methods when spiral trajectories are used since this trajectory choice leads to linear-class conditions (34, 35) that are well-suited for the iterative techniques used here. When the EP trajectories are used this conditions are not met leading to decreased excitation accuracy when any of the methods presented here are used. Consequently, a nonlinear optimization approach for the solution of Eq. (3.4) might be a better numerical choice under such conditions.

Though the proposed method is desirable in terms of excitation quality, it is an iterative method and, therefore, computationally complex. The computational time for the PTA and AA methods is devoted to two main steps, namely, the solution of the model equations and the evaluation of the Bloch equation. Currently, using MATLAB (Mathworks, Natick, MA, USA) on a MacBook Pro (Apple Computer, Cupertino, California) with a 2.33 GHz Intel Pentinum 2 Duo and 3 GB RAM, the evaluation of the Bloch equation typically amounts to 25-35 seconds per iteration. The solution of the model equations, on the other hand, requires 15 seconds and 10 seconds for the PTA and AA methods, respectively. Consequently, although the PTA pulse design method requires a longer computational time per iteration than the AA method, its faster convergence (10 iterations vs. 15 iterations, for the examples considered here) makes it an attractive and practical alternative due to its lower overall computational time. It should be pointed out that such computational times do not represent a major practical burden for these techniques as recent reports have shown how the Graphics Processing Units (GPU) found on consumer-grade computational hardware can be used to significantly accelerate the solution of the model equations (70).

Using PTX, the RF pulses calculated could lead to high peak RF magnitudes that might not be well-suited for routine implementations on human subjects. However, during the numerical solution of the problem using the iterative techniques shown above, the regularization parameter can be used effectively to reduce the peak RF magnitudes, albeit at the expense of a larger excitation errors or a longer computational time (more iterations) if the size of this excitation error is to be constrained. Lee *et al* (71) has successfully extended the variable-rate selective excitation (VERSE) (72) for the reduction of peak RF magnitude and demonstrated a consistent increased in pulse durations. The use of this approach for PTX SAR reduction needs to be carefully evaluated since with increased pulse length the effects of eddy currents and off-resonance must be prospectively mitigated (39). Also, because VERSE increases the sampling density near the center of k-space, the effective acceleration factor for PTX is lower than its nominal value. Finally, the transmission voltages of the AA and PTA pulses are both larger than those for the STA pulses, This is a common finding for all current iterative algorithms for PTX, including the Optimal Control Algorithm (37), Therefore, further detailed work is still needed in order to develop fast and effective algorithms for constraining SAR while at the same time achieving low excitation errors during large-tip-angle parallel transmission pulse design.

3.6 CONCLUSIONS

We have demonstrated an exact formulation for the inversion of the Bloch equation during PTX RF pulse design. Through the use of iterative solution of the resulting equations we have demonstrated, using simulated as well experimental results, that the proposed formulation can be used to obtain improved excitation patterns relative to other existing iterative pulse design techniques. Experimental results agreed well with the theoretical calculations and demonstrated the improvements in excitation patterns that can be obtained through a complete account of the intervening terms in the solution of the Bloch equations.

4.0 PARALLEL TRANSMISSION RF PULSE DESIGN FOR EDDY CURRENT CORRECTOIN IN ULTRA HIGH FIELD

4.1 INTRODUCTION

In the previous chapter, we have developed a novel method for designing large-tip-angle parallel transmission RF pulses. As it is well known, multidimensional spatially selective RF pulses (29, 35) have been proposed in a wide range of MRI applications, including localized excitation (58), spatially selective saturation (73), B_1 inhomogeneity correction (7, 8) and B_0 inhomogeneity correction (25). However, one major drawback of multidimensional RF pulses is their long pulse duration (tens of milliseconds). The effects of relaxation and off-resonance can significantly limit the practical applications, which are more obvious at ultra high field due to shorter relaxation time and larger B_0 inhomogeneity. Recently, parallel transmission (PTX) (14, 16, 74) has been demonstrated as one of the effective means to overcome theses limitations, allowing for shortening RF pulse duration without sacrificing the performance of spatial excitation. A number of successful demonstrations have been reported at high field or ultra high field (30, 64).

Nonetheless, the performance of parallel transmission can be severely impeded by various hardware system imperfections. One of the major practical issues is from eddy current field. Previous work with conventional single channel transmission system have been demonstrated that eddy current field can be produced from gradient coils and various methods such as using shield gradients (41), pre-emphasis system (42), and k-space trajectory measurement (43), have been proposed to eliminate or minimize their effects for imaging and excitations. One of less discussed source of eddy currents is from the RF shield with fast switching gradients. RF shield, as those used in a transverse electromagnetic (TEM) coil, can significantly improve the transmitter efficiency and reduce the specific absorption rate (SAR), which is particularly relevant for ultra high field applications (75). RF shield design has been proposed to reduce eddy currents (76). Nevertheless, the effect of the remnant eddy current field can still introduce significant errors in parallel excitation that relies on actual k-space trajectory such as spiral or echo planar imaging (EPI). Wu *et al* (40) recently proposed and demonstrated the use of a k-space trajectory measurement to reduce the eddy currents effects for parallel excitation applications. However, since the k-space trajectory has to be re-measured whenever the nominal gradient waveform is modified, this approach is greatly limited for use in routine PTX applications.

In this work, we demonstrate a model-based eddy current compensation method that relies on eddy current characterization (77-79) for mitigating their effects to improve the performance of PTX RF pulse design as well as accounting for potential system delays. With this approach, eddy current characterization needs to be performed only one time. Once the eddy current field is characterized, the eddy current distortions for any given gradient waveforms can be subsequently predicted using the established model and RF pulse design to provide the required compensation. In what follows we describe the methodology used for the characterization of the eddy current field and RF pulse design approach for compensating the eddy current effects. The performance of the proposed algorithm is then demonstrated on phantom studies using a Siemens 7 Tesla whole body scanner equipped with an eight-channel PTX system and also compared between unshielded and shielded RF coils.

4.2 THEORY

4.2.1 Eddy Currents Model and Measurement

The eddy current field can be characterized as the superposition of multiple exponential terms, which represent the Taylor expansion of eddy current field. Higher-order terms are usually not considered due to their insignificant effects compared to linear terms and also difficult to measure and compensate (79, 80). The effect of eddy current field is spatially dependent and can severely distort the k-space trajectory. In addition to the effect from eddy currents, system delay exists between gradient waveforms and RF pulses. This delay can also hinder the performance of PTX excitation (40). Therefore, RF pulses that are designed using an ideal k-space trajectory cannot always excite the desired spatial distribution.

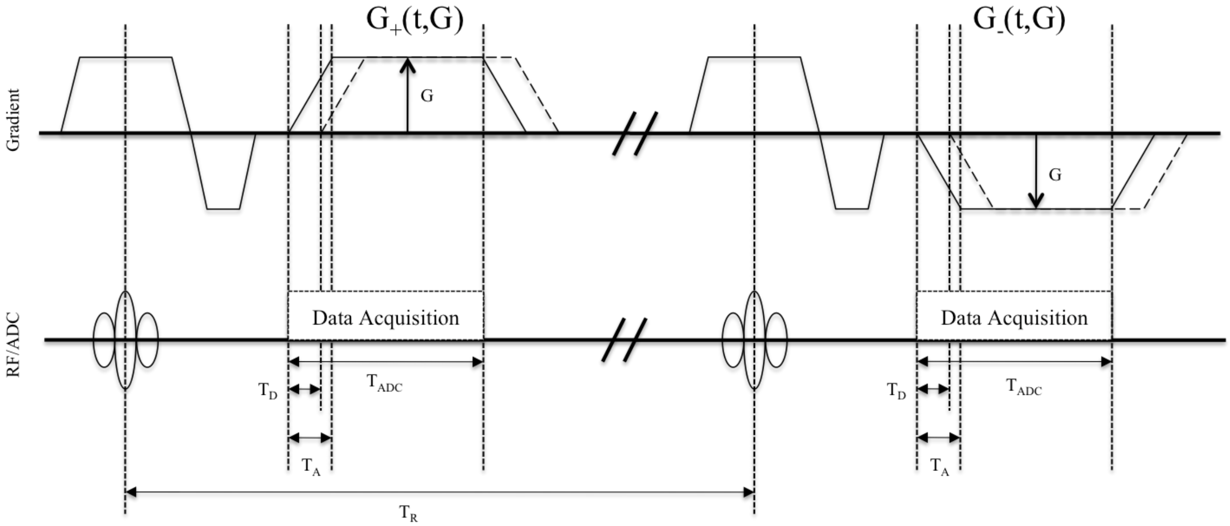

Figure 4.1 Pulse sequence diagram to characterize the system constants. Data are acquired from multiple slice locations and multiple gradient amplitudes at each slice location. Slice selection and readout are performed on the same physical gradient and then measured for each physical gradient direction. The solid and dashed lines indicate the nominal and actual gradient waveforms, respectively.

According to previously described eddy current models (80), the eddy current field $G_E(t)$ induced by a nominal gradient waveform $G_D(t)$ can be described as the convolution of the eddy current impulse response function H(t) and the negative time derivative $-dG_D(t)/dt$ of the nominal gradient waveform $G_D(t)$.

$$G_E(t) = -\frac{dG_D(t)}{dt} \otimes H(t) \tag{4.1}$$

where the eddy current impulse response function H(t) can be modeled as the sum of multiple exponential terms (77, 78) that are characterized by amplitude α_n and time constant τ_n as the followings,

$$H(t) = u(t)\sum_{n=0}^{N-1} \alpha_n e^{-t/\tau_n} \tag{4.2}$$

where u(t) is the unit step function.

The method proposed by Atkinson *et al* (79) is employed to completely characterize the system delay and B_0 and linear eddy currents. This method is similar to that proposed by Duyn *et al* (81), but rather than measuring the imaging trajectories, the gradient waveforms shown in Fig. 4.1 are applied at multiple slice locations and multiple gradient amplitudes and the system constants describing the eddy currents can be computed from the phase of the measured data. The problem of solving system constant, including system delay and eddy current coefficients (amplitude constants and time constants), can be formulated as the constrained minimization problem. Data are acquired by applying calibration gradient waveforms multiple times at different amplitudes and slice locations. Then the full set of system constants can be obtained by using iterative nonlinear fitting method to solve the aforementioned minimization problem for each physical gradient.

The pulse sequence shown in Fig. 4.1 is used to acquire data from a thin slice centered at x_0, and then the normalized difference of the data phase is,

$$\begin{aligned}\eta(x_0,t,G) &= \frac{\Phi_+(x_0,t,G)-\Phi_-(x_0,t,G)}{2\gamma} \\ &= x_0\int_0^t (G_D(t,G)+G_L(t,G))\,dt + \int_0^t B_0(t,G)\,dt\end{aligned} \tag{4.3}$$

where $\Phi_+(x_0,t,G)$ and $\Phi_-(x_0,t,G)$ are the phases of the data collected during $G_+(t,G)$ and $G_-(t,G)$, respectively, γ is the gyromagnetic ratio of the excited nucleus, $G_D(t,G)$ is the delayed gradient, and $G_L(t,G)$ and $B_0(t,G)$ are the magnetic fields due to the linear and B_0 eddy currents, respectively.

Using Eqs. (4.1) and (4.2), the three integral terms on the right side of Eq. (4.3) can be computed, respectively,

$$\int_0^t G_D(t,G)\,dt = \begin{cases} 0 & t < T_D \\ 0.5\bullet(t-T_D)^2 \dfrac{G}{T_A} & T_D \le t \le T_D + T_A \\ G(t-0.5\bullet T_A - T_D) & T_D + T_A \le t \end{cases} \tag{4.4}$$

$$\int_0^t G_L(t,G)\,dt = -\sum_{n=0}^{N_L-1} \alpha_n^{(L)} \rho(t,\tau_n^{(L)},G) \tag{4.5}$$

$$\int_0^t B_0(t,G)\,dt = -\sum_{n=0}^{N_0-1} \alpha_n^{(0)} \rho(t,\tau_n^{(0)},G) \tag{4.6}$$

where, the common term

$$\rho(t,\tau,G)=\begin{cases}0 & t<T_D\\ \dfrac{G}{T_A}\tau(t-T_D)-\dfrac{G}{T_A}\tau^2(1-e^{-(t-T_D)/\tau}) & T_D\le t\le T_D+T_A\\ G\tau-\dfrac{G}{T_A}\tau^2(1-e^{-T_A/\tau})-\dfrac{G}{T_A}\tau^2(1-e^{T_A/\tau})(e^{-T_A/\tau}-e^{-(t-T_D)/\tau}) & T_D+T_A\le t\end{cases} \tag{4.7}$$

and N_0 and N_L are the number of multiple acquisitions (i.e., multiple slice positions and multiple gradient amplitudes) for B_0 and linear eddy current models, respectively.

If data are acquired for N_s slices, with the sth slice centered at x_s, and N_G gradient amplitudes for each slice location, with the gth gradient amplitude of G_g, then the system delay and linear and B_0 eddy currents coefficients can be found by solving the following constrained minimization problem,

$$\min:\sum_{g=0}^{N_G-1}\sum_{s=0}^{N_S-1}\left\|\eta_{\text{model}}(x_s,t,G_g)-\eta_{\exp}(x_s,t,G_g)\right\|^2 \tag{4.8}$$

The full set of system constants (i.e., amplitude constants and time constants) for each physical gradient are then obtained using an iterative nonlinear fitting method. With the system constants, we can estimate the impulse response function H(t) according to Eq. (4.2). Then the eddy current gradient $G_E(t)$ can be predicted using Eq. (4.1). Finally, the actual gradient waveform can be obtained by summing up nominal gradient G_D and eddy current gradient G_E.

4.2.2 RF Pulse Design

In this chapter, parallel transmission RF pulses were designed in the regime of small tip angle using the method proposed by Grissom *et al* (16), which extends the linear small-tip-angle approximation (29) to parallel transmission system and controls RF power via regularization terms. Under the regime of small tip angle, the excitation pattern can be written as follows.

$$\mathrm{m}(\boldsymbol{x}) = \mathrm{i}\gamma \mathrm{m}_0 \sum_{\mathrm{r}=1}^{\mathrm{R}} \mathrm{S}_{\mathrm{r}}(\boldsymbol{x}) \int_0^{\mathrm{T}} \mathrm{b}_{\mathrm{r}}(\mathrm{t}) \mathrm{e}^{\mathrm{i}\boldsymbol{k}(\mathrm{t})\cdot \boldsymbol{x}} \mathrm{e}^{\mathrm{i}\gamma \Delta \mathrm{B}_0(\boldsymbol{x})\cdot(\mathrm{t}-\mathrm{T})} \mathrm{dt} \tag{4.9}$$

where R is the number of coils; T is the pulse duration; S_r and $b_r(t)$ are the spatial sensitivity map (B_1^+ map) and RF pulse waveform of coil r, respectively; ΔB_0 is field map that represents static field inhomogeneity. The trajectory k(t) is defined as the time reversed integration of gradient waveform. Equation (4.9) is then discretized in time and space and written in matrix form $\mathbf{m}(x)=\mathbf{A}*\mathbf{b}(t)$. RF pulses $\mathbf{b}(t)$ can be obtained by solving the following minimization cost function,

$$\mathbf{b}(\mathrm{t}) = \arg\min_{\mathbf{b}} \{ \|\, |\mathbf{A}\mathbf{b}| - \mathbf{m} \,\|_{\mathbf{w}}^2 + \lambda \| \mathbf{b} \|^2 \} \tag{4.10}$$

where **m** is the target magnetization; A incorporates the excitation k-space trajectory, ΔB_0 and B_1^+ maps; vector $\mathbf{b}(t)$ represents the complex RF pulses waveform of all channels; W is a spatial error weighting mask that can be used to specify a region of interest (ROI). The regularization parameter λ is used to balance between RF power and excitation errors. The minimization problem can be solved by using magnitude least square optimization (61). To improve the performance of the algorithm, correction terms are incorporated to compensate for the error associated with the finite gradient raster time (82). Due to the mismatch between nominal and actual gradient waveforms, the corresponding nominal and actual trajectories will be obviously discrepant. Therefore, the resulting uncorrected and corrected RF pulses will be significantly different.

Once the model parameters are determined, the performance of the proposed model-based method is verified by comparing the excitation patterns generated by RF pulses designed with the nominal gradient (G_D) and model-corrected actual gradient (G_D+G_E), respectively (regularization parameters (λ) of 10 and flip angle of 10^o) over a range of acceleration factors. In all cases, main magnetic field map correction is incorporated to exclude the effects of magnetic field inhomogeneity.

4.3 METHODS

4.3.1 B_1 and ΔB_0 Mapping

In parallel transmission, rapid and accurate mapping of the B_1^+ profiles of transmit coil array is one of the most important ingredients for the effectiveness of PTX pulse design in both phantom and human experiments. B_1^+ map (magnitude and phase) of each individual channel was obtained with a novel fast B_1^+ mapping method for PTX applications introduced by Zhao *et al* (83). This method can efficiently estimate B_1^+ maps for parallel transmission only using the images obtained from one small-tip-angle excitation. The detailed formulation for the method is included in Chapter 6. In this method, B_1^+ maps were obtained by sequentially transmitting through each RF channel while always receiving through all available receive channels. 2D GRE sequence with the following parameters: TR/TE = 200ms/2.51ms, flip angle = 10^o, bandwidth per pixel =1500 Hz/pixel, FOV = 220 mm and matrix size = 64 × 64 was used for this purpose (total scan time was 1min 12sec for mapping the B_1^+ maps of all channels). This B_1^+ mapping method produced accurate B_1^+ maps within very short imaging time, making the proposed PTX calibration practical for human experiments.

FLASH sequence with TE_1=3.7 ms and TE_2=4.7 ms, respectively, was used to estimate the B_0 map, which, as mentioned above, was purposely incorporated into the RF pulse design (61) in order to reduce the effect of off-resonance on the RF pulse design. This frequency offset compensation of field map proved particularly crucial in the context of ultra high field due to its large field inhomogeneity.

4.3.2 Eddy current effects on different coils

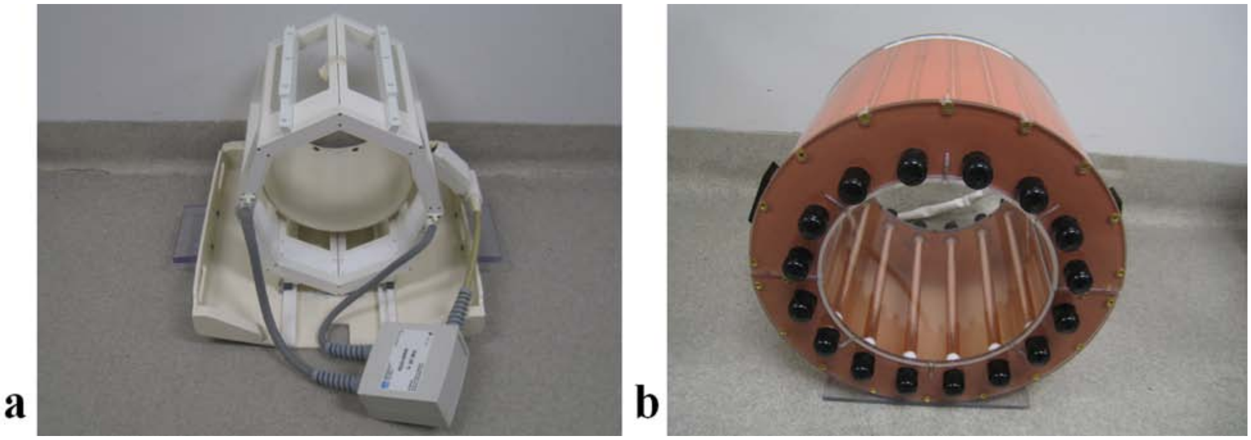

Figure 4.2 Different coils to illustrate different eddy current effects between unshielded and shielded RF coils. (a) Siemens commercial birdcage coil (unshielded RF coil) and (b) TEM coil (shielded RF coil).

In order to illustrate eddy current effects between unshielded and shielded RF coils, the same experiments were performed using a decoupled birdcage coil (unshielded RF coil) and a TEM coil (shielded RF coil), respectively. Figure 4.2 shows the Siemens commercial birdcage coil and 4-channel transmit/receive TEM coil. Spiral and echo planar (EP) k-space trajectories were employed during the design of the spatially selective excitations. PTX acceleration was, therefore, achieved by undersampling the radial direction of the k-space trajectory in the spiral case and undersampling the blip direction of the k-space trajectory in the EP case. RF pulses were designed using nominal and model-corrected gradient waveforms, respectively.

4.3.3 Model-based method vs trajectory measurement method

We compared excitation performance and time efficiency between the model-based model method and k-space trajectory measurement method. Similar to Takahashi *et al* (43) and Wu *et al* (40), k-space trajectory was extracted from measured raw data by locating the peak position at each time point along the self-encode dimension and then fitting with a second-order polynomial to find the maximum position. To minimize noise impact, ten data acquisitions were averaged before extracting k-space trajectories, yielding a total acquisition time of around 7 minutes for both G_x and G_y. And the two are measured independently. In order for fast measurement, it is assumed that there are no significant cross-terms between Gx and Gy, These trajectories were also smoothed by Gaussian function before calculating their time derivative to obtain the measured waveforms. In addition, baseline k-space trajectories were acquired by running the same acquisition but without implementing the gradient waveforms. These baseline which represents B_0 inhomogeneity, would be subtracted from the measured data before the computation of actual gradient waveforms. The accuracy of this method replies on the number of encoding steps along the phase direction. More steps lead to higher accuracy but at the expense of increased acquisition time. Gradient waveforms of model-based method and trajectory measurement method were illustrated and compared with nominal gradient waveform.

4.3.4 Numerical simulations

RF pulses were designed using spiral and EP excitation k-space trajectories, respectively. Spiral trajectory was designed with maximum gradient amplitude of 36 mT/m and maximum slew rate of 150 mT/m/ms. PTX acceleration was achieved by undersampling the k-space trajectories in the radial direction. EP trajectory was designed with maximum gradient amplitude of 30 mT/m and maximum slew rate of 120 mT/m/ms. For the EP trajectory, acceleration was achieved by undersampling along the phase-encoding dimension. In both cases, the acceleration factor (R) was defined as the number of undersampling rate and approximately equal to the reduction rate of pulse duration. To demonstrate the effectiveness of the proposed method, acceleration factors of 1, 2, 3 and 4 for both spiral and EP trajectories were compared. When evaluating the performance of RF pulse design, the difference between the target and excited magnetizations was computed over the entire excited slice. Maximizing the spin excitation within the excited patterns and minimizing the spin excitation everywhere else were simultaneously implemented. We used the Normalized Root-mean-square error (NRMSE) defined as $NRMSE = \frac{1}{N_s}\sqrt{\sum_{i=1}^{N_s} | M_{xy}^{D} - M_{xy}^{p} |^2}$ with ROI masked between the desired and excited patterns to evaluate the accuracy. All pulse designs and Bloch simulations were performed in MATLAB 2009a (Mathworks, Natick, MA).

4.3.5 Experiments

All experiments were performed on a Siemens 7T whole body scanner (Erlangen, Germany) equipped with an eight-channel PTX system and a gradient set with maximum amplitude of 40 mT/m and maximum slew rate of 170 mT/m/ms. The phantom used for the experimental data acquisition consisted of an 8 cm diameter sphere filled with 1.25 g/liter of nickel sulfate and 5 g/liter of sodium chloride.

For experimental data acquisition, spiral and EP designs with the same parameters as in numerical simulations for acceleration factors of 1, 2, 3 and 4 were compared. RF pulses designed with the nominal and model-corrected gradient waveforms were employed to excite a two-dimensional excitation pattern in the phantom. The desired pattern was a rectangle of 4.5 × 9 cm^2 in the spiral case and a square of 4.5 × 4.5 cm^2 in the EP case, respectively, on a 64 × 64 grid within a FOV of 20 × 20 cm^2. 3D GRE sequence was used with the following parameters: 64 × 64 matrix, FOV= 20 × 20 cm^2, TR =30 ms, TE =2.48 ms, 3.0 mm slice thickness and 300 Hz/pixel bandwidth.

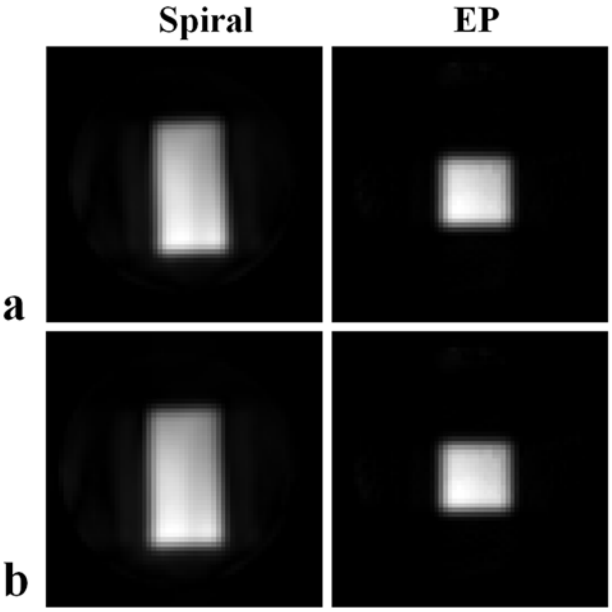

Figure 4.3 Excitation patterns produced by the Siemens birdcage coil using spiral and EP trajectories with an acceleration factor of 2. (a) Excitation obtained with RF pulses designed using the nominal gradient waveforms. (b) Excitation obtained with RF pulses designed using the model-corrected gradient waveforms. Note that no significant differences are observed, which implies that the eddy currents produced on the coil are negligible.

4.3.6 Simulations vs Experiments

We compared RF performance for the spiral and EP trajectory design over a range of acceleration factors for both simulations and experiments. RF pulses were designed with nominal and model-corrected gradients, respectively. Four groups of studies would be implemented as follows,

(a) Ideal Pattern: simulated excitation patterns obtained with RF pulses that were designed based on the nominal gradient.

(b) Simulated Distortion: simulated excitation patterns obtained with RF pulses that were designed based on the model-corrected gradient.

(c) Experimental Distortion: experimental excitation patterns obtained with RF pulses that were designed based on the nominal gradient.

(d) Experimental Compensation: Experimental excitation patterns obtained with RF pulses that were designed based on the model-corrected gradient.

We expected good agreement between simulations and experimental results. Results from (a) and (d) should be close and represent the desired excitation; (b) and (c) should be close and represent the distorted excitation. Significant improvements of excitation accuracy are observed when RF pulses designed by the model-based method are applied.

4.4 RESULTS

4.4.1 Comparison between eight-channel loop coil and TEM coil

Figure 4.3 presents the excitation patterns produced by the unshielded birdcage coil with the spiral and EP trajectories, respectively. The results at the top row were obtained with the uncorrected RF pulses designed using the nominal gradient; while those at the bottom row were obtained with the corrected RF pulses designed using the model-corrected gradients. Clearly, the results are comparable due to the relatively insignificant effects of the eddy currents induced on this coil and also indicate that the eddy currents and delays of gradient system are negligible for our 7T PTX system. By contrast, the TEM coil generates stronger eddy currents due to the RF shield rendering significant eddy current induced errors. Because both gradient waveforms and k-space trajectory are distorted by the eddy current field (Figs. 4.4 a-b), pulses calculated on the actually generated trajectory, which is predicted by the model-based method, are significantly different from the pulses calculated on the nominal trajectory (Fig. 4.4c). Consequently, noticeable changes in the pulse shape lead to the correction of the excitation errors in both spiral (Fig. 4.5) and EP (Fig. 4.6) designs.

4.4.2 Comparison between model-based method and trajectory measurement method

The comparison between the measured and model-corrected gradient waveforms for the spiral design is presented in Fig. 4.5a. From zoom-in figure, we observed that gradient waveforms generated by both methods are very similar, yet considerably different from nominal gradient waveforms. Due to the distortion of nominal gradient waveforms, RF pulses designed by nominal gradient waveforms are inconsistent with the desired excitation pattern. However, both trajectory measurement method and model-based method produced good results. The excitation pattern obtained using the model-based method (Fig. 4.5c) seems to be slightly better than the one obtained using the trajectory measurement method (Fig. 4.5b). So we propose that model-based method can have the comparable performance as trajectory measurement method, but system constants are only needed to be measured one time, rather than re-measure the trajectory whenever trajectory design was modified. Furthermore, model-based method can be performed offline and thus RF pulses can be calculated priori to the experiment, and deployed during the experiment. Time efficiency is greatly improved compared to trajectory measurement method.

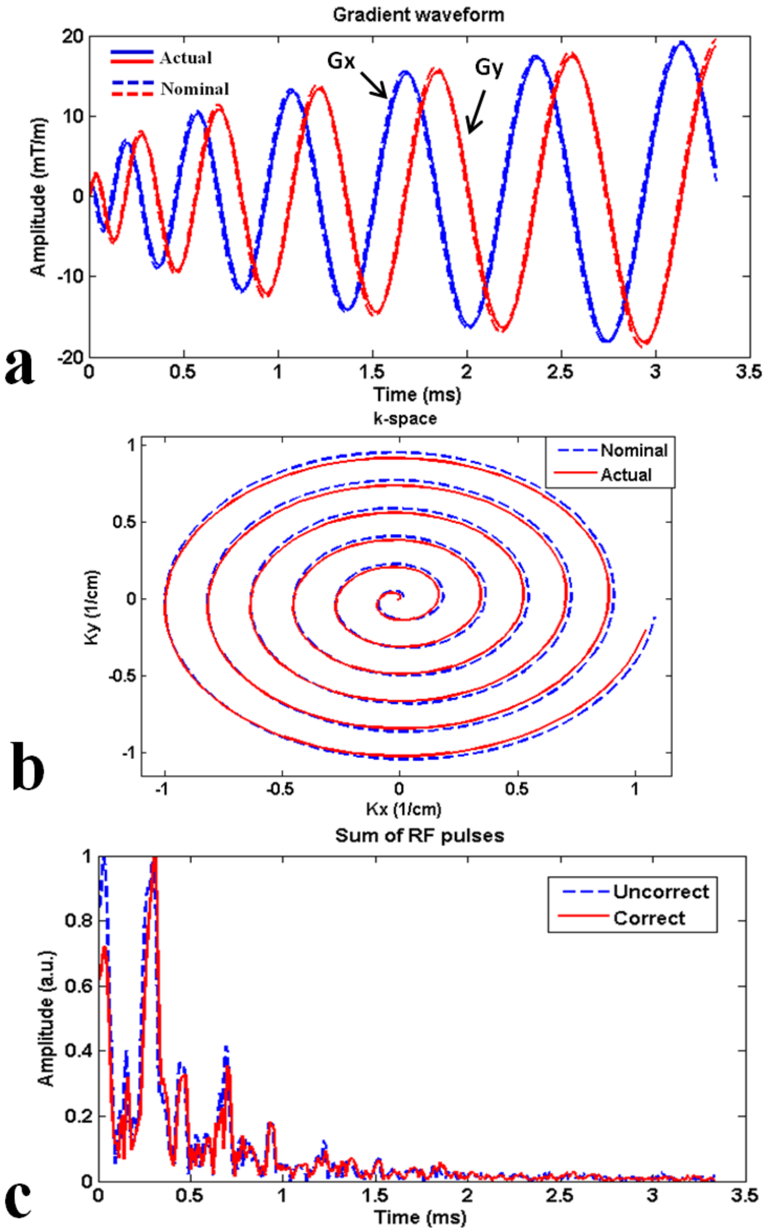

Figure 4.4 Gradient waveforms, k-space trajectory and resulting RF pulses for an acceleration factor of 2 with the use of the TEM coil. (a) Nominal vs actual (model-based correction) gradient waveforms. (b) Corresponding k-space trajectories. (c) Sum of amplitudes of all RF pulses obtained with the nominal (uncorrected) and actual (corrected) trajectories. Note that the deviation between the nominal and actual gradient waveforms leads to significant difference between the uncorrected pulses and corrected pulses.

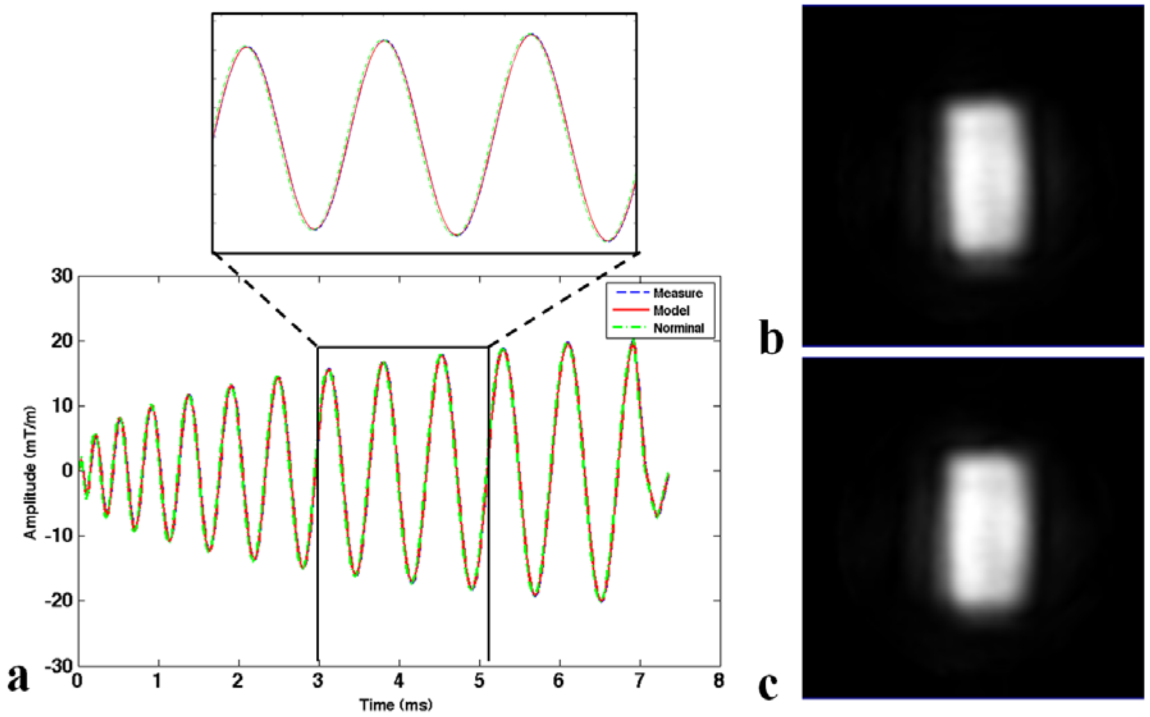

Figure 4.5 Comparison of gradient waveforms and excitation patterns between model-based method and trajectory measurement method. (a) Gradient waveforms obtained from the nominal trajectory, the model-based method and the trajectory measurement method. The zoom-in panel clearly presents that the gradient waveforms derived from the model-based method and the trajectory measurement methods are very close. By contrast, these gradient waveforms are both significantly different from the nominal gradient waveforms. (b) Excitation obtained using the trajectory measurement method. (c) Excitation obtained using the model-based method. Note that model-based method can produce similar or even better results than trajectory measurement method.

4.4.3 Comparison between Simulations and Experiments

Figure 4.6 shows the excitation patterns generated by the uncorrected pulses designed using nominal gradient and the corrected pulses designed using model-based method, respectively, with the spiral design for both simulations (Figs. 4.6a-b) and experiments (Figs. 4.6c-d). Notable tilt of the target pattern and outside artifacts were observed with the excitation of uncorrected RF pulses (Figs. 4.6a and 4.6c). It should be noticed that the distorted rotation primarily comes from the eddy current effects not from the delay between gradients and RF pulses, because it does not appear when we use the unshielded birdcage coil (Fig. 4.2a). The performance of excitation was significantly improved when the uncorrected pulses (Figs. 4.6a and 4.6c) were replaced by the corrected pulses designed via model-based method (Figs. 4.6b and 4.6d). This behavior was consistent over the range of acceleration factors shown in Fig. 4.6. The similar results were observed in the EP design (Fig. 4.7). The results obtained using the corrected pulses designed by the model-corrected method (Figs. 4.7b and 4.7d) provided improvements over those obtained using the uncorrected pulses designed by the nominal waveforms (Figs. 4.7a and 4.7c). Noticeably, there were considerable reductions of the ghosting artifacts along the phase-encoding direction due to the use of corrected pulses. Note that the excitation patterns at R=1 in Figs. 4.7c and 4.7d were contaminated by the long pulse duration (>20ms). This is also one application where parallel transmission can be applied to achieve improved excitation by shortening pulse duration.

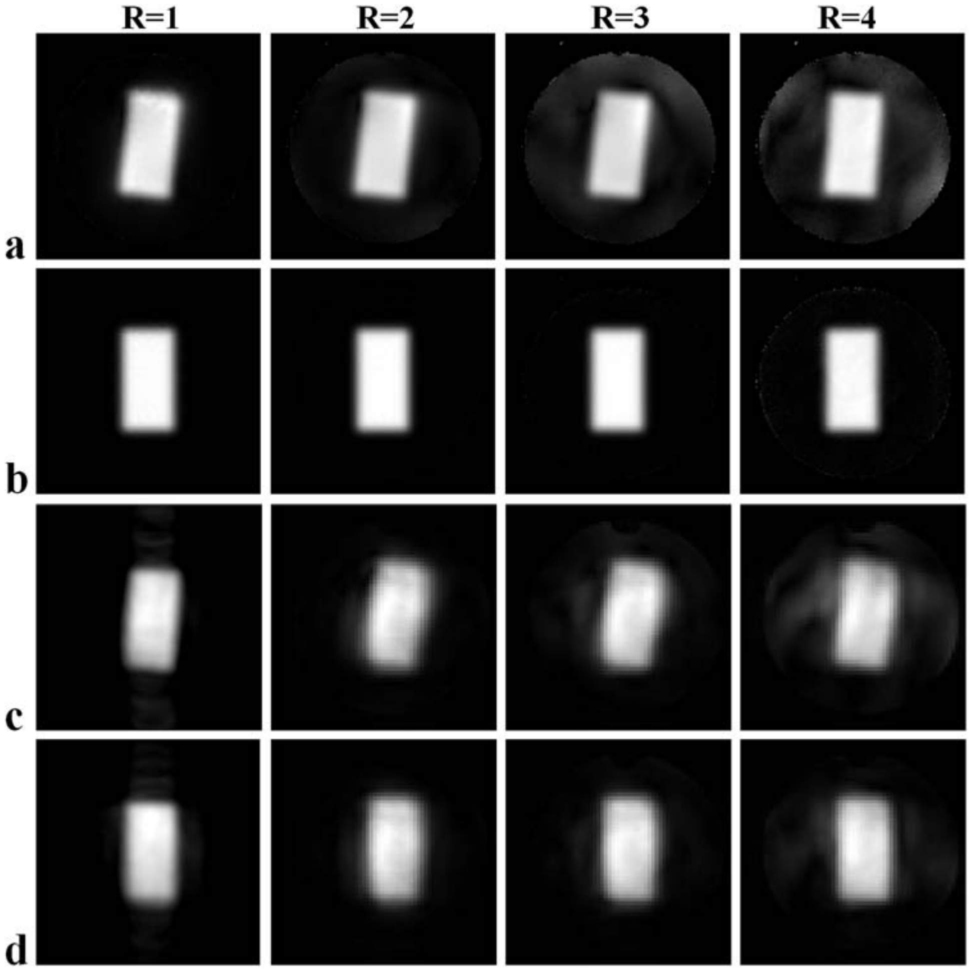

Figure 4.6 Comparison of the RF performance for the spiral trajectory design over a range of acceleration factors for both simulations (a-b) and experiments (c-d). (a) Simulated excitation patterns obtained with the RF pulses designed using the nominal gradient waveforms. (b) Simulated excitation patterns obtained with the RF pulses designed using the model-corrected gradient waveforms. (c) Experimental excitation patterns obtained with the RF pulses designed using the nominal gradient waveforms. (d) Experimental excitation patterns obtained with the RF pulses designed using the model-corrected gradient waveforms. Significant improvements are observed when the model-corrected RF pulses are used for both simulations and experiments.

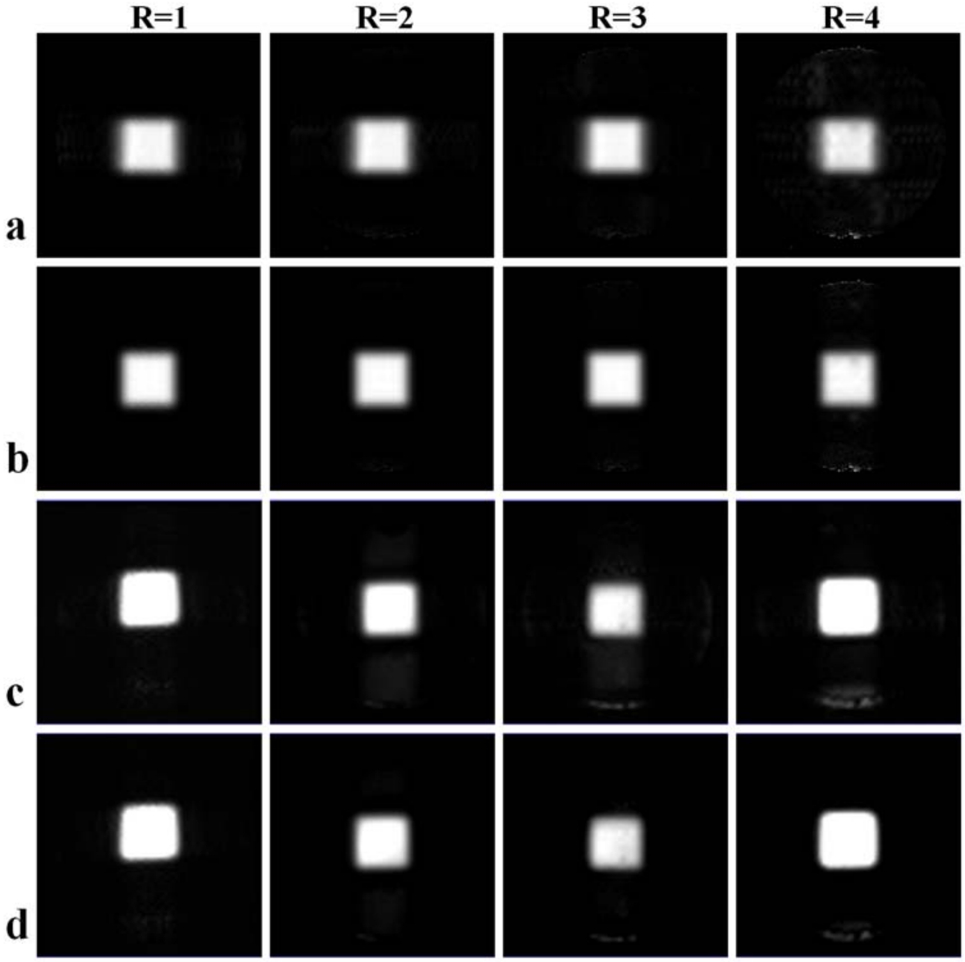

Figure 4.7 Comparison of the RF performance for the EP trajectory over a range of acceleration factors for both simulations (a-b) and experiments (c-d). (a) Simulated excitation patterns obtained with the RF pulses designed using the nominal gradient waveforms. (b) Simulated excitation patterns obtained with the RF pulses designed using the model-corrected gradient waveforms. (c) Experimental excitation patterns obtained with the RF pulses designed using the nominal gradient waveforms. (d) Experimental excitation patterns obtained with the RF pulses designed using the model-corrected gradient waveforms. The result documents the same findings as in Fig. 4.6. Noticeably, significant reductions in ghosting artifacts along the phase encoding direction are obtained through the use of the proposed model-based correction method.

4.4.4 Excitation Quality

In order to evaluate the excitation accuracy, we compared the normalized root-mean-square error (NRMSE) of uncorrected pulses and corrected pulses excited patterns over a range of acceleration factors for both spiral and EP designs (Fig. 4.8). In Fig. 4.8a, it was shown that smaller NRMSE could be achieved with the corrected RF pulses designed by model-based method over the entire range of acceleration factors. Moreover, when the effect of large B_0 field inhomogeneity was excluded, NRMSE could be further reduced for both excitations from uncorrected and corrected pulses. The graph in Fig. 4.8b demonstrated the similar behavior as in Fig. 4.8a. Note that the minimal NRMSE on the blue solid line of uncorrected pulses was not at R=1 but at R=2. However, when we excluded the effect of large field inhomogeneity, it presented that the minimal NRMSE was at R=1. The abnormal phenomenon was caused by the long pulse duration at the EP design (>20ms) as mentioned above, which suffered from the effects of both eddy current field and large field inhomogeneity.

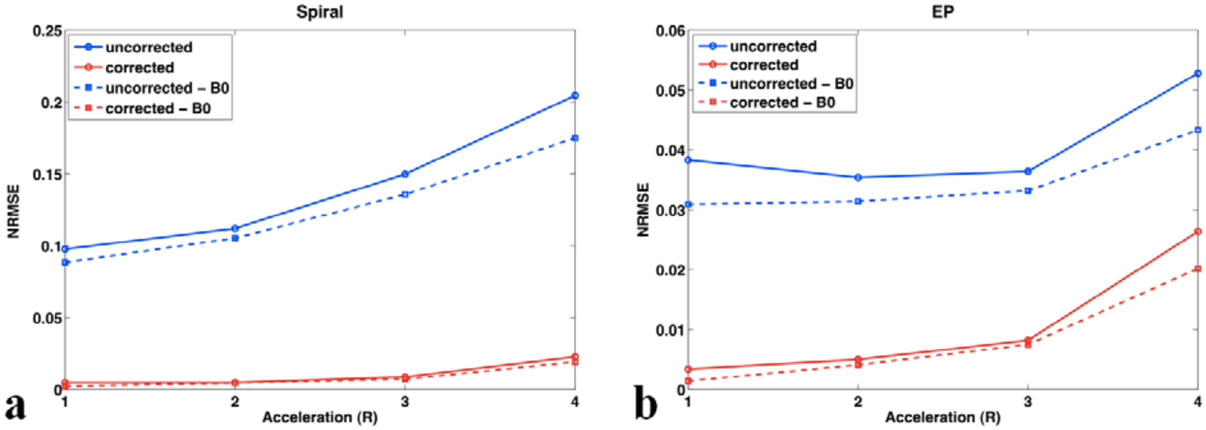

Figure 4.8 Comparison of excitation accuracy for (a) spiral design and (b) EP design over a range of acceleration factors in Bloch simulations. Note that the corrected RF pulses designed by model-based method increase excitation accuracy over the entire range of acceleration factors for both spiral and EP designs. The excitation accuracy is further increased when we exclude the effect of large B_0 field inhomogeneity. However, one interesting finding is that the minimal NRMSE on the solid blue line of uncorrected pulses in (b) is not at R=1 but at R=2. This is most probably due to the long pulse duration at the EP design (>20ms), which suffers from the severe effects of eddy current field and large field inhomogeneity.

4.5 DISCUSSION

To date, various methods have been proposed from hardware and software perspectives to reduce the undesired eddy currents induced by gradient switching. From the hardware perspective, Alecci *et al* (76) found that effective RF shielding and low eddy current sensitivity could be achieved by axial segmentation of a relative thick copper shield, etched on a kapton polymide subtrate. The research for reducing eddy currents with different shielding method is still ongoing in our center. However, our method is helpful not only for the reduction of the eddy currents on the RF shield, but also eddy currents from the gradient system and other delays due to hardware imperfections. While the eddy current effects from our Siemens gradient system are insignificant, other gradient system such as insert gradient system that has much stronger gradient amplitude and slew rate may gain benefits from the model-based procedure as reported here. From the software perspective, we have compared the performance of trajectory measurement method with model-based method. Our proposed method achieves comparable or improved excitation quality. Trajectory measurement method does not lead themselves for practical applications due to the need of re-measuring the trajectory for any new trajectories in order to optimize the generation of a desired excitation pattern. While each trajectory measurement takes about 5-6 minutes, the acquisition time will be significantly increased when many trajectories are needed (e.g., when different accelerations are required) in one PTX session. The method demonstrated here circumvents this problem by using an established model to characterize the effect of the eddy currents on k-space trajectory. The model parameters need only be measured one time for a specific coil and the associated trajectory distortion can be subsequently predicted for any excitation gradient waveforms.

Good agreement is observed between numerical simulations and experimental results for both spiral and EP designs. Note, however, that these numerical simulations are strictly predicting the excitation pattern without the interference of hardware system, assuming homogeneous proton density and ignoring T_1 and T_2 relaxations. Moreover, large field inhomogeneity exacerbates the difficulties in achieving accurate excitation patterns in parallel transmission at 7T (Fig. 4.8). The impacts appears to be severe at R=1 due to the long pulse duration but limited for the relatively short duration of the accelerated RF pulses (Fig. 4.7). Though the B_0 map was incorporated in Eq. (3) for our studies, we have found that it is not adequate to employ the B_0 correction method in Eq. (3) for larger B_0 variation at 7T. To the best of our knowledge, for a given coil and gradient waveforms, the maximum of B_0 compensation will be determined for parallel transmission technique. Therefore, the compensation of B_0 variation tends to be deficient with the use of the reported B_0 correction method in Eq. (3) in the case of large B_0 inhomogeneity and/or long RF pulse duration due to large phase variation accumulation across different spatial locations. This is an interesting and practical topic of parallel transmission that is worthy of further investigations.

Consistent with others' works (40, 79, 84), the proposed method does not consider the effects of cross-terms related to the coupling of the gradient and/or RF coils, which leads to some remnant excitation errors. However, these could be accounted for through extensions of the methodology presented here.

4.6 CONCLUSION

In conclusion, we have successfully demonstrated that the model-based eddy current correction method using parallel transmission RF pulse design is an effective and efficient means to compensate for the excitation errors resulting from eddy currents on the RF shielding at 7T.

5.0 MULTI-SLICE PARALLEL TRANSMISSION THREE-DIMENSIONAL TAILORED RF (PTX 3DTRF) PULSE DESIGN FOR SIGNAL RECOVERY IN ULTRA HIGH FIELD FUNCTIONAL MRI

5.1 INTRODUCTION

Ultra high magnetic field (UHF) MRI has gained considerable interest in recent years due to its improved signal-to-noise ratio (SNR) capabilities and the enhanced contrast mechanisms that it provides (1). Unfortunately, the same mechanisms that lead to enhanced contrast sometimes lead to increased susceptibility artifacts for long-established MRI applications. Functional MRI (fMRI), in particular, is severely affected by both increased physiological noise and susceptibility induced (SI) signal loss at UHF. SI artifacts usually appear as geometric distortions and/or signal loss at some important functional areas of the brain, such as the orbital frontal and inferior temporal cortices (21), and limit the effectiveness of blood oxygen level-dependent (BOLD) fMRI studies of mood and related disorders at fields higher than 3 Tesla (19, 20).

Numbers of approaches have been proposed to recover the susceptibility-induced signal loss, but they all have different drawbacks. One category is focused on optimization between the slice and imaging parameters. Signal loss can be mitigated by the reduction of the size of image voxels (48, 49). Phase cancellation of spin signals can be alleviated via the reduction of voxel dimension of through plane. However, one major drawback of thin slices averaging is, obviously, a reduction in brain coverage per repetition time. Therefore scanning time will be inevitably increased by multiple folds compared to conventional methods. Refs. (50, 51) proposed to use an external coil for localized shimming to recover signal loss. These localized shimming methods were effective to some extent in improving field homogeneity. However, for long time fMRI sessions, placement of shimming hardware on subject leads to significant discomfort, which likely increases head motion and thus critical artifacts are observed. Another class of methods uses z-gradient lobs to compensate for through-plane dephasing, which is dubbed as “z-shim” (52-55). A z-gradient lobe, deployed after excitation, can create linear phase along z dimension that could cancel out the dephasing due to field inhomogeneity accumulated up to data acquisition. Since gradient lobes are non-selective and the extent of dephasing varies as a function of voxel location, one needs to acquire multiple subimages using different gradient moments to refocus different image regions. Then the subimages can be combined to form a final image free of signal loss. To generate an image with acceptable signal recovery, it usually requires several subscans for each slice location, and hence a major problem of z-shim is the temporal resolution loss due to acquisition of multiple subimages for each slice location.

Besides the aforementioned techniques, Stenger *et al* (25) firstly introduced the three-dimensional tailored RF (3DTRF) method to reduce susceptibility artifacts in T_2^* weighted fMRI studies. It has several important advantages. First, it has no interference with imaging parameter, for example, thin slice thickness is not required. Second, it does not require multiple subimage acquisitions for a single image, which is a significant advantage compared to z-shim that sacrifices the temporal resolution. Third, it does not require additional shimming hardware. Finally, this method can be applied in conjunction with many other existing methods, such as thin slice, localized shimming and z-shim for maximal signal recovery. Based on the original version of 3DTRF, Yip *et al* (26) proposed advanced version of the 3DTRF method to effectively improve slice selection fidelity and shorten RF pulse duration, but the pulses are still impractically long (~15ms). Afterward, spectral-spatial RF pulse design (85, 86) for reducing susceptibility-induced signal loss gains more and more interests on benefit of its offline computation. However, it relies on the assumption that resonance frequency offset well predicts through-plane dephasing. This assumption may not be valid at multiple slice locations and different human subjects. Thus, it does not perform well at places where the assumption is violated. Also, the pulse duration is still relatively long (>10ms). Such lengthy RF pulses severely hamper the temporal resolution of the MR images, which is critical in fMRI studies. In addition, because the long 3DTRF pulses are deployed in the regions with highly inhomogeneous field, excitation accuracy can be severely affected by off-resonance excitation. For these reasons, 3DTRF method still needs further investigation for full realization of its potential.

The primary drawback of long pulse duration of the 3DTRF method could be potentially overcome by the promising parallel transmission technology (14-16), which can dramatically shorten RF pulses duration by undersampling the k-space trajectory. Therefore combining the 3DTRF method with parallel transmission would be prerequisite for the clinic use of ultra high field fMRI. Nevertheless, generalization of the 3DTRF method for parallel transmission version is a nontrivial problem due to the complexity of parallel transmission RF pulse design. It consists of two categories: small-tip-angle (16) and large-tip-angle (38, 74) pulse design. In this work we propose the 3DTRF method of small-tip-angle parallel transmission version to recovery the susceptibility-induced signal loss for ultra high field fMRI. This new strategy will be effective over the whole brain coverage for the signal recovery of multi-slice excitation.

This article first introduces basic principles of the advanced version of 3DTRF (26) and small-tip-angle (16) parallel transmission RF pulse design. Afterward, we evaluate the proposed method in a cylinder water phantom and validate the recovery of signal loss at multiple slices. Finally, we demonstrate the signal recovery for *in vivo* studies via applying the designed pulses with Gradient Echo (GRE) and two-dimensional echo planar (EP) BOLD sequences at multiple-slice brain regions on multiple subjects. Results show that the proposed RF pulse design method was successfully improving slice selection fidelity and recovering signal loss at different brain regions of multiple subjects using an eight-channel parallel transmission system at 7T.

5.2 THEORY

5.2.1 Principle of the 3DTRF method

In multi-dimensional excitation, pixel dimension of through plane is often larger than the one of in plane. So through-plane signal loss artifact is of primary importance relative to in-plane dephasing. The goal of the 3DTRF pulse design method is to recover the signal loss via precompensating the through-plane phase variation during the stage of RF pulse excitation. We use the derivations in Ref. 14 to calculate the precompensated phase, which is the negative of the phase variation in the presence of an inhomogeneous main field with frequency offset $\Delta f(x,y,z)$. Assuming slice location z_0 is excited with echo time of T_E, define as the duration between the flip down of magnetization and the center of the k-space acquisition, the through-plane phase variation that dominates the signal loss at in-plane location (x,y) can be modeled with the first order linear relationship as the follows,

$$\phi(x,y,z;z_0) = -2\pi \cdot T_E \cdot [\Delta f(x,y,z) - \overline{\Delta f}(\mathrm{x,y;z_0})] \tag{5.1}$$

where $\overline{\Delta f}(\mathrm{x,y;z_0})$ denotes the mean frequency offset around z_0 along the axial direction and can be defined by,

$$\overline{\Delta f}(\mathrm{x,y;z_0}) = \frac{\int p(z-z_0)\cdot \Delta f(x,y,z)\,dz}{\int p(z-z_0)\,dz} \tag{5.2}$$

where $p(z-z_0)$ is the excited slice profile at the center of slice location z_0. The aim of the aforementioned normalization is to exclude the contribution of in-phase evolution of spin signal for through-plane phase variation. For T_2^* weighted contrast in ultra high field fMRI, the phase variation is very rapid due to the severe main field inhomogeneity. Phase cancellation during readout leads to MR signal loss because the voxel intensities are generated from the integration of spin signals in those regions. Therefore, one way to recover the signal loss is to precompensate the through-plane phase variation in Eq. (5.1) within the excitation profile. We denote $D_{orig}(\mathbf{r},z_0)$ as the original slice-selective excitation pattern with the slice selection peak of $p(z-z_0)$ at z_0. By negating the through-plane phase variation, the precompensated excitation pattern can be formulated as,

$$D_{precom}(\mathbf{r},z_0) = D_{orig}(\mathbf{r},z_0)\cdot p(z-z_0)\cdot \exp(-i\cdot\phi(\mathbf{r},z_0)) \tag{5.3}$$

Then the precompensated excitation pattern $D_{precom}(\mathbf{r},z_0)$ will be the new desired excitation pattern. Ideally, the phase pattern of $D_{precom}(\mathbf{r},z_0)$ would cancel out the through-plane dephasing during T_E, and spins would be aligned in phase when the center of k-space acquired at T_E. This advanced 3DTRF method (26) has been investigated and successfully demonstrated to mitigate signal loss at 3T. However, as aforementioned earlier, the exceedingly long pulse duration significantly hinders its performance in ultra high field (i.e., 7T). Therefore, the parallel transmission technique that can shorten pulse duration without sacrificing the excitation performance is needed for the 3DTRF method to be practical, as addressed in the subsequent section.

5.2.2 Parallel Transmission RF Pulse Design

The most widely used small-tip-angle parallel transmission (PTX) RF pulse design is the spatial domain method proposed by Grissom *et al* (16). In the regime of small-tip-angle excitation (29), the excitation pattern produced by multiple coils of L can be approximated by the integration of Fourier kernel with an excitation k-space trajectory defined as $\boldsymbol{k}(t) = -\gamma \int_t^T G(\tau)\, d\tau$, weighted by RF pulses $B_1\{b_1(t),...,b_L(t)\}$ and spatially dependent transmit sensitivity map (B_1^+ map) $S\{S_1(\mathbf{r}),...,S_L(\mathbf{r})\}$,

$$M(\mathbf{r},T) = i\gamma M_0 \sum_{l=1}^{L} S_l(\mathbf{r}) \int_0^T b_l(t) e^{i2\pi\cdot\Delta f(\mathbf{r})\cdot(t-T)} e^{i\boldsymbol{k}(t)\cdot\mathbf{r}} dt \qquad (5.4)$$

where γ is the gyromagnetic ratio, the equilibrium magnetization is given by M_0 , T is the duration of gradient G and Δf denotes the main field frequency offset. After discretization in space and time dimensions, Eq. (5.4) can be written as a matrix form, $M = \sum_{l=1}^{L} S_l A b_l$ where the encoding matrix A incorporates the Fourier kernel and frequency offset. With this formulation, RF pulses can be designed by solving the following least-square minimization problem,

$$B_1 = \underset{B_1}{argmin}\left\{\| SAB_1 - D \|_W^2 + \beta \| B_1 \|_2^2\right\} \tag{5.5}$$

Here, D is the desired excitation pattern, the optimization is performed over the region of interest (ROI) weighted by the spatial error weighting mask W, and the deposited RF power is controlled by the Tikhonov regularization term $\beta \| B_1 \|_2^2$. Finally, RF pulses can be efficiently solved by Conjugate Gradient (CG) method (19) for the minimization problem.

5.2.3 Multi-slice RF Pulse Design of PTX 3DTRF

The multi-slice RF pulse design for signal recovery is an extension of the previously derived formulation via combining the principle of 3DTRF method with parallel transmission technique. To control the excitation at a set of *N* different slices, we extend the set of equations as Eq. (5.4) to different slices and concatenate the precompensated desired patterns $D_{precom}(\mathbf{r}, z_n) = \{D_{slice1}, ..., D_{sliceN}\}$ in Eq. (5.3) where the slice-selective peak is at the slice location of z_n (n=1,…,*N*), the spatial sensitivity (B_1^+) maps of total slices $S_{total} = \{S_{slice1}, ..., S_{sliceN}\}$ and the aforementioned encoding matrix of total slices $A_{total} = \{A_{slice1}, ..., A_{sliceN}\}$ where frequency offset maps (Δf) are encoded. Finally, we can formulate the following concatenated equation for multi-slice signal recovery,

$$\begin{bmatrix} [D_{slice1}] \\ [D_{slice2}] \\ \vdots \\ [D_{sliceN}] \end{bmatrix}_{z_n} = \begin{bmatrix} [S_{slice1} A_{slice1}] \\ [S_{slice2} A_{slice2}] \\ \vdots \\ [S_{sliceN} A_{sliceN}] \end{bmatrix}_{z_n} \times B_{1,z_n} \tag{5.6}$$

The RF pulses for the signal recovery at the slice location of z_n can be efficiently solved via Conjugate Gradient optimization. Then the RF pulses of signal recovery for other slices can be obtained with the similar procedure above with the location of excited peak (z_n) shifting from slice 1 to slice *N*. In other words, the slice selection profile $p(z-z_n)$ is modified according to the location of the excited peak. Because the concatenated matrix of right side of Eq. (5.6) does not change with the excitation profile, fast parallel computation can be implemented via the use of multiple CPUs, which will be further discussed below.

5.3 METHODS

5.3.1 System equipment

All experiments were performed on a Siemens 7T whole-body Magnetom scanner (Siemens Healthcare Erlangen, Germany) equipped with an 8-channel parallel transmission (PTX) RF system and a gradient set with maximum amplitude of 40mT/m and maximum slew rate of 170 mT/m/ms. An 8-channel transmit/receive volume birdcage head coil was used for all experiments. Phantom experiments were performed on a cylindrical water phantom filled with 1.25 g/liter of nickel sulfate and 5 g/liter of sodium chloride. To mimic the human structure near the tissue and air cavities, we attached a round bottom flask filled with air to the inner top of the water phantom to induce an inhomogeneous field. In the human experiment, five healthy volunteers participated after providing informed consent as approved by the Institutional Review Board (IRB) of the University of Pittsburgh Medical Center and two of them were repeated for the study. In both phantom and human experiments, we performed high-order shimming before all the experiments to achieve the as good shimming as possible for the current experiment.

5.3.2 B_1^+ mapping

One of the most important ingredients for effective parallel transmission pulses design is the rapid and accurate mapping of the B_1^+ maps of the transmit coil array in both experimental phantoms and humans. Multi-slice B_1^+ maps were acquired with a novel fast B_1^+ mapping method firstly introduced by Zhao *et al* (83). This method can efficiently estimate B_1^+ maps for parallel transmission only using the images obtained from one small-tip-angle excitation. Therefore, the totally acquisition for B_1^+ maps was significantly reduced and it only took about 1min 40sec to acquire 21 slices of B_1^+ maps for eight channels. The magnitude and phase of the B_1^+ maps of the central slice for one representative subject are shown in Fig. 5.1.

5.3.3 Main field frequency offset mapping

FLASH sequence with TE_1=3.7 ms and TE_2=4.7 ms, respectively, was used to estimate the frequency offset map in Hertz via dividing the phase difference between the two sets of images by $2\pi(\mathrm{TE}_2\text{-}\mathrm{TE}_1)$. Then the effects of frequency offset have to be incorporated into the RF pulse design as shown in Eq. (5.4). This frequency offset compensation of field maps proved particularly crucial in the context of ultra high field due to its severe field inhomogeneity.

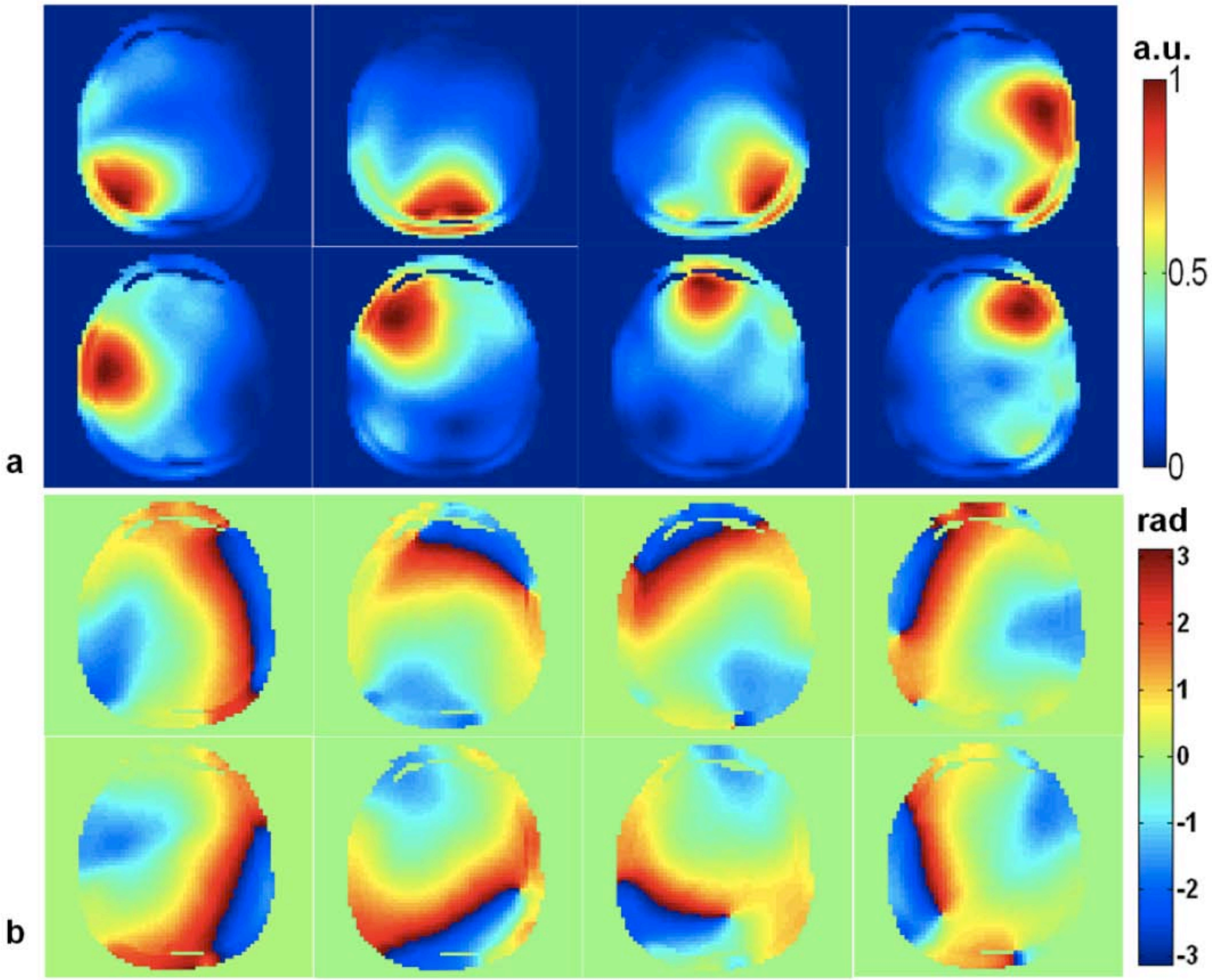

Figure 5.1 Magnitude (a) and phase (b) of B_1^+ map measured at the central slice of one subject for eight-channel parallel transmission.

5.3.4 Pulse design

For multi-slice signal recovery, we precompensated the homogeneous target pattern by the aforementioned dephasing pattern to constitute the new target pattern as explained in Eq. (5.3). To demonstrate the potentiality of the proposed multi-slice signal recovery method, the technique was employed with a flyback fashioned five-spoke fast-kz trajectory (8) centered at the k-space center (Fig. 5.2) to obtain parallel transmission RF pulses that uniformly excite

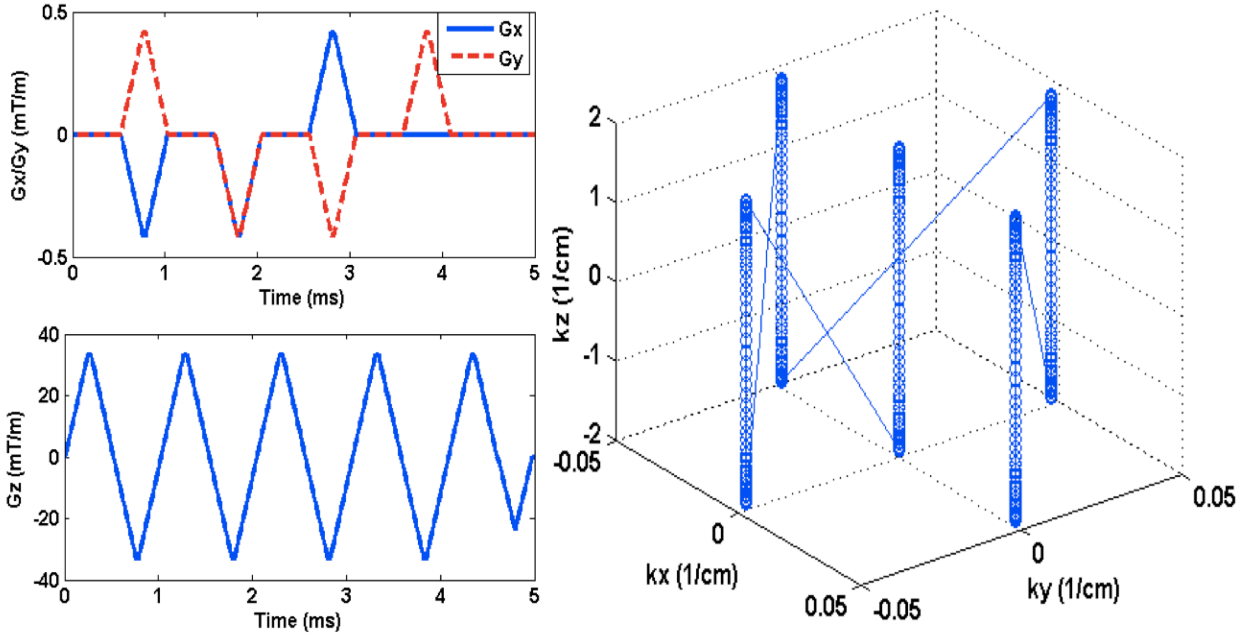

Figure 5.2 Flyback fashioned five-rung fast-kz trajectory.

Gaussian-shaped slice profile with the full width half maximum (FWHM) of 5mm and flip angle=15^o, TE=16ms.

In our pulse design, we have two schemes of PTX 3DTRF method in terms of the gradient dwell time: regular method with gradient dwell time of 10us and time-interpolation method with gradient dwell time of 5us. The trajectory of regular method was complied with the maximum gradient of 18mT/m and the maximum slew rate of 150mT/m/ms, respectively. The resulting pulse duration is approximately 8.5ms. For the time-interpolation method, the maximum gradient and slew rate were constrained with 36mT/m and 150mT/m/ms, respectively. The corresponding pulse length is about 6ms, which is much shorter than the one of the regular method. Therefore the time-interpolation method is more robust to the main field inhomogeneity on benefit of short pulse duration. In other words, even with bad shimming, the time-interpolation method can still produce good results compared to the regular method. This improvement will be demonstrated in the results section. We can also further shorten pulse duration up to around 4ms with the use of non-flyback fast kz trajectory, however, careful calibration has to be done to avoid the ghost artifacts along through-plane direction, which then significantly increases the complexity of experiments.

After determining the B_1^+ maps, fieldmaps, target pattern and trajectory, we design multi-slice signal recovery 3DTRF pulses of parallel transmission version with Conjugate Gradient method implemented with Matlab R2011a (The mathworks, In., Natick, MA, USA) on a Linux PC computing platform running two 2.33GHz quad-core Intel Xeon processors. For regular method, it took about 5min to calculate the RF pulses of 7 slices given the total 21 slices B_1^+ maps and field maps. The computational time of the corresponding time-interpolation method was about 7min due to higher sampling rate.

5.3.5 Phantom experiment

To induce an inhomogeneous field in water phantom, we attached the round bottom flask to mimic the susceptibility-induced artifact in humans. The created inhomogeneous field led to signal loss in GRE images, acquired using SINC pulse under the circular polarization (CP) mode of the RF coil. We subsequently attempted to simultaneously recover the signal loss at different slice locations with the proposed method as described above. The SINC pulses in the GRE sequence was then replaced with the pulses designed by the proposed method while keeping other images parameter the same. We compared the GRE images acquired with SINC pulses and PTX 3DTRF pulses. Furthermore, three-dimensional slice-selective excitation was performed in order to confirm the fidelity of the excited slice volume.

5.3.6 *In vivo* experiment

To illustrate the benefit of the proposed methods, the same protocol as described in phantom experiments would be performed in vivo experiment. GRE images acquired from healthy volunteers were compared to demonstrate the efficiency of the proposed methods. In addition to GRE images acquired with the SINC and PTX 3DTRF pulses, we also acquired EPI images at the same slice locations. Note that for both GRE and EPI sequences, multi-slice RF pulses are deployed in one single scan to simultaneously recover multi-slice signal loss at different slice locations. Moreover, to prove the more robustness of the time-interpolation method than the regular method in the present of field inhomogeneity, we compared the images acquired with two methods in severe and mild main field inhomogeneities, respectively.

5.3.7 BOLD fMRI

Breath holding task is known to produce activations through the whole brain including the regions of susceptibility-induced signal loss. The breath holding task was an initial resting state of 22 seconds followed by the breath holding period of 8 seconds. The set of breath holding and normal breathing was repeated six times. A visual notice of the preparation of holding breath was provided with 3 sec before the start of breath holding period. Subjects were instructed to breathe shallowly during the normal breathing period to be better synchronized with the timing of the breath holding and minimize motion in the scanner. The breathing cycles were monitored and recorded using the scanner’s physiology monitoring system with the respiration belt. Five subjects were recruited to perform the study on a 7T Siemens (Erlangen, Germany) whole body scanner equipped with a PTX extension. In order to prove the reproducibility of the proposed methods, two of the five subjects were scanned twice, respectively. The regular method with gradient dwell time of 10us and time-interpolation method with gradient dwell time of 5us are both implemented. The resulting RF pulse durations are 8.3ms and 6.1ms, respectively. The flyback-fashioned five-rung fast-kz trajectory was employed with the following imaging parameter: TE=16ms, slice thickness=4.5mm and flip angle=20^o.

5.3.8 Effect of trajectory design

We extend multiple slices to whole brain excitation and investigate the effect of trajectory design on signal recovery and computational time. Three different flyback fast-kz trajectories (1 spoke, 3 spokes and 5 spokes) are used to design RF pulses and then investigate the impact of design trajectory. Twenty 5mm thick slices B_1^+ maps and fieldmaps were acquired and then twenty slices RF pulses were designed. Multiple CPUs are employed for fast parallel computation. RF design was implemented in Matlab R2011b on a Mac computing platform running two 2.66GHz six-core Intel Xeon processors. In our design, the computational time for 1 spoke, 3 spokes and 5 spokes trajectories are 3.3mins, 9.2mins and 15.8mins. The resulting RF pulse durations are 1.03ms, 3.47ms and 5.91ms, respectively.

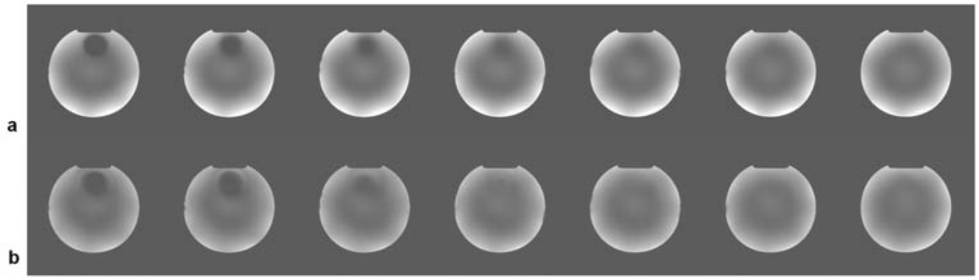

Figure 5.3 Comparison of the performance between SINC and PTX 3DTRF pulses. a: (Top row) excitation patterns obtained with SINC pulses. b: (Bottom row) excitation patterns obtained with PTX 3DTRF pulses. Noticeably, significant signal recovery at multiple slices is observed when the PTX 3DTRF pulses are used.

5.4 RESULTS

5.4.1 Phantom experiment

Figure 5.3 shows the comparison of GRE images of the custom-made water phantom experiments excited by the (a) SINC and (b) PTX 3DTRF pulses. It is clear that susceptibility artifacts induced severe signal loss when the routine SINC pulse is employed. In contrast, with the use of PTX 3DTRF pulses via embedding the precompensated phase pattern, signal recovery could be significantly observed at multiple slice locations while excitation at the other remaining regions are undiminished.

To evaluate the fidelity of excitation profile, we image the slice volume excited by the PTX 3DTRF using 3D imaging sequence. Note that the desired patterns are the multiple slices of homogeneous excitation windowed by the Gaussian profile with the FWHM of 5mm. Figure 5.4 shows the excitation magnitude profile at multiple slice locations along the through-plane direction. One can observe, from the (a) 2D and (b) 1D profiles, excellent slice-selective excitation is illustrated.

5.4.2 *In vivo* experiment

Based on the success of phantom experiments, we can apply our proposed method to in vivo experiment and demonstrate the effective recovery of signal loss on human subjects. Figure 5.5 shows multi-slice fieldmaps acquired from three subjects. It is obvious that frequency offsets are very large at ultra high field (e.g. 7T). Moreover, due to the different loadings of multiple subjects, the susceptibility-induced artifacts on multiple subjects can be significantly different.

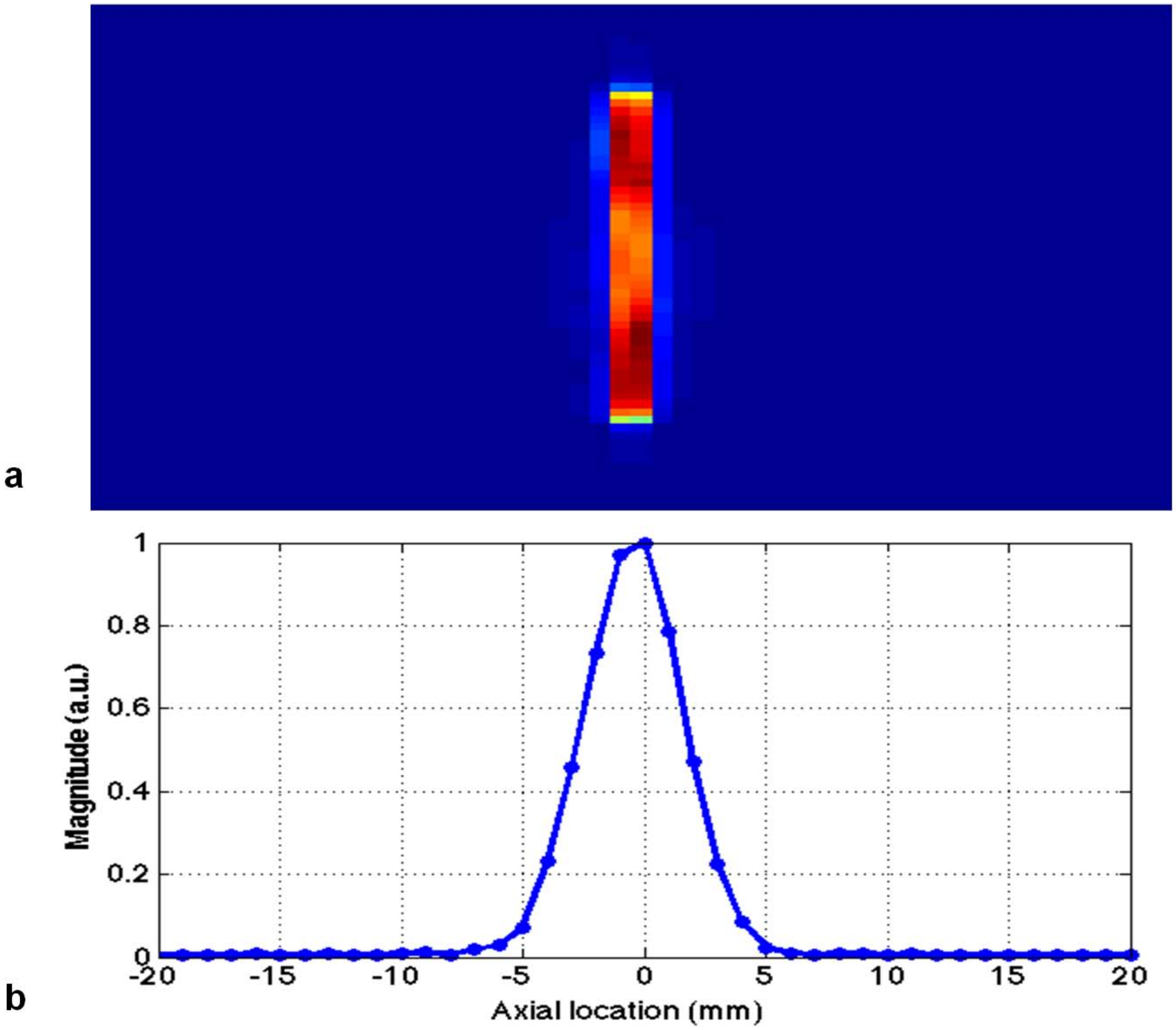

Figure 5.4 2D (a) and 1D (b) through-plane profiles obtained from the excitation patterns using the PTX 3DTRF pulses in Fig. 5.3b.

Note that before performing the experiments, we have done high-order shimming to achieve the best we can have on the current subject. From the results in Fig. 5.6, Subject A exhibits the worst case with severe main field inhomogeneity and signal loss near the regions of the orbital frontal cortex. By comparison, frequency offsets of Subject C are relatively small and subsequently leads to more successful recovery of signal loss.

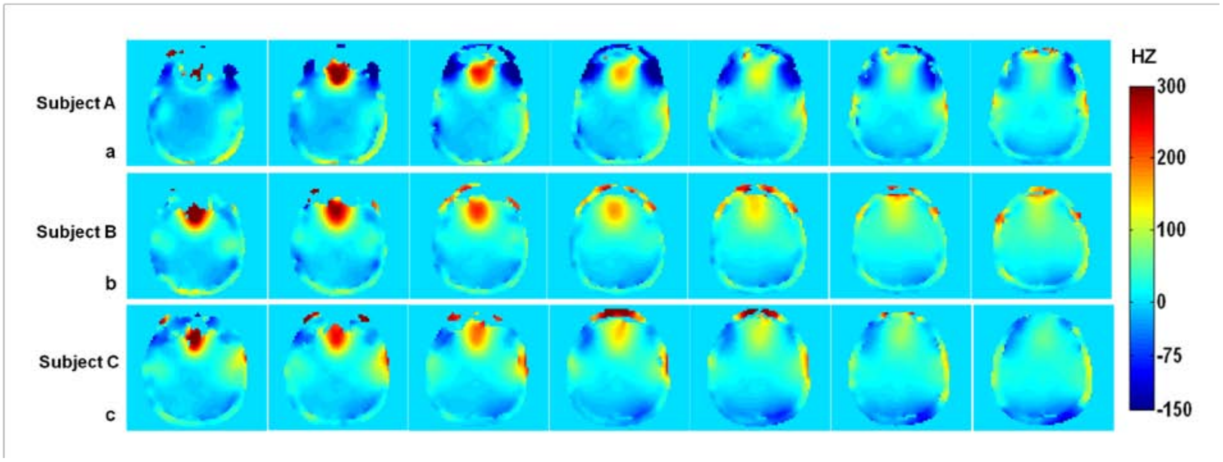

Figure 5.5 Fieldmaps acquired at multiple slices on three healthy subjects. Note that fieldmaps are highly inhomogeneous and frequency offsets are very large in ultra high field. In addition, Subject A shows more severe inhomogeneity than the other two, which leads to the subsequent signal recovery more challenging.

A more in-depth depiction of the distributions of frequency offsets is presented in Fig. 5.6. The mean frequency offsets of Subject A (Fig. 5.6a), Subject B (Fig. 5.6b) and Subject C (Fig. 5.6c) are -19.9 Hz, 16.9 Hz and 13.5 Hz, respectively. And the corresponding standard deviations are 68.7, 46.5 and 42.8, respectively. As observed in Fig 5.6a, another peak close to zero frequency leads to the larger frequency offsets than on Subject C.

Figure 5.7 shows the multi-slice excitation with GRE sequence on Subject A using (a) SINC pulses, (b) regular PTX 3DTRF method and (c) time-interpolation PTX 3DTRF method, respectively. For the excitation of routinely used SINC pulses (Fig. 5.7a), significant signal loss can be observed at multiple slice locations. With the help of PTX 3DTRF(Figs. 5.7b-c), signal loss is simultaneously and precisely recovered at different regions of multiple slice locations. Moreover, the improvement in signal recovery is more evident with the use of time-interpolation method, as indicated by the solid arrows in Figs. 5.7b-c. This also complies with our aforementioned statement that the time-interpolation method, compared to regular method, is more robust and effective at the regions with large frequency offsets.

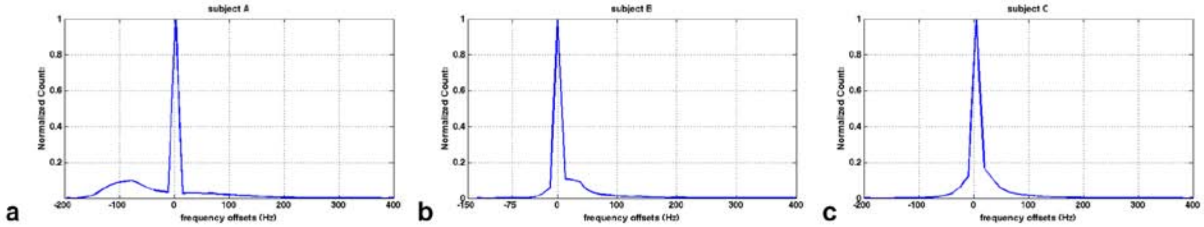

Figure 5.6 The distribution of frequency offsets of the three subjects. The mean and standard deviation of Subject A (a) are -19.9 Hz (SD= 68.7), Subject B (b) are 16. 9 Hz (SD= 46.5), and Subject C (c) are 13.5 Hz (SD= 42.8), respectively. Note that another peak near the main peak in Fig. 5a, results in the large frequency offset on Subject A.

Likewise, the recovery of signal loss can also be noticeably observed on Subject B (Fig. 5.8), where the frequency offsets of fieldmaps are smaller than on Subject A. It is clear that SINC pulses excited GRE images suffered extensive signal loss at different regions. Remarkably, PTX 3DTRF pulses can be effective in recovering signal loss at global regions not only orbital-frontal lobe regions. A more clear view is presented in Fig. 5.9 at the regions where the solid arrows are indicated. Furthermore, even through the frequency offsets are small on Subject C, the improvement of time-interpolation method of PTX 3DTRF is still notable. At the same time, regions that were originally not plagued by the signal loss remained unaffected by the PTX 3DTRF pulses.

Figure 5.10 shows the comparison of multi-slice signal recovery using EPI sequence with three different sets of RF pulses on one representative subject. Visual inspection of multiple slices indicates that both regular and time-interpolation methods of PTX 3DTRF have successfully recovered the signal loss and time-interpolation method proves to be more effective. Similar results are observed at multiple slice locations on other subjects.

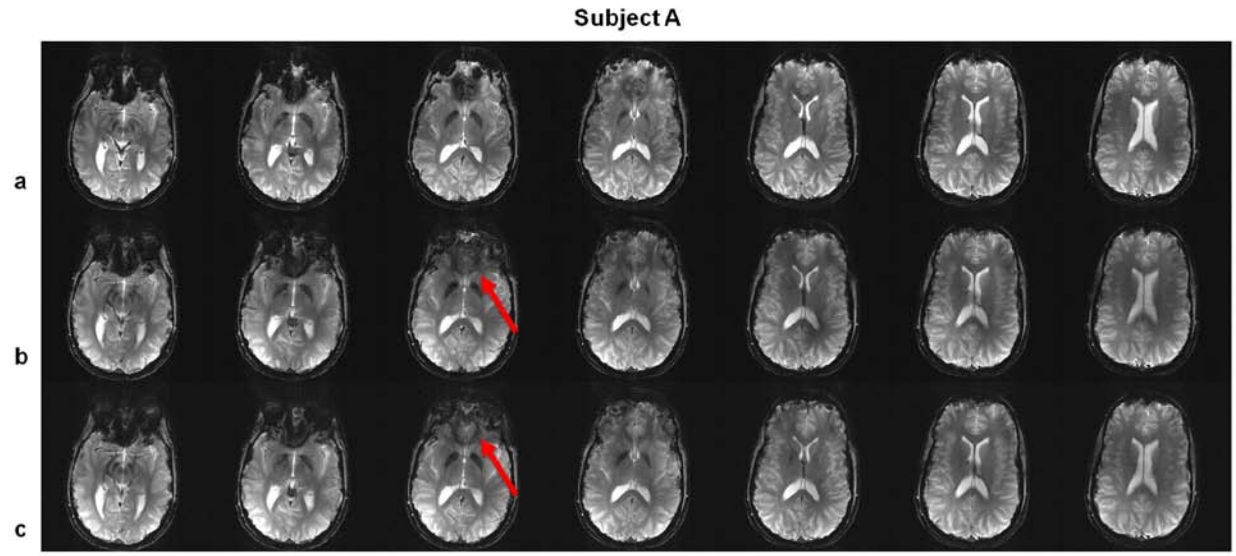

Figure 5.7 Gradient echo (GRE) images acquired on Subject A, using (a) SINC pulses, (b) regular PTX 3DTRF method and (c) time-interpolation PTX 3DTRF method, respectively. Note that the recovery of signal loss can be observed at multiple slice locations. The signal recovery can be further improved using time-interpolation PTX 3DTRF method compared to regular method, as indicated by solid arrows.

5.4.3 BOLD fMRI

Multi-slice BOLD images were acquired using SINC pulses, regular method designed pulses and time-interpolation method designed pulses, respectively. Significant signal loss at multiple slice locations can be observed in Fig. 5.11a. However, signal loss is simultaneously and precisely recovered at different regions across multiple slice locations with the use of PTX 3DTRF(Figs. 5.11b-c). Moreover, the improvement is more evident with the use of time-interpolation method due to the shorter pulse duration. Time-interpolation method is more robust at regions with large frequency offset, which was proved on all subjects. Note that increased activation can be conspicuously noticed within the ROI labeled with blue squares. Figure 5.12 shows the time course of the signal within the marked ROI in Fig. 5.11. It is clear that the two proposed schemes

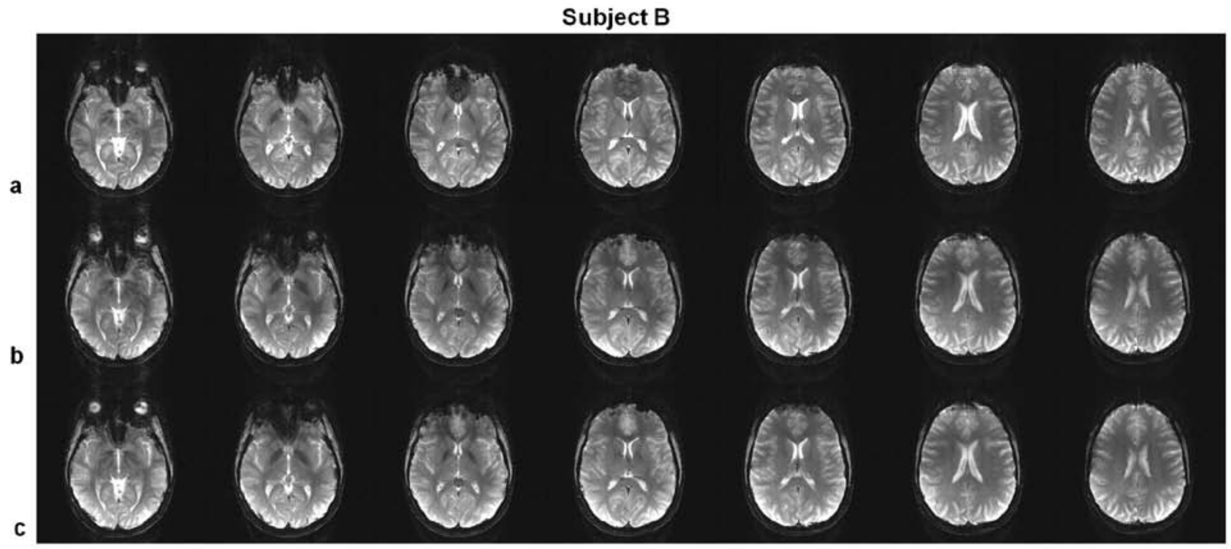

Figure 5.8 Gradient echo (GRE) images acquired on Subject B, using (a) SINC pulses, (b) regular PTX 3DTRF method and (c) time-interpolation PTX 3DTRF method, respectively. On benefit of the smaller frequency offset of the fieldmaps (Fig. 5.5b), the improvement of signal recovery on Subject B is more obvious compared to those in Fig. 5.7.

significantly improve the lost signal and also follow the 30 sec block design of breath holding task. The similar results were obtained when two of the five subjects were scanned twice to prove the reproducibility of PTX 3DTRF.

5.4.4 Effect of trajectory design

Figure 5.13a shows twenty axial slices GRE images excited by PTX 3DTRF with 5 spokes fast-kz trajectory. The comparison of excitations from SINC pulses, 1 spokes, 3 spokes and 5 spokes designed pulses are presented in Fig. 5.13b. Significant signal loss can be observed at one representative slice when the SINC pulses are used. With the help of PTX 3DTRF, signal loss is obviously restored for all three different k-space trajectories. Furthermore, the improvement of

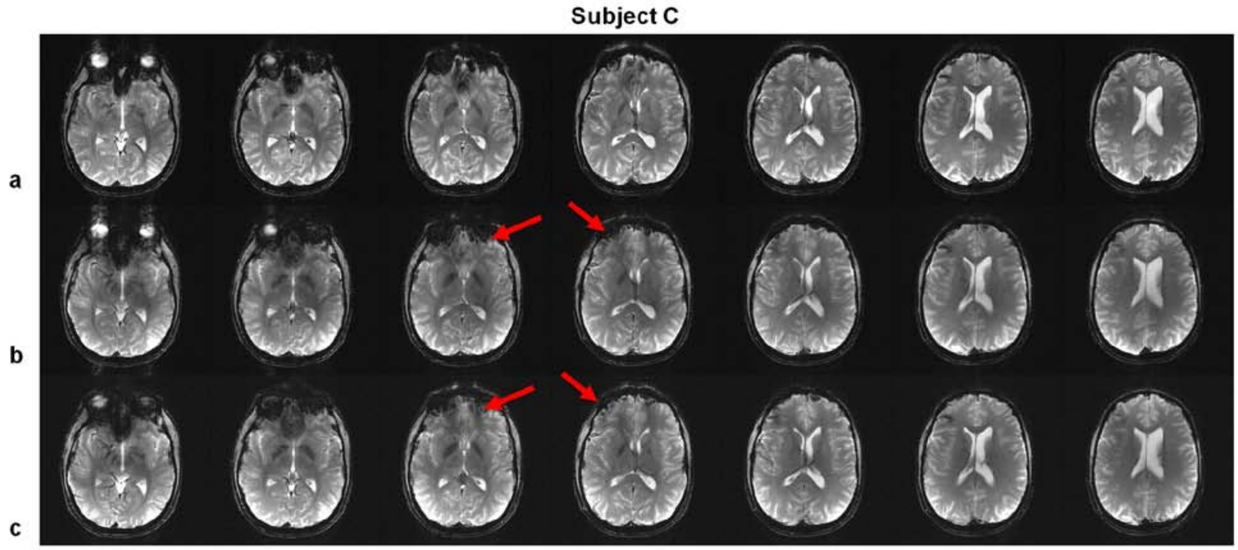

Figure 5.9 Gradient echo (GRE) images acquired on Subject C using (a) SINC pulses, (b) regular PTX 3DTRF method and (c) time-interpolation PTX 3DTRF method, respectively. The result documents the same findings as in Figs. 5.7 and 5.8. Noticeably, not only the orbital-frontal lobe regions but also other regions are beneficial for the use of the PTX 3DTRF pulses. In addition, the improvement of time-interpolation method of PTX 3DTRF is still notable as the solid arrows are indicated.

signal recovery is more evident in 5 spokes fast-kz trajectory design because adding phase-encoding locations can increase the capability to maneuver in-plane excitation variation. However, it is inevitable to increase the pulse duration and computational time. From our experience, the performance would be contaminated at the regions with large frequency offset if the pulse duration is longer than 10ms. The similar results are obtained from EPI BOLD imaging in Fig. 5.14. Visual inspection of increased BOLD activation over the whole brain has demonstrated the effectiveness of the proposed method for the whole brain signal recovery. Figure 5.15 shows the mean signal intensity within ROI labeled with the yellow squares in Fig. 5.13 and Fig. 5.14. As the number of spokes increases, the performance of signal recovery is improved albeit at the expense of increased computational time.

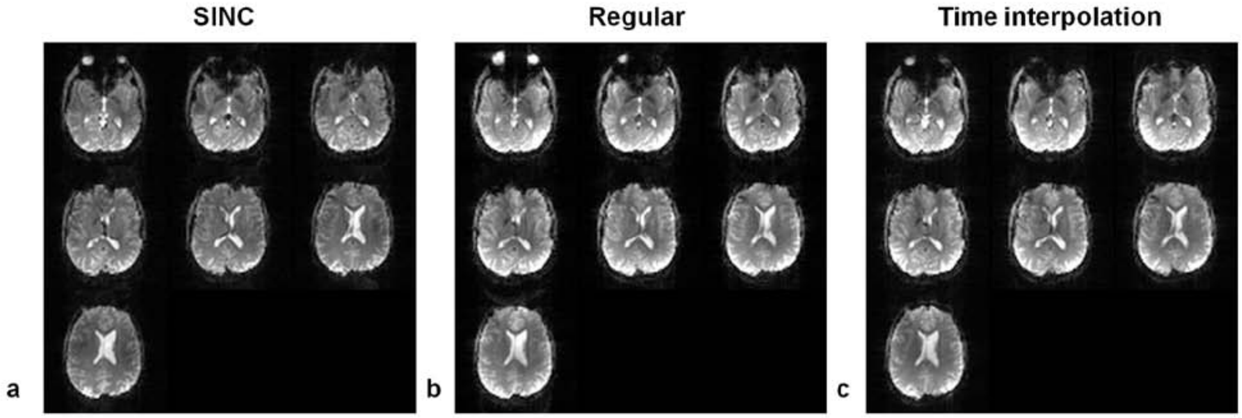

Figure 5.10 Multiple brain slices with EPI sequence using three different sets of RF pulses for the comparison of signal recovery on one representative subject. The signal loss in Fig. 5.10a has been successfully recovered in Figs 5.10b and 5.10c. Similar results are observed in all other subjects.

5.5 DISCUSSION

In this chapter, we have successfully presented a novel excitation strategy to recover the susceptibility-induced signal loss at multiple slice locations and even whole brain via through-plane phase precompensation method combined with parallel transmission technique in ultra high field. This is the first time to demonstrate the 3DTRF method in conjunction with parallel transmission technique can be effective to recover the signal loss in ultra high field. This is also the first time to prove the through-plane phase precompensation method to globally and precisely recover the signal loss of different regions at multiple slice locations and even the whole brain.

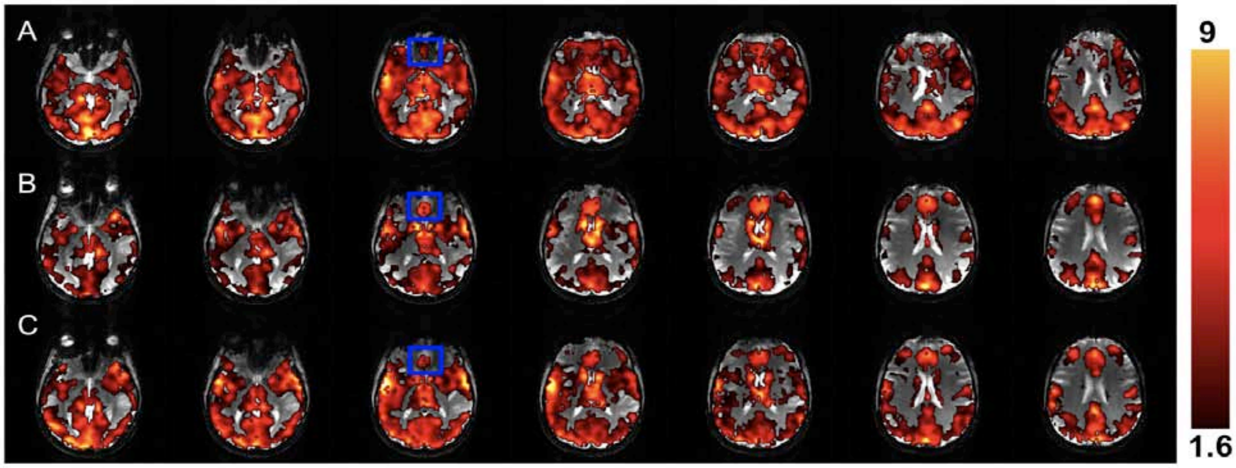

Figure 5.11 Multi-slice BOLD sequence excited using (a) SINC pulses, (b) regular method and (c) time-interpolation method. Note that signal loss (a) within the marked ROI is successfully recovered in (b) and (c). Increased activation is also noticeable.

The PTX 3DTRF method was successfully demonstrated for signal recovery in phantom and *in vivo* experiments. First, we verified that the proposed method was effective in a customized cylindrical water phantom. Afterwards, we illustrated, on all the subjects, that the PTX 3DTRF method was efficacious in slice selection with recovering signal loss at different regions of multiple slices. It is noticed that with PTX 3DTRF pulses, signal loss at multiple locations can be recovered in one single scan due to the incorporation of the accurate priori information (e.g. fieldmap). Simultaneously global and precise multi-slice recovery is one of the major advances relative to the SPSP methods (85). SPSP pulses would devastate the performance of the precompensation concept either bad α choice is made or the fundamental assumption of correlational relationships is violated at different regions.

Another feature of the method presented above is that the pulse duration is significantly reduced compared to any existing method for the recovery of signal loss. Exceedingly long pulse duration has been one of the main obstacles to hinder the practical applications of 3DTRF pulse

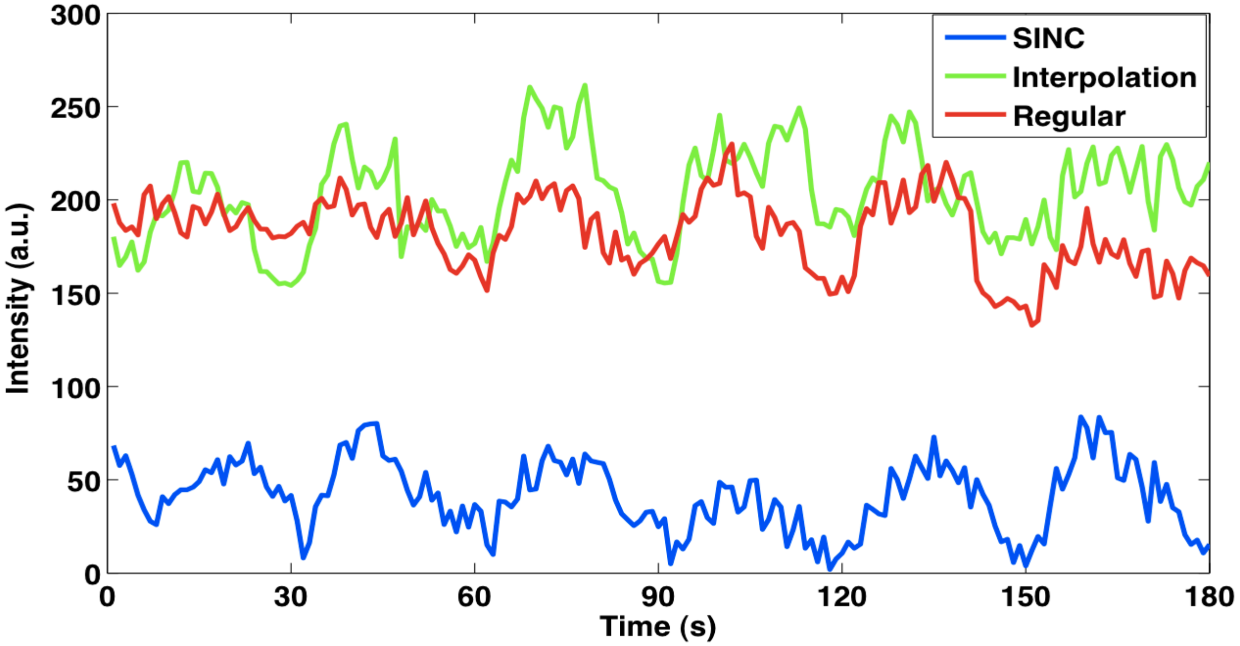

Figure 5.12 Time course of the fMRI signal within the marked ROI in Fig. 5.11.

for more than ten years since the first paper published by Stenger *et al* (25). Afterwards, people were working on reducing the pulse duration from 60ms in the original 3DTRF method (25) to 15ms in the derivative 3DTRF methods (26, 85, 86). In our proposed PTX 3DTRF method, the pulse duration is firstly reduced to 8.5ms using the regular method and 6ms using the time-interpolation method while maintaining the performance of signal recovery and slice selection. This also explains why PTX 3DTRF method is more robust and efficacious for recovering the signal loss at the regions with large frequency offsets.

Though the proposed method is desirable in terms of excitation quality, it is multi-slice RF pulse design and thus computationally complex. As previously mentioned, it took 5min and 7min for the pulse design of the regular method and time-interpolation method, respectively, on our existing computing platform. Albeit at the expense of computational demand for RF pulse design, the PTX 3DTRF does shed light on the routine use of the 3DTRF method with the concept of phase precompensation. It should be pointed out that such computational time does

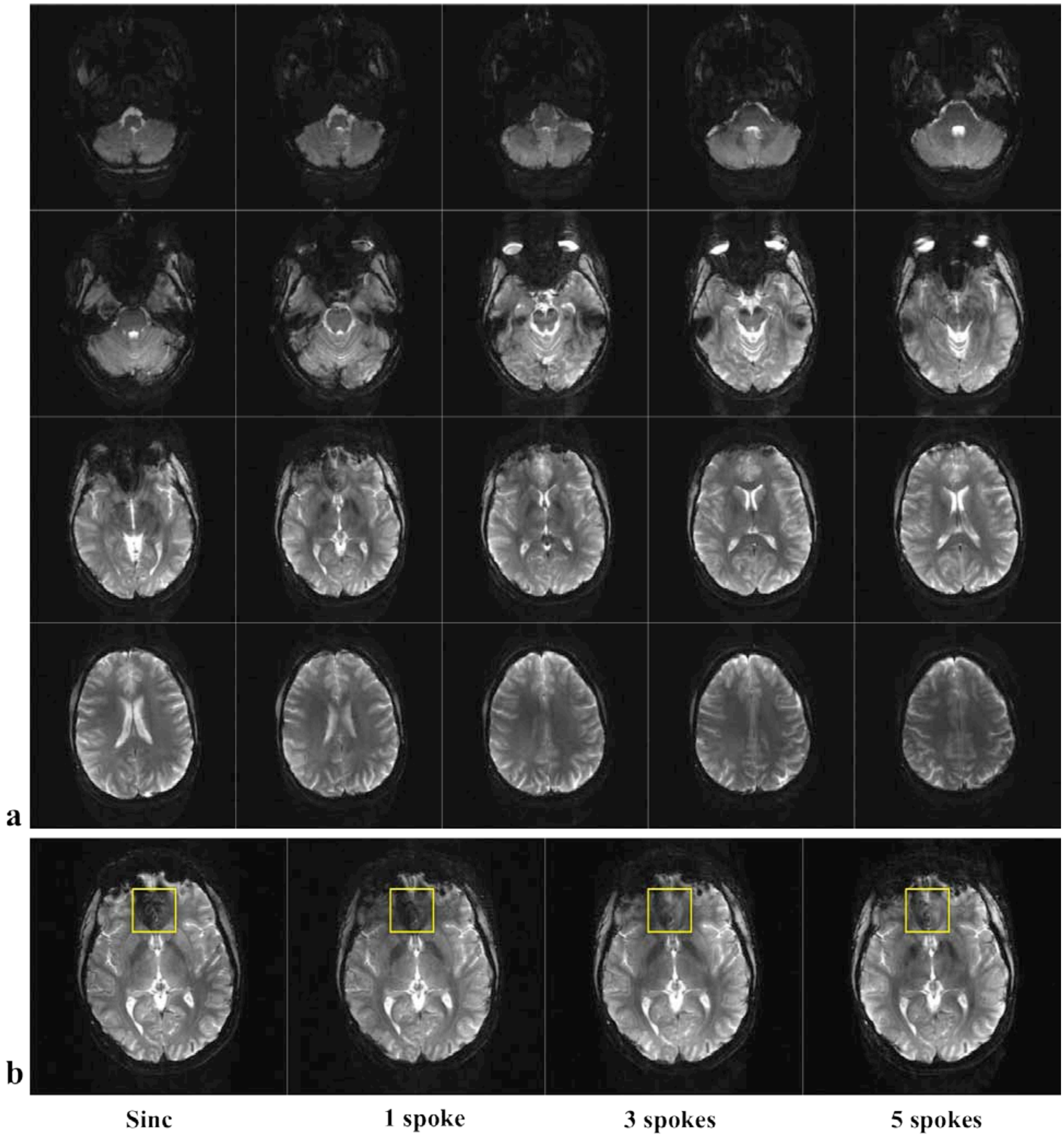

Figure 5.13 (a) GRE images excited by PTX 3DTRF designed using 5 spokes trajectory (b) Comparison of one representative slice excited by different pulses. Note that significant signal recovery was observed within the ROI labeled with yellow squares when PTX 3DTRF was used. Furthermore, the performance of signal recovery was improved with the increase of spoke number.

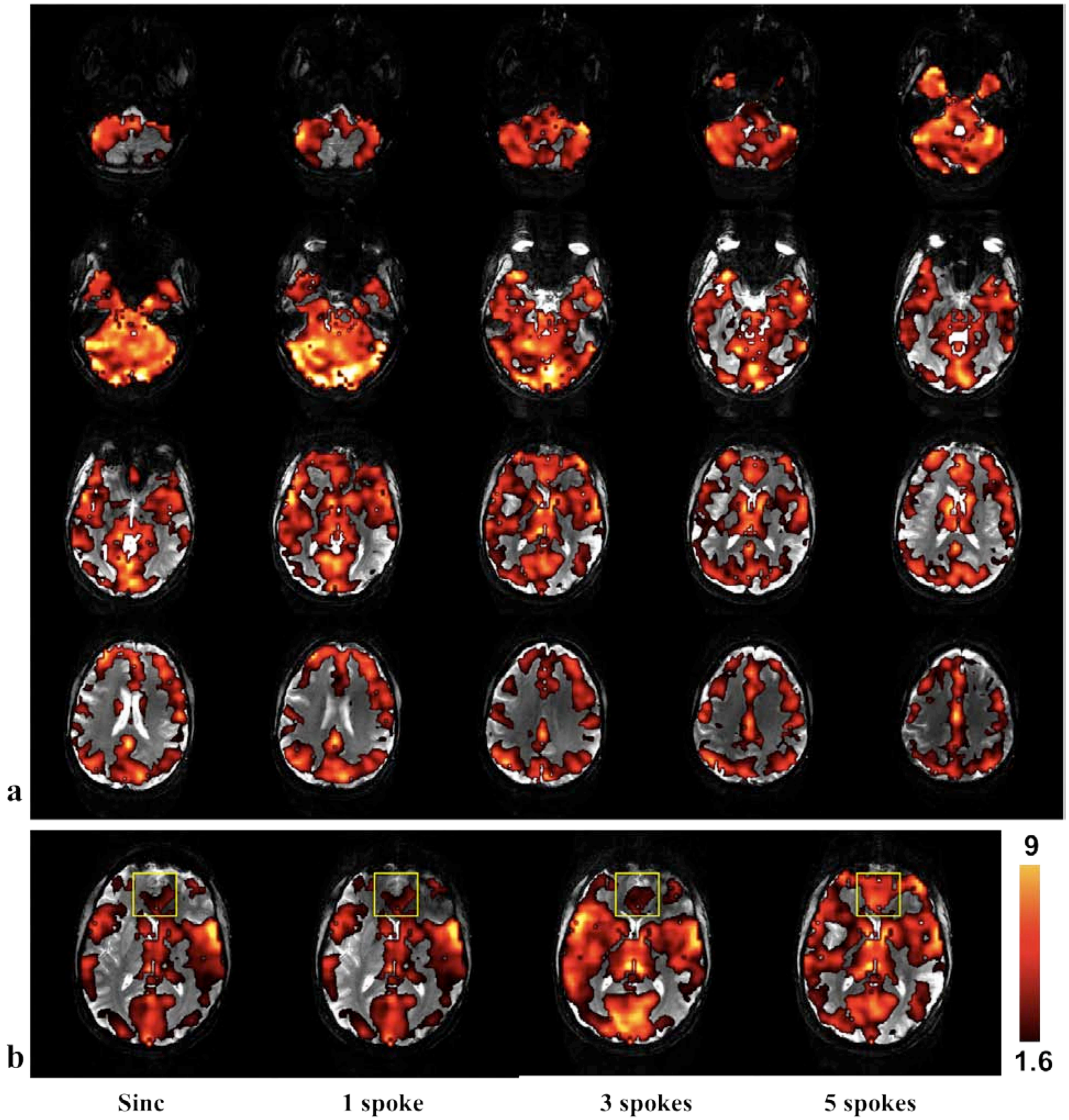

Figure 5.14 (a) BOLD images excited by PTX 3DTRF designed using 5 spokes trajectory (b) Comparison of one representative slice excited by different pulses. Visual inspection of increased BOLD activation over the whole brain has demonstrated the effectiveness of the proposed method for the whole brain signal recovery.

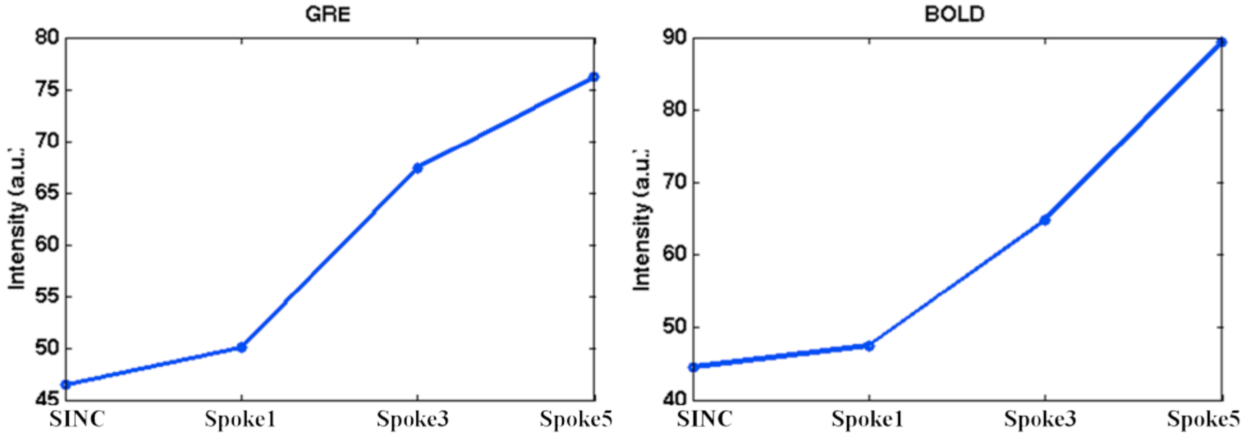

Figure 5.15 Mean signal intensity within the ROI labeled with yellow squares in GRE (Fig. 5.13) and BOLD (Fig. 5.14). As the number of spokes increases, the performance of signal recovery is improved albeit at the expense of increased computational time.

not represent a major practical burden for these techniques as recent reports have shown how the Graphics Processing Units (GPU) found on consumer-grade computational hardware can be used to significantly accelerate the solution of the parallel transmission technique (70, 87).

As Yip *et al* discussed in the advanced 3DTRF method (26), parallel transmission could be the potential strategy to break through the “phase-encoding ceiling”. In this chapter, we present PTX 3DTRF method can enable signal recovery at multiple image regions in the presence of large frequency offsets. Beside the successful signal recovery of multiple slices, we also demonstrate the feasibility of PTX 3DTRF method on BOLD fMRI experiments before introducing the proposed method into routine fMRI use. Further, robustness and reproducibility of PTX 3DTRF pulse design are proved on multiple scans within one subject and multiple subjects. The ongoing breath-holding task is known to produce activations through the whole brain including the regions of susceptibility-induced signal loss. Further investigation will focus on proving the PTX 3DTRF pulses are beneficial for increasing the BOLD contrast and sensitivity to brain activations during fMRI experiments. Future research will also be focused on how to find the optimal compromise between excitation performance and computational time.

5.6 CONCLUSION

With orchestration of all new techniques, parallel transmission and 3D tailored RF pulse design, we have demonstrated an effective means for simultaneous restoring the lost signal over multi-slice and whole brain with relative thin slice selection on both phantom and human subjects. With the proceeds of parallel computation, PTX 3DTRF pulses have high potential for routine use in ultra high field functional MRI.

6.0 PRACTICAL CONSIDERATIONS FOR THE DESIGN OF PARALLEL TRANSMISSION RF PULSES IN ULTRA HIGH FIELD

6.1 INTRODUCTION

Previous chapters have elaborated several issues on RF pulse design for parallel transmission at ultra high field, such as large-tip-angle RF pulse design, eddy current compensation and signal recovery for T_2*-weighted BOLD fMRI. In this chapter, we will focus on some practical considerations for the design of parallel transmission RF pulses especially at ultra high field. Two topics will be introduced: Fast B_1 mapping for parallel transmission application and Compensation for discrete sampling.

6.2 FAST B_1 MAPPING METHOD

6.2.1 Introduction

For a successful parallel transmission experiment, the B_1 map must be known for each transmit channel. So how to rapid and accurate to acquire B_1 map is a nontrivial issue for any parallel transmission application. As the number of the transmit channel increases, the total scan time of B_1 mapping could increase dramatically. Because of this, there is a tremendous motivation to find a fast and accurate B_1 mapping method for parallel transmission applications in the recent years. Many methods have been proposed to measure B_1 map, such as Bloch-Siegert Method (88), Saturated Double Angle Method (SDAM) (89) and Actual Flip-angle Imaging (AFI) (90). However, there are various advantages and disadvantage for parallel transmission at ultra high field (i.e., 7T) with these methods. Note that T_2* decay is very fast at ultra high field, as a result, Bloch-Siegert method could not be used for excitation near the regions of orbital-frontal lobe due to its long RF pulse and thus need for long TE, which leads to significant signal loss in the regions. On the other hand, large-tip-angle pulses could run into SAR limitation, which leads to prolonged scan time for B_1 mapping. To the best of our knowledge, the refocusing pulses and saturation pulses used in these methods could cause this problem. In the chapter, we propose a fast and accurate technique to estimate B_1 map for parallel transmission using only the small-tip-angle images.

6.2.2 Theory

In our past research, we notice that the map of square sum of B_1^+ map and B_1^- map are all quite similar for all our transmit/receive coils (>6 coils, TEM/surface loops). With this observation, we proposed the following procedures to rapidly estimate the B_1^+ map for parallel transmission application using only data from the small-tip-angle experiment. The following assumptions are required for this work,

(1) The sum of square of B_1^+ maps and B_1^- maps, $\mathbf{I_{sq}}$, are equal or very close as shown in Eq. 6.1.

$$I_{sq} = \sum_{i=1}^{N} (B_i^+)^2 \approx \sum_{i=1}^{N} (B_i^-)^2 \tag{6.1}$$

(2) The maps of sum of square of B_1^+ and B_1^- are relatively smooth. So a low pass filter can be used to extract these maps for *in vivo* studies.

Assume that N is the total number of transmit/receive channels for a given coil, i is the used transmit/receive channel. The images of small-tip-angle excitation can be obtained quickly by transmitting each transmit channel sequentially and always receiving with all available receiving channels. The image intensity (**I_i**) from the image acquired by transmitting through only the i_{th} channel is directly proportional to the transmit B_1^+ map, the receiving B_1^- map of the i_{th} channel and proton density **ρ**, as shown in Eq. 6.2.

$$I_i = B_i^+ \sqrt{\sum_{i=1}^{N} (B_i^-)^2 \rho^2} \tag{6.2}$$

Then a summed image **I_{Tot}** can be obtained by simply summing all the images acquired via sequentially exciting each transmit channel as shown in Eq. 6.3, which is a function of image intensity (**I_i**) and proton density **ρ**.

$$I_{Tot} = \sum_{i=1}^{N} I_i^2 = \sum_{i=1}^{N} (B_i^+)^2 \sum_{i=1}^{N} (B_i^-)^2 \rho^2 = I_{sq}^2 \rho^2 \tag{6.3}$$

From the second assumption, we know that the image profile of **I_{sq}** is relative smooth (Fig. 6.1) and thus a low pass filter that can then be applied to filter out the proton density information, which leads to a quick estimate of the map of **I_{sq}** from the measured map of **I_{Tot}**. **R** is defined as the ratio between the image **I_i** of the i_{th} transmit channel and the total summed image **I_{Tot}**. Equation 6.4 shows that B_1^+ map is only related with maps of **R** and **I_{Tot}**.

$$R_i = \sqrt{\frac{I_i^2}{I_{Tot}^2}} = \sqrt{\frac{(B_i^+)^2 \sum_{i=1}^{N} (B_i^-)^2 \rho^2}{\sum_{i=1}^{N} (B_i^+)^2 \sum_{i=1}^{N} (B_i^-)^2 \rho^2}} = \frac{B_i^+}{\sqrt{\sum_{i=1}^{N} (B_i^+)^2}} \tag{6.4}$$

Therefore, the B_1^+ map of the i_{th} channel can be derived from the ratio $\mathbf{R}_i$ and the map of $\mathbf{I_{sq}}$ via Eq. 6.5.

$$B_i^+ = R_i I_{sq} \tag{6.5}$$

6.2.3 Methods

The simulation method used here was very close to previous chapters. A human model was used for simulating *in vivo* B_1 mapping and was used to verify the B_1 estimation algorithm. All *in vivo* experiments were carried out on the 7T Siemens scanner with the multi-transmit capabilities of using an 8-channel transmit/receive coil. The RF waveforms for each transmit channel can be independently driven. The B_1 maps were obtained by sequentially exciting each transmit channel using the 2D GRE sequence with the following parameters: TR/TE = 200/2.51ms, flip angle = 8°, bandwidth per pixel = 1500 Hz/pixel, FOV = 220mm and matrix size = 64×64. The total scan time is only about 1min 40sec. The B_1 map was then estimated using the aforementioned algorithm with acquired data under the regime of small-tip-angle. The interleaves spiral trajectories were numerical designed with a maximal gradient amplitude of 24 mT/m and slew rate of 80mT/m/ms, FOV = 200mm, and matrix size = 32. Two experiments will be implemented to exam the B_1 map estimation algorithm.

(a) Two dimensional slice selective localized excitation with the acceleration factor of 2 in the spiral trajectory.

(b) Three dimensional non-selective uniform excitation with the spoke number of 3 in the fast-kz trajectory.

6.2.4 Results and Discussions

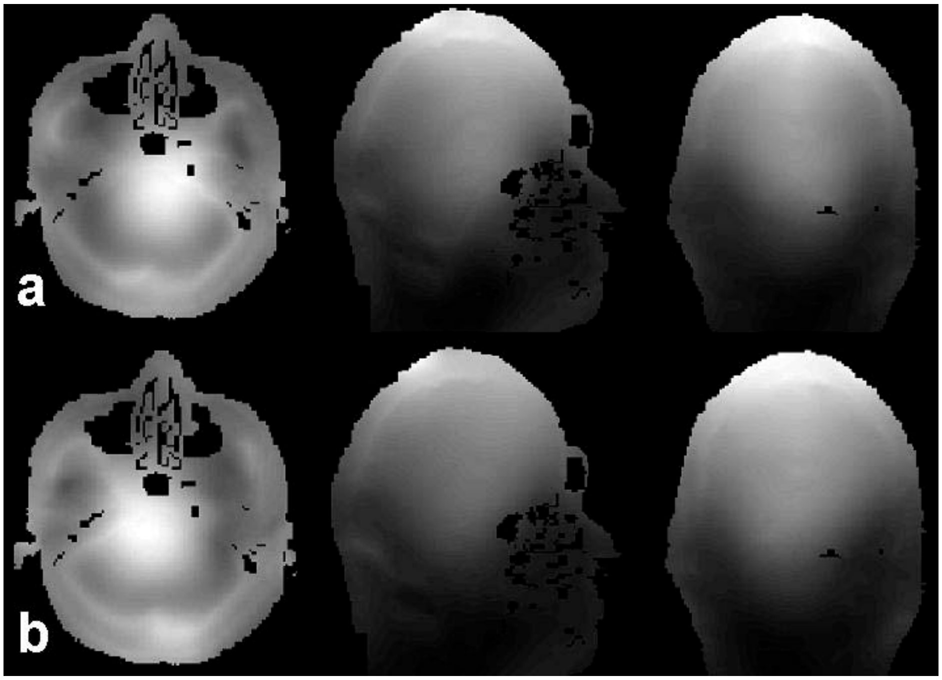

Figure 6.1 (a) The sum of $(B_1^+)^2$ map and (b) The sum of $(B_1^-)^2$ map for the three-plane views from the simulation. Note that they are very close and both relatively smooth.

Figure 6.1 shows maps of the sum of $(B_1^+)^2$ and $(B_1^-)^2$ from a four-channel transmit/receive coil. It is evident that these two groups of three-plane views demonstrated very clear similarities, which validated our assumption as shown Eq. 6.1. The behavior was observed with all our transmit/receive coils (>6 different coils). With homemade simulation program, we can also simulate the experiment of small-tip-angle excitation. The simulated data were then seeded to the proposed B_1 mapping technique to produce the estimated B_1 map.

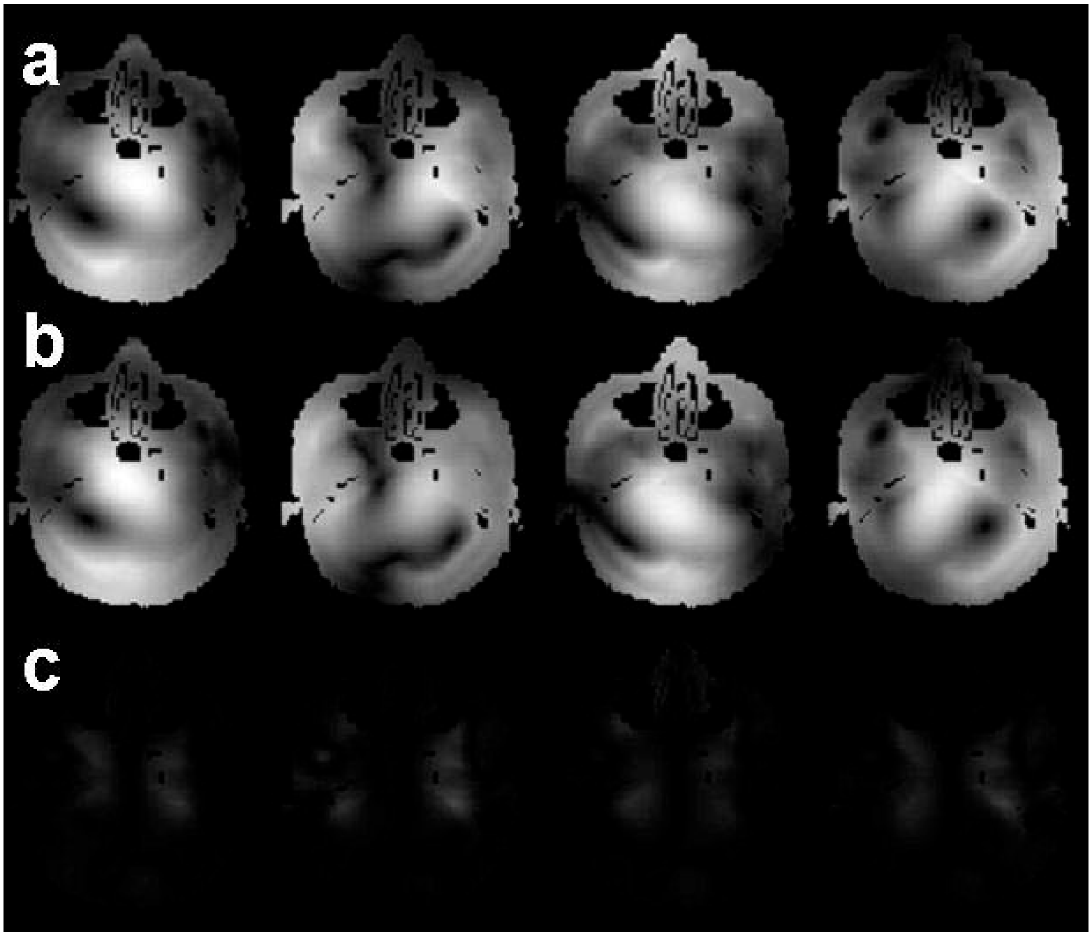

Figure 6.2 (a) The B_1^+ map acquired by multiple-angle method and (b) The estimated B_1^+ maps acquired by the proposed method, and (c) the difference between (a) and (b).

Figure 6.2a (top row) shows the B_1^+ map acquired by multiple-angle method (64), which is accurate but quite time-consuming. Figure 6.2b (middle row) shows estimated B_1^+ map acquired by the proposed method, which is accurate enough but very fast. Figure 6.2c (bottom row) shows the difference between the two groups of maps. These data demonstrated that the proposed B_1 mapping method produced a reasonable accurate B_1 maps with only some minor discrepancies, but is much faster than any existing method.

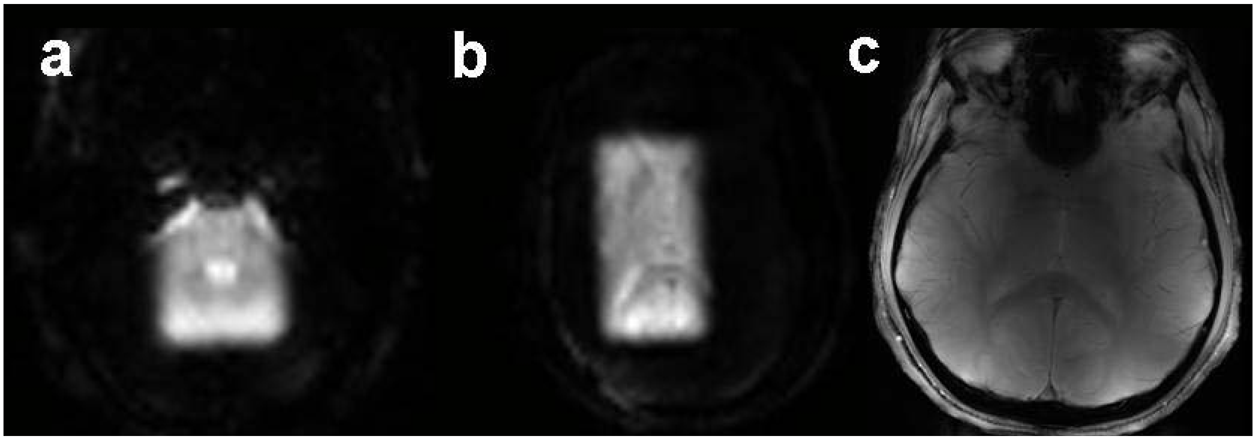

Figure 6.3 In vivo studies using the estimated B_1 maps acquired by proposed method. (a) 2D selective localized excitation for subject 1, (b) 2D selective localized excitation for subject 2, and (3) 3D nonselective uniform excitation with 3-spoke trajectory.

Interestingly, we noticed that the distribution of the difference seems to be similar for all four transmit channels, which partially indicated that there were some discrepancies between the sum of $(B_1^+)^2$ map and the sum of $(B_1^-)^2$ map. However, as the number of transmit channels increases, the discrepancies between the sum of $(B_1^+)^2$ map and the sum of $(B_1^-)^2$ map become trivial. Thus, the estimated B_1 maps from the proposed mapping method are expected to be more accurate with more transmit channels.

To demonstrate the application of the proposed B_1 mapping method, two healthy subjects were recruited and the B_1 maps were estimated using the proposed method for an 8-channel transmit/receive coil with 8 loops evenly distributed on the surface of the cylindrical. The 2D selective localized excitations with the desired rectangle pattern were shown in Figs. 6.3a-b for the two subjects. The RF pulses were designed using aforementioned small-tip-angle parallel transmission RF pulse design method with the acceleration factor of 2 in spiral trajectory. In addition, 3D non-selective RF pulses with the spoke number of 3 in the fast-kz trajectory were designed for uniform excitation, as shown in Fig. 6.3c. The intensity variation was caused by the receiving profiles. A uniform image was obtained by removing this receiving profile. The *in vivo* data shows satisfied results with the proposed B_1 mapping method. The presented parallel transmission results show similar quality as those with other B_1 mapping methods, which also assure that the proposed method is accurate enough for practical applications. Last but now least, it is worthy of note that with the proposed B_1 mapping method, the total scan time for obtaining the B_1 maps of the whole brain for an 8-channel transmit/receive coil is only 1min 42sec and the SAR is very low.

6.2.5 Conclusion

To conclude, we have successfully proposed a fast B_1 mapping method in parallel transmission at ultra high field. The proposed method is fast and accurate to estimate B_1 maps for parallel transmission applications. In addition, only the images acquired from small-tip-angle are required by this method, which greatly reduces the acquisition time and overcomes the limitation of SAR issue.

6.3 COMPENSATION FOR DISCRETE SAMPLING

6.3.1 Introduction

From previous chapters, parallel transmission has been demonstrated as a promising means to accelerate multidimensional selective excitation using multiple coils driven with independent waveforms. Accelerated selective excitation can also reduce specific absorption rate (SAR) and shorten multidimensional RF pulses in such applications as compensation for B_1 and B_0 inhomogeneities. Therefore, parallel transmission could be a potential solution for mitigating or solving RF and SAR problems at the ultra high field (e.g, 7T). Many methods have been proposed for designing the RF pulses for multiple coils (14-16). One of the popular methods was proposed by Grissom *et al* (16), which formulated RF pulse design as a quadratic optimization problem in the spatial domain and allowed the use of arbitrary k-space trajectories and the incorporation of B_0 inhomogeneity correction. We applied this method for 7T applications and found that excitation artifacts were generated due to discrete sampling, which is caused by finite gradient raster time. This fact is generally neglected during the implementation of Grissom's method. In this study, two novel methods were proposed to compensate the aforementioned excitation errors and verified using Bloch simulations and phantom experiments on 7T scanner.

6.3.2 Methods

Under the regime of small tip angle, the transverse magnetization produced by RF pulse waveforms $\sum_{n=1}^{N} b_n(\mathbf{r})$ from N transmit coils can be approximated by the Fourier integral of an excitation k-space trajectory using the coil's complex B_1 map $\sum_{n=1}^{N} S_n(\mathbf{r})$,

$$M(\mathbf{r},T) = i\gamma M_0 \sum_{n=1}^{N} S_n(\mathbf{r}) \int_0^T b_n(t) e^{i\mathbf{k}(t)\cdot\mathbf{r}} dt \tag{6.6}$$

where γ is the gyromagnetic ratio, M_0 is the equilibrium magnetization magnitude, T is the pulse length, and k(t) is defined as the time-reversed integration of the gradient waveforms. As shown in Ref. (16), by directly discretizing time to N_t samples and space to N_s samples, we may write:

$$M = \sum_{n=1}^{N} D_n A b_n \tag{6.7}$$

where M_0 is the length of N_s vector of spatial samples of excitation pattern, $D_n = diag\{S_n(\mathbf{r})\}$ is a diagonal matrix containing the sensitivity maps of coils. The (i, j)$_{\text{th}}$ element a_{ij} of the matrix A with size of $N_s \times N_t$ is given by,

$$a_{ij} = i\gamma M_0 \Delta t e^{i\mathbf{r}_i \bullet k(t_j)} \tag{6.8}$$

On Siemens 7T scanner, the gradient raster time Δt is 10us, which is used as the time step for designing both the spiral trajectory and RF pulses for parallel transmission. However, as shown in the following simulation and experimental results, this method of directly discrete sampling is not accurate enough due to finite gradient raster time step. To improve to the accuracy, we assumed that the gradient during each Δt period is constant, which leads to a linear $k(t)$ as,

$$k(t-t_i)=k(t_i)+\frac{k(t_{i+1})-k(t_i)}{\Delta t}(t-t_i) \tag{6.9}$$

Since the minimal time step for RF waveforms is 1us, the RF waveforms within Δt can be specified either as a constant or a linear function with the use of more RF sampling data points. Therefore, the correct a_{ij} can be obtained by the integration of each Δt period instead of direct discretization as shown in Ref. (16).

6.3.2.1 Method I (Constant function)

Assume that RF pulses $\sum_{n=1}^{N} b_n(\mathbf{r})$ is constant within each small Δt period, the (i, j)$_{\text{th}}$ element of matrix A is giving by,

$$a_{ij}=i\gamma M_0 \Delta t e^{i\mathbf{r}_i \bullet k(t_j)}\times(\frac{e^{c_{ij}}-1}{c_{ij}}) \tag{6.10}$$

where the correction coefficient c_{ij} is giving by,

$$c_{ij}=i\mathbf{r}_i\bullet\{k(t_{j+1})-k(t_j)\} \tag{6.11}$$

6.3.2.2 Method II (Linear function)

Assume RF pulses $\sum_{n=1}^{N} b_n(\mathbf{r})$ is linear within each small Δt period, the (i, j)$_{\text{th}}$ elment of matrix A is giving by,

$$a_{ij}=i\gamma M_0 \Delta t[e^{i\mathbf{r}_i \bullet k(t_j)}\times(\frac{e^{c_{ij}}-c_{ij}-1}{c_{ij}})+e^{i\mathbf{r}_i \bullet k(t_{j-1})}\times(\frac{c_{ij-1}e^{c_{ij-1}}-e^{c_{ij-1}}+1}{c_{ij-1}})] \tag{6.12}$$

where the correction coefficient c_{ij} is the same as in Eq. (6.11)

6.3.3 Results and Discussions

All experiments were performed on 7T Siemens scanner equipped with the multi-transmit capabilities. An 8-channel transmit/receive coil in Fig. 6.4 was used and the RF waveforms for each transmit channel can be independently driven. The B_1 map with resolution of 64 by 64 for each transmit channel was obtained using aforementioned fast B_1 mapping method. The interleaves spiral trajectories were numerical designed with a maximal gradient amplitude of 24mT/m, slew rate of 80mT/m/ms, FOV = 200mm. The acceleration factor for the RF excitation was from 2 to 4, which depends on the number of spiral/EPI interleaves. The design flip angle was 5° and total RF duration was 5.4 ms.

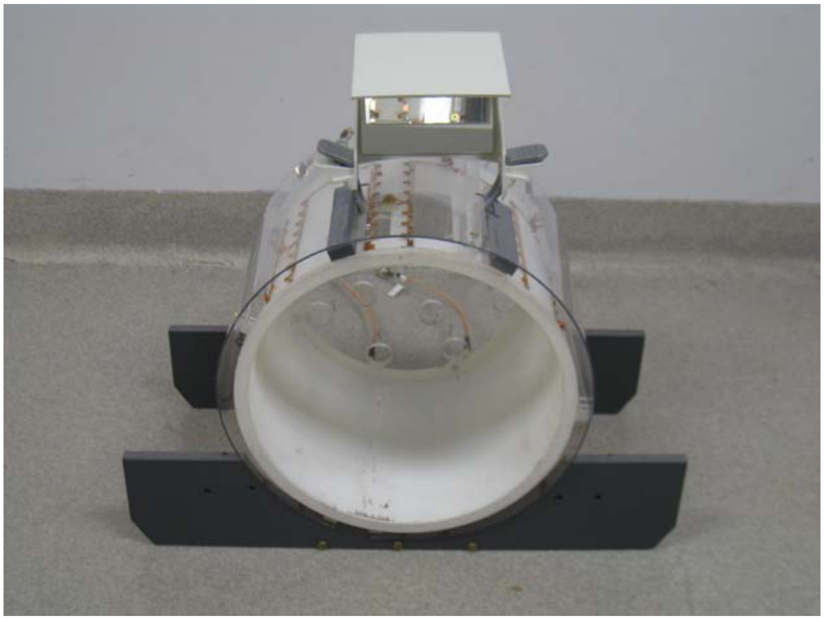

Figure 6.4 The 8-channel transmit/receive coil used in the experiments.

Figure 6.5 shows the comparison of excitation patterns using different RF pulse design methods with acceleration factor of 4. Top row in Figure 6.5 shows the Bloch simulation results and bottom row in Figure 6.5 shows the experimental results. It is obvious that the both Bloch simulation and experiments indicated the excitation pattern designed by the method described in

Ref.16 was slightly tilted to the left and achieved higher residue excitation errors at the background. On the other hand, both Method I and Method II corrected these excitation errors in the simulations and experiments. Figure 6.6 showed the experimental excitation profiles taken along the red dotted line in Fig. 6.5. The excitation profile using the method with directly discrete sampling as in Eq. 6.8 showed a slightly shifted excitation profile. However, both Method I and Method II successfully compensated the errors caused by discrete sampling. To quantify the excitation errors, the mean square errors for the experimental excitation patterns in relative to the designed pattern were determined to be 0.069, 0.0015, and 0.0010 for regular method with directly discrete sampling, Method I and Method II, respectively. The methods described in this study reduced excitation error by more than six times in terms of mean square errors.

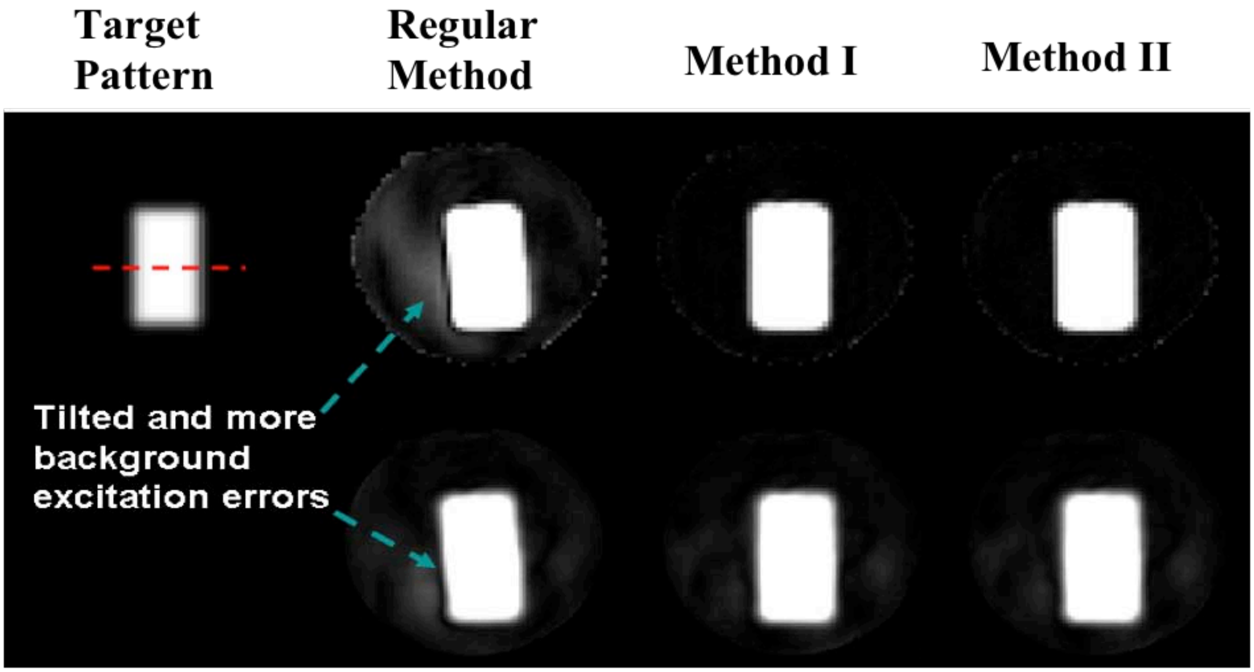

Figure 6.5 Comparisons of different RF pulse design methods. Top row: Bloch simulation; Bottom row: phantom experiments.

Although the issue of tilt was corrected and background errors were smaller using the proposed methods in experiments as shown in Fig 6.5 (bottom row), the mean square error reduction factor are only about two, which is much smaller than the ones in the simulation results, especial at the background region. We speculated that the excitation errors in the experiments caused by many other factors, such as eddy currents and delays between the RF pulses and gradients. The excitation with other acceleration factors for EP trajectory were also implemented and the proposed methods provided better results for both trajectories. When the EP trajectory was used, the excitation without using the correction terms showed obvious ghosting instead of tilt as shown in Fig. 6.5. On the other hand, the experimental results with the use of EP trajectory also showed more obvious background errors than the simulated results.

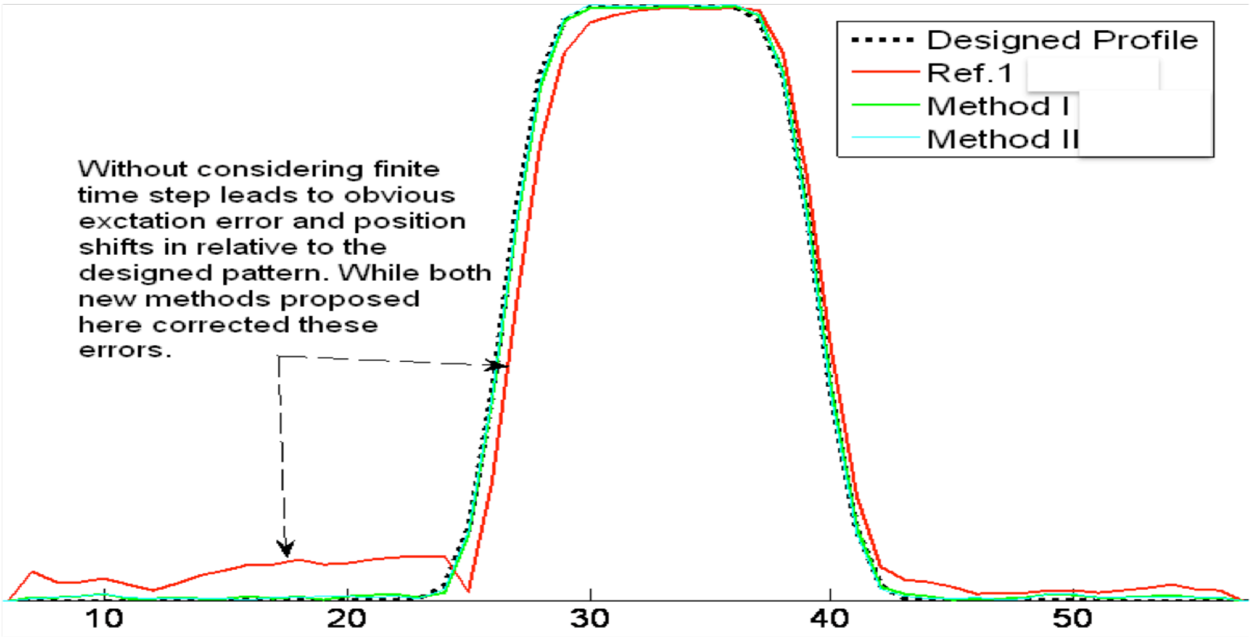

Figure 6.6 Excitation profiles taken along the red dotted line in Figure 6.5 for different RF pulse design methods.

6.3.4 Conclusion and Future work

We have proposed two novel methods to compensate the excitation artifacts due to finite gradient raster time that was widely neglected. Significant improvement can be obtained with the proposed method via compensation of discrete sampling. However, other factors, such as eddy currents, distorted gradient trajectory are also potential issues for excitation errors and should be carefully compensated during the parallel transmission experiments. Thus, future work will focus on combining the proposed methods with the eddy current compensation method in Chapter 4 to reduce the overall artifacts.

7.0 CONCLUSIONS AND FUTURE WORK

Ultra high field MRI provides the great potential for improvement in image SNR, resolution and contrast. However, the presence of dramatic spatial variation in B_1^+ field of RF coil leads to very unfavorable spatial nonuniformity in the excitation region, and largely limits the practical applications of parallel transmission technology. The central goal of this dissertation is motivated by pressing need to solve the aforementioned issue, and then bring ultra high field to clinic use.

Parallel transmission has been emerging as an active research for almost eight years since it is firstly introduced by Katscher and Zhu. However, the technique is still on the stage of academic research and by far from the clinic use. There are many reasons to hamper the forward of parallel transmission. We summarized them as two parts: hardware and software. For hardware, it is rather demanding to implement parallel transmission at ultra high field. Not only does the ultra high magnetic field scanner have to equip with the capability of multiple-channel excitation driven with independent RF pulses and power amplifiers, but it also needs high quality multiple-channel RF coil especially built for parallel transmission. As for software, an effective and robust large-tip-angle RF pulse design for parallel transmission must be proposed and implemented on ultra high field scanner. Further, hardware imperfection such as eddy current must be overcome during the experiments. Last but now least, a rapid and accurate algorithm for measuring B_1^+ transmit sensitivity maps are very important for the implement of parallel transmission.

7.1 CONTRIBUTIONS

This aims of this dissertation is to solve the aforementioned issues. And the main contributions of the work are summarized below:

- The invention, implementation, and validation of Perturbation Analysis (PTA) Method for designing large-tip-angle parallel transmission RF pulses at ultra high magnetic field (i.e., 7T); resulting in significant improvement in excitation accuracy and reduction in RF power deposition compared to other existing methods (i.e., Additive Angle Method).
- Implementation of novel model-based eddy current characterization technique to compensate the eddy current field induced on RF shield for parallel transmission at ultra high field; leading to substantial improvements in excitation patterns and improved time efficiency than any existing method (i.e., trajectory measurement method).
- It is the first time to present that, PTX 3DTRF, the 3DTRF method in conjunction with parallel transmission technique can be effective to recover the signal loss in T_2*-weighted fMRI at ultra high field (i.e., 7T). This is also the first time to prove the through-plane phase precompensation method to restore the lost signal over the whole brain and increase the BOLD contrast to brain activation at ultra high field. Robustness and reproducibility are proved by scanning multiple subjects (N=5) and multiple times on one subject (two of the five subjects were scanned twice, respectively).
- Implementation and demonstration of *in vivo* 8-channel parallel transmission at 7T for spatially localized high resolution excitation and B_1^+ inhomogeneity mitigation.

- Development of a rapid quantitative B_1 mapping technique that is especially appropriate for the implementation of parallel transmission at ultra high field.
- Development of two methods for the practical consideration of parallel transmission to compensate the excitation artifacts caused by direct discrete sampling. Significant improvement can be observed with the proposed methods.

These contributions presented here will be of importance to bring parallel transmission to clinical applications in future ultra high field MRI.

7.2 FUTURE WORK

In the final section, several interesting ideas of the extensions to the work in this dissertation are listed as below,

- Investigation of large-tip-angle pulse design with SAR reduction algorithm in parallel transmission. The variable rate selective excitation (VERSE) (72) algorithm can be used to control excitation RF power, but at the expense of increased pulse duration. So future work should include proposing effective algorithms to reduce SAR without sacrificing excitation accuracy.
- With the use of VERSE algorithm, the parallel transmission RF pulse duration will be inevitably increased. Thus future work can be focused on combining the VERSEd RF pulse design method with eddy current characterization method in Chapter 4 to mitigate the enhanced effects of eddy current and off-resonance.
- Development of a SAR monitor including simulation for *in vivo* parallel RF transmission, which is essential for parallel transmission to clinical applications.

- Applications of some conventional imaging relied on the homogeneous excitation that has been hampered by B_1^+ field inhomogeneity at 7T. With the use of parallel transmission, some potential applications such as Turbo Spin Echo (TSE) or Diffusion Tensor Imaging (DTI) can be fully realized to gain the benefits of ultra high field system.
- Implementation of parallel transmission RF pulse design in routine scanner. This involves automatically acquiring B_1^+ transmit sensitivity maps and field maps, and computing RF pulses for different slices. It is not a trivial task.

APPENDIX

DERIVATION OF LARGE-TIP-ANGLE RF PULSE DESIGN IN PARALLEL TRANSMISSION

For the sake of simplicity, we first derive the single-channel case and then extend to the multiple-channel equation. We first rewrite Eq. (3.6) and Eq. (3.7) into the single-channel form,

$$M_{xy}^{D}(\mathbf{r},T) = i\gamma\int_{0}^{T} M_{z}^{D}(\mathbf{r},t)B_{1}(t)e^{i2\pi\mathbf{k}(t)\cdot\mathbf{r}}dt \tag{3.11}$$

$$M_{xy}^{p}(\mathbf{r},T) = i\gamma\int_{0}^{T} M_{z}^{p}(\mathbf{r},t)B_{1}^{p}(t)e^{i2\pi\mathbf{k}(t)\cdot\mathbf{r}}dt \tag{3.12}$$

Then by subtracting Eq. (3.12) from Eq. (3.11), we have the following equation (for simplicity, we hide the parameters specifying the position and time dependence of the functions),

$$\begin{aligned}\Delta M_{xy}(\mathbf{r},T) = M_{xy}^{D} - M_{xy}^{p} &= i\gamma\int_{0}^{T}(M_{z}^{D}B_{1} - M_{z}^{p}B_{1}^{p})e^{i2\pi\mathbf{k}(t)\cdot\mathbf{r}}dt \\ &= i\gamma\int_{0}^{T}[(M_{z}^{p}+\Delta M_{z})(B_{1}^{p}+\Delta B_{1}) - M_{z}^{p}B_{1}^{p}]e^{i2\pi\mathbf{k}(t)\cdot\mathbf{r}}dt \\ &= i\gamma\int_{0}^{T}(M_{z}^{p}\Delta B_{1} + \Delta M_{z}B_{1}^{p} + \Delta M_{z}\Delta B_{1})e^{i2\pi\mathbf{k}(t)\cdot\mathbf{r}}dt\end{aligned} \tag{3.13}$$

Then we assume $\Delta M_{z} = M_{z}^{D} - M_{z}^{p,j} \approx M_{z}^{p,j+1} - M_{z}^{p,j}$ (j denotes the number of iteration), which is the difference between the longitudinal magnetization created by $B_{1}^{p}\{b_{1}^{p},...,b_{N}^{p}\}$ + $\Delta B_{1}\{\Delta b_{1},...,\Delta b_{N}\}$ and by $B_{1}^{p}\{b_{1}^{p},...,b_{N}^{p}\}$, respectively, and is known from the numerical solution of the Bloch equation. Finally, Eq. (3.8) can be obtained by incorporating the spatially weighted transmit sensitivity map $S(\mathbf{r})$ into Eq. (3.13).

.

BIBLIOGRAPHY

1. Hoult D, Richards R. The signal to noise ratio of the nuclear magnetic resonance experiment. J Magn Reson 1976;24:71-85.

2. Bottomley P, Andrews E. RF magnetic penetration, phase shift and power dissipation in biological tissue: implication for NMRI imaging. Phys Med Biol 1978;23:630-643.

3. Van de Moortele P-F, Arkgun C, Adriany G, Moeller S, Ritter J, Collins CM, Smith MB, Vaughan JT, Ugurbil K. B1 destructive interference and spatial phase patterns at 7T with a head transceiver array coil. Magn Reson Med 2005;54;1503-1518.

4. Vaughan JT, Garwood M, Collins CM, Liu W, DelaBarre, L, Adriany G, Andersen P, Merkle H, Goebel R, Smith MB, Ugurbil K. 7T vs. 4T: RF power, homogeneity, and signal-to-noise comparison in head images. Magn Reson Med 2001;46:24-30.

5. Collins CM, Wanzhan L, Schreiber W, Yang QX, Smith MB. Central brightening due to constructive interference with, without, and despite dielectric resonance. J Magn Reson Imaging 2005;21:192-196

6. Stenger VA, Saekho S, Zhang Z, Yu S, Boada FE. B_1 inhomogeneity reduction with transmit SENSE. In: Proceedings of the 2nd International Workshop on Parallel MRI, Zurich, Switzerland, 2004, p94

7. Saekho S, Boda FE, Noll DC, Stenger VA. Small tip angle three-dimensional tailored radiofrequency slab-select pulse for reduce B_1 inhomogeneity at 3T. Magn Reson Med 2005;53:479-484.

8. Saekho, S, Yip CY, Noll DC, Booda FE, Stenger VA. Fask-kz three dimensional tailored radiofrequency pulse for reduced B_1 inhomogeneity. Magn Reson Med 2006;55:719-724.

9. Ibrahim TS, Lee R, Baertlein BA, Abdulijalil AM, Zhu H, Robitaille PM. Effect of RF coil excitation on field inhomogeneity at ultra high fields: a field optimized TEM resonator. Magn Reson Imaging 2001;19:1339-1347.

10. Adriany G, Van de Moortele PF, Wiesinger F, Moeller S, Strupp JP, Andersen P, Snyder C, Zhang X, Chen W, Pruessmann KP, Boesiger P, Vaughan T, Ugurbil K. Trnasmit and receive transmission line arrays for 7 Tesla parallel imaging. Magn Reson Med 2005;53:434-445

11. Mao W, Smith MB, Collins CM. Exploring the limits of RF shimming for high-field MRI of the human head. Magn Reson Med 2006;56:918-922

12. Silver MS, Joseph RI, Hoult DI. Highly selective 90^o and 180^o pulse generation. J Magn Reson 1984;58:347-351.

13. Garwood M, Delabarre L. The return of the frequency sweep: designing adiabatic pulses for contemporary NMR. J Magn Reson 2001;153:155-177.

14. Katscher U, Bornert P, Leussler C, van den Brink JS. Transmit SENSE. Magn Reson Med 2003;49:144-150.

15. Zhu Y. Parallel excitation with array of transmit coils. Magn Reson Med 2004;51:775-784.

16. Grissom W, Yip CY, Zhang Z, Stenger VA, Fessler JA, Noll DC. Spatial domain method for the design of RF pulses in multicoil parallel excitation. Magn Reson Med 2006;56:620-629.

17. Belliveau JW, Kennedy DN, McKinstry RC, Buchbinder BR, Weisskoff RM, Cohen MS, Vevea JM, Brady TJ, Rosen BR. Functional mapping of the human visual cortex by magnetic resonance imaging. Science 1991;254:716-719.

18. Kwong KK, Belliveau JW, Chesler DA, Goldber IE, Weisskoff RM, Poncelet BP, Kennedy DN, Hoppel BE, Cohen MS, Turner R, Cheng H-M, Brady TJ, Rosen BR. Dynamic magnetic resonance imaging of human brain activity during primary sensory stimulation. Proc Natl Acad Sci USA 1992;89:5675-5679.

19. Ogawa S, Tank DW, Menon R, Ellerman JM, Kim SG, Merkle H, Ugurbil K. Intrinsic signal changes accompanying sensory stimulation: functional brain mapping with magnetic resonance imaging. Proc Natl Acad Sci USA 1992;89:5951-5955.

20. Ogawa S, Menon RS, Tank DW, Kim SG, Merkle H, Ellerman JM, Ugurbil K. Functional brain mapping by blood oxygenation level dependent contrast magnetic resonance imaging. Biophys J 1993;64:803-812.

21. Lipschutz B, Friston KJ, Ashburner J, Turner R, Price CJ. Assessing study-specific regional variations in fMRI signal. Neuroimaging 2001;13:392-398.

22. Lai S, Glover G. Three-dimensional spiral fMRI technique: A comparison with 2D spiral acquisition. Magn Reson Med 1998;39:68-78.

23. Yang QX, William GD, Demeure RJ, Mosher TJ, Smith MB. Removal of local field gradient artifacts in T_2^*-weighted images at high fields by gradient echo slice excitation profile imaging. Magn Reson Med 1998;39:402-409.

24. Constable R, Spencer D. Composite image formation in z shimmed functional MR imaging. Magn Reson Med 1999;42:110-117.

25. Stenger VA, Boada FE, Noll DC. Three-dimensional tailored RF pulses for the reduction of susceptibility artifacts in T_2^* weighted functional MRI. Magn Reson Med 2000;44:525-531.

26. Yip CY, Fessler JA, Noll DC. Advanced three-dimensional tailored RF pulses for signal recovery in T_2* weighted functional magnetic resonance imaging. Magn Reson Med 2006;56:1050-1059.

27. Collins CM, Li S, Smith MB. SAR and B_1 distribution in a heterogeneous human head model within a birdcage coil. Magn Reson Med 1998;40:874-856.

28. Jin J, Chen J. On the SAR and field inhomogeneity of birdcage coils loaded with the human head. Magn Reson Med 1997;21:192-196.

29. Pauly J, Nishimura D, Macovski A. A k-space analysis of small tip angle excitation. J Magn Reson 1989;81:43-56.

30. Setsompop, K, Wald, LL, Alagappan V, Gagoski, B, Hebrank F, Fontius, U, Schmitt F, Adalsteinsson E. Parallel RF transmission with eight channels at 3 Tesla. Magn Reson Med 2006;56:1163-1171.

31. Katscher U, Bornert P, van den Brink JS. Theoretical and numerical aspects of transimt SENSE. IEEE Trans Med Imaging 2004;23:520-525.

32. Ullmann P, Junge S, Wick M, Ruhm W, Hennig J. Experimental analysis of parallel excitation using dedicated coil setups and simultaneous RF transmission on multiple channels. Magn Reson Med 2005;54:994-1001.

33. Katscher U, Bornert P. Parallel RF transmission in MRI. NMR Biomed 2006;19:393-400.

34. Xu D, King KF, Zhu Y, MacKinnon GC, Linag ZP. A noniterative method to design large tip angle multidimensional spatially selective radio frequency pulses for parallel transmission Magn Reson Med 2007;58:326-334.

35. Pauly J, Nishimura D, Macovski A. A linear class of large tip angle selective excitation pulses. J Magn Reson 1989;82:647-654.

36. Hoult DI. The solution of the Bloch equations in the presence of a varying B_1 field---an approach to selective pulse analysis. J Magn Reson 1979;35:69-86.

37. Xu D, King KF, Zhu, Y, McKinnon GC, Liang ZP. Designing multichannel, multidimensional, arbitrary flip angle RF pulses using an optimal control approach. Magn Reson Med 2008;59:547-560.

38. Grissom W, Yip CY, Wright SM, Fessler JA, Noll DC. Additive angle method for fast large tip angle RF pulse design in parallel excitation. Magn Reson Med 2008;59:779-787.

39. Zheng H, Zhao T, Ibrahim TS, Boada FE. Eddy current compensated RF pulse design for parallel excitation. In Proceedings 18th Ann. Meet. Intl. Soc. Mag. Reson. Med., Stockholm, Sweden, 2010 p4923.

40. Wu X, Vaughan T, Ugurbil K, Van de Moortele PF. Parallel excitation in the human brain at 9.4 T counteracting k-space errors with RF pulse design. Magn Reson Med 2010;63:524-529.

41. Chapman B, Mansfield P. Double active magnetic screening of coils in NMR. J Phys E19:L129, 1986.

42. Wysong RE, Madio DP, Lowe IJ. A novel eddy current compensation scheme for pulsed gradient systems. Magnetic Reson Med 1994;31:572-575.

43. Takahashi, A, Peters T. Compensation of multi-dimensional selective excitation pulses using measured k-space trajectories. Magn Reson Med 1995;34:446-456.

44. Xue R, van Zijl PC, Crain BJ, Solaiyappan M, Mori S. In vivo three dimensional reconstruction of rat brain axonal projections by diffusion tensor imaging. Magn Reson Med. 1999;42:1123-1127.

45. Wedeen VJ, Reese TG, Napadow VJ, Gibert RJ. Demonstration of primary and secondary muscle fiber architecture of the bovine tongue by diffusion tensor magnetic resonance imaging. Biophys. J. 2001;80:1024-1028.

46. Yip CY. RF pulse designs for signal recovery in T_2^* weighted functional magnetic resonance imaging. 2007. University of Michigan.

47. Detre JA, Wang J. Technical aspects and utility of fMRI using BOLD and ASL. Clin Neurophysiol. 2002;113(5):621-634.

48. Chen NK, Dickey CC, Yoo SS, Guttmann CR, and Panych LP. Selection of voxel size and slice orientation for fMRI in the presence of susceptibility field gradients: application to imaging of the amygdala. Neuroimage 2003;19(3):817-825.

49. Haacke EM, Tkach JA, and Parrish TB. Reduction of T_2^* dephasing in gradient field-echo imaging. Radiology 1989:170(2):457-462.

50. Hsu JJ and Glover GH. Mitigation of susceptibility-induced signal loss in neuroimaging using localized shim coils. Magn Reson Med 2005;53:243-248.

51. Wong EC and Mazaheri Y. Shimming of the inferior frontal cortex using an external local shim coil. In Proceedings 12th Ann. Meet. Intl. Soc. Mag. Reson. Med., Kyoto, Japan, 2004, p520.

52. Glover GH. 3D z-shim method for reduction of susceptibility effects in BOLD fMRI. Magn Reson Med 1999;42:290-299.

53. Constable R. Functional MR imaging using gradient-echo echo-planar imaging large static field inhomogeneities. J Magn Reson Imag 1995;5(6):746-752.

54. Song AW. Single-shot EPI with signal recovery from the susceptibility-induced losses. Magn Reson Med 2001;46:407-411.

55. Heberlein KA and Hu X. Simultaneous acquisition of gradient-echo and asymmetric spin-echo for single-shot z-shim: Z-SAGA. Magn Reson Med 2004;51(1):212-216.

56. Griswold MA, Kannengiesser S, Muller M, and Jakob PM. Autocalibrated accelerated parallel excitation (Transmit-GRAPPA). In Proceedings 18th Ann. Meet. Intl. Soc. Mag. Reson. Med., Miami Beach, 2005, p2435.

57. Griswold MA, Jakob PM, Heidemann RM, Nittka M, Jellus V, Wang J, Kiefer B, and Haase A. Generalized autocalibrating partially parallel acquisitions (GRAPPA). Magn Reson Med 2002;47(6):1202-1210.

58. Hardy CJ, Cline HE. Spatial localization in two dimensions using NMR designer pulses. J Magn Reson 1989;82:647-654;

59. Bottomley PA, Hardy CJ. Two-dimensional spatially selective spin inversion and spin-echo refocusing with a single nuclear magnetic resonance pulse. J Appl Phys 1987;62:4284-4290.

60. Hardy CJ, Cline HE. Broadband nuclear magnetic resonance pulses with two-dimensional spatial selectivity. J Appl Phys 1989;66:1513-1516.

61. Setsompop K, Wald L.L, Alagappan V, Gagoski B. A., Adalsteinsson E. Magnitude least squares optimization for parallel radio frequency excitation design demonstrated at 7 tesla with eight channels. Magn Reson Med 2008;59:908-915.

62. Zheng H, Zhao TJ, Ibrahim T, Boada FE. Fast and Accurate Large-Tip-Angle RF Pulse Design for Parallel Excitation Using a Perturbation Analysis of the Bloch Equation. In Proceedings 18th Ann. Meet. Intl. Soc. Mag. Reson. Med., Stockholm, Sweden, 2010, p100.

63. Lin F, Kwong KK, Belliveau JW, Wald LL. Parallel imaging reconstruction using automatic regularization. Magn Reson Med 2004;51:559-567

64. Setsompop K, Alagappan V, Gagoski B, Witzel T, Polimeni J, Potthast A, Hebrank F, Fontius U, Schmitt F, Wald L.L, Adalsteinsson E. Slice-selective RF pulses for in vivo B_1^+ inhomogeneity mitigation at 7 Tesla using parallel RF excitation with 16-element coil. Magn Reson Med 2008;60:1422-1432.

65. Setsompop K Zelinski AC, Alagappan V, Nistler J, Hebrank F, Fontius U, Schmitt F, Wald LL, Adalsteinsson E. In vivo parallel RF excitation with B_0 correction. In Proceedings 15th Ann. Meet. Intl. Soc. Mag. Reson. Med., Berlin, Germany, 2007, p671.

66. Kim DH, Adalsteinsson E, Spielman DM. Simple analytic variable density spiral design. Magn Reson Med 2003;50:214-219.

67. Pauly JM, Spielman D, Macovski A. Echo-planar spin-echo and inversion pulses. Magn Reson Med 1993;29:776-782.

68. Conolly S, Nishimura D, Macovski A. Optimal control solution to the magnetic resonance selective excitation problem. IEEE Trans Med Imaging 1986;5:106-115.

69. Grissom W, Xu D, Kerr A.B, Fessler JA. Noll DC. Fast large-tip-angle multidimensional and parallel RF pulse design in MRI. IEEE Trans Med Imag 2009;28: 1548-1559.

70. Lee SK, Xu D, Lechner S.M, Vogel M.W. Bloch Simulation Acceleration for Fast Pulse Design in Parallel Transmit. In Proceedings 18th Ann. Meet. Intl. Soc. Mag. Reson. Med., Stockholm, Sweden, 2010, p4927.

71. Lee D. Lustig M, Grissom W, Pauly JM. Time-optimal design for multidimensional and parallel transmit variable-rate selective excitation. Magn Reson Med 2009;61:1471-1479.

72. Conolly S, Nishimura DG, Macovski A. Glover G. Variable-rate selective excitation. J Magn Reson 1988;78:440-458.

73. Pauly J, Hu B, Wang S, Nishimura D, Macovski A. A three-dimensional spin-echo or inversion pulse, Magn. Reson. Med. 1993;29:2-6.

74. Zheng H, Zhao T, Qian Y, Ibrahim TS, Boada FE. Improved large tip angle parallel transmission pulse design through a perturbation analysis of the Bloch Equation, Magn. Reson. Med. 2011;66:687-696.

75. Snyder C, DelaBarre L, Van de Moortele P, Snyder A, Akgun C, Tian J, Metzger G, Ugurbil K, Vaughan J. Stripline/TEM Transceiver Array for 7T Body Imaging, In Proceedings 15th Ann. Meet. Intl. Soc. Mag. Reson. Med., Berlin, Germany, 2007, p164.

76. Alecci M, Jezzard P, Characterization and reduction of gradient-induced eddy current in the RF shield of a TEM resonator, Magn. Reson. Med. 2002;48:404-407.

77. Jehenson P, Westphal M, Schuff N. Analytical method for the compensation of eddy current effects induced by pulses magnetic field gradients in NMR system, J. Magn. Reson. 1990;90:264-278.

78. Vanvaals JJ, Bergman AH. Optimization of eddy current compensation, J. Magn. Reson. 1990;90:52-70.

79. Atkinson IC, Lu A, Thulborn KR. Characterization and correction of system delays and eddy currents for MR imaging with ultrashort echo-time and time-varying gradients, Magn. Reson. Med. 2009;62:532-537.

80. Bernstein MA, King KF, Zhou XJ. Handbook of MRI pulse sequences, Academic Press, Boston, 2004.

81. Duyn JH, Yang Y, Frank JA, van der Veen JW. Simple correction method for k-space trajectory deviations in MRI. J Magn Reson 1998;132:150-153

82. Zhao T, Zheng H, Hue YK, Ibrahim TS, Qian Y, Boada FE. Practical consideration for the design of parallel transmission pulses at ultra high field. In Proceedings 19th Ann. Meet. Intl. Soc. Mag. Reson. Med., Montreal, Canada, 2011, p4439.

83. Zhao T, Zheng H, DeFranco A, Ibrahim TS, Qian Y, Boada FE. A fast B_1^+ mapping method for transmit/receive coils for parallel transmit (PTX) applications. In Proceedings 19th Ann. Meet. Intl. Soc. Mag. Reson. Med., Montreal, Canada, 2011, p2925.

84. Schneider J, Hass M, Hennig J, Junge S, Ruhm W, Ullmann P. Coping with off-resonance effects and gradient imperfections in parallel transmission experiments. In Proceedings 17th Ann. Meet. Intl. Soc. Mag. Reson. Med., Honolulu, USA, 2009, p172.

85. Yip CY, Yoon D, Olafsson V, Lee S, Grissom WA, Fessler, Noll DC. Spectral-spatial pulse design for through-plane phase precompensatory slice selection in T_2^* weighted functional MRI. Magn Reson Med 2009;61:1137-1147.

86. Yang C, Deng W, Alagappan V, Wald LL, Stenger VA. Four-dimensional spectral-spatial RF pulses for simultaneous correction of B_1^+ inhomogeneity and susceptibility artifacts in T_2* weighted MRI. Magn Reson Med 2010;64:1-8.

87. Deng W, Yang C, Stenger VA. Accelerated multidimensional radiofrequency pulse design for parallel transmission using concurrent computation on multiple graphics processing units. Magn Reson Med 2011;65:363-369.

88. Sacolick LI, Wiesinger F, Hancu I, Vogel MW. B1 mapping by Bloch-Siegert shift. Magn Reson Med 2010;63:1315-1322.

89. Cunningham CH, Pauly JM, Nayak KS. Saturated double-angle method for rapid B_1^+ mapping. Magn Reson Med 2006;55:1326-1333.

90. Yarnykh V. Actual flip-angle imaging in the pulsed steady state: A method for rapid three-dimensional mapping of the transmitted radiofrequency field. Magn Reson Med 2007;57:192-200.